

AD-A105 758

NAVAL POSTGRADUATE SCHOOL MONTEREY CA

F/G 20/1

THE EFFECT OF SCATTERING AND ABSORPTION ON NOISE FROM A CAVITAT--ETC(U)

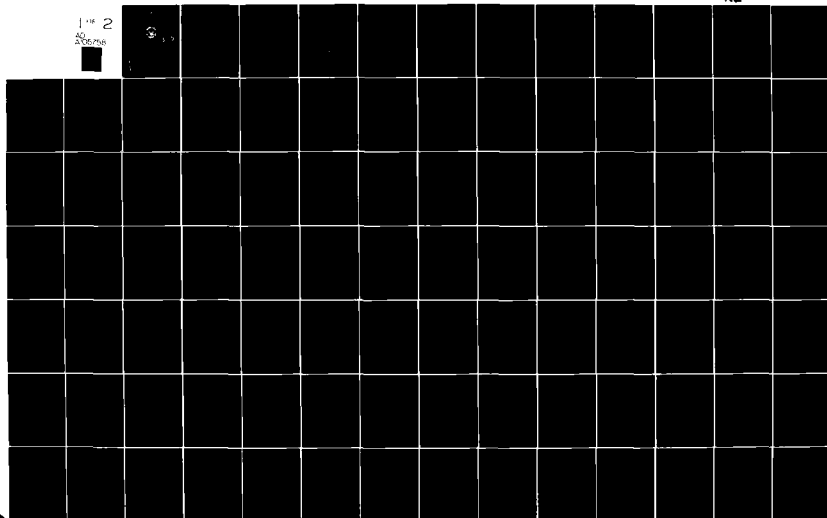
JUN 81 Y D TRONSTAD

UNCLASSIFIED

NL

1-18 2

AD-A105 758



AD A105758

LEVEL

NAVAL POSTGRADUATE SCHOOL
Monterey, California



DTIC
ELECTE
OCT 20 1981
S A D

THESIS

THE EFFECT OF SCATTERING AND ABSORPTION
ON NOISE FROM A CAVITATING NOISE SOURCE
IN THE SUBSURFACE OCEAN LAYER

by

Yngvar Dag Tronstad

June 1981

Thesis Advisor:

K. E. Woehler

Approved for public release; distribution unlimited

FILE COPY

10 31

UNCLASSIFIED

SECURITY CLASSIFICATION OF THIS PAGE (When Data Entered)

| REPORT DOCUMENTATION PAGE | | READ INSTRUCTIONS BEFORE COMPLETING FORM |
|--|-----------------------|---|
| 1. REPORT NUMBER | 2. GOVT ACCESSION NO. | 3. RECIPIENT'S CATALOG NUMBER |
| | AD-A105 758 | |
| 4. TITLE (and Subtitle) | | 5. TYPE OF REPORT & PERIOD COVERED |
| The Effect of Scattering and Absorption on Noise from a Cavitating Noise Source in the Subsurface Ocean Layer. | | Master's thesis, June 1981 |
| 6. PERFORMING ORG. REPORT NUMBER | | |
| 7. AUTHOR(s) | | 8. CONTRACT OR GRANT NUMBER(s) |
| Yngvar Dag/Tronstad | | |
| 9. PERFORMING ORGANIZATION NAME AND ADDRESS | | 10. PROGRAM ELEMENT, PROJECT, TASK AREA & WORK UNIT NUMBERS |
| Naval Postgraduate School Monterey, California 93940 | | |
| 11. CONTROLLING OFFICE NAME AND ADDRESS | | 12. REPORT DATE |
| Naval Postgraduate School Monterey, California 93940 | | June 1981 |
| 13. MONITORING AGENCY NAME & ADDRESS (if different from Controlling Office) | | 13. NUMBER OF PAGES |
| | | 176 pages |
| | | 14. SECURITY CLASS. (of this report) |
| | | Unclassified |
| | | 15. DECLASSIFICATION/DOWNGRADING SCHEDULE |
| 16. DISTRIBUTION STATEMENT (of this Report) | | |
| Approved for public release; distribution unlimited | | |
| 17. DISTRIBUTION STATEMENT (of the abstract entered in Block 20, if different from Report) | | |
| Approved | | |
| 18. SUPPLEMENTARY NOTES | | |
| 19. KEY WORDS (Continue on reverse side if necessary and identify by block number) | | |
| Scattering, absorption, rough sea surface, inhomogeneous bubble-dominated subsurface layer, torpedo, turn rate limitation, cavitating propeller, square law detector. | | |
| 20. ABSTRACT (Continue on reverse side if necessary and identify by block number) | | |
| <p>When investigating the detection performance of a passive homing torpedo used against shallow draft surface ships, certain environmental factors such as the rough sea surface and the bubble dominated inhomogeneous layer near the sea surface have to be considered. This thesis attempts to gain some insight into the behavior of a homing torpedo system during its critical attack phase, as well as getting some indications of the relative importance of the scattering mechanisms and the induced tactical</p> | | |

DD FORM 1 JAN 73 1473

EDITION OF 1 NOV 68 IS OBSOLETE
S/N 0102-014-6601

UNCLASSIFIED

SECURITY CLASSIFICATION OF THIS PAGE (When Data Entered)

UNCLASSIFIED

SECURITY CLASSIFICATION OF THIS PAGE/When Data Entered

limitations. An idealized propagation model was used as reference of comparison. For a given sea state and target speed, the results stress the importance of low operating frequency as well as a high maximum turn rate. They also point to the importance of having a search depth below the bubble-dominated subsurface layer, and a variable speed capability during the torpedo's attack phase.

| | | |
|--------------------|--------------|---------|
| Availability Codes | | |
| Dist | Avail and/or | Special |
| A | | |

Approved for public release; distribution unlimited

The Effect of Scattering and Absorption
on Noise from a Cavitating Noise Source
in the Subsurface Ocean Layer

by

Yngvar Dag Tronstad
Commander, Norwegian Navy
Marine Engineer, Norwegian Naval Academy, 1969

Submitted in partial fulfillment of the
requirements for the degree of

MASTER OF SCIENCE IN ENGINEERING ACOUSTICS

from the

NAVAL POSTGRADUATE SCHOOL
June 1981

Author

Yngvar D. Tronstad.

Approved by:

H. W. W. W.

Thesis Advisor

James V. Sanders

Second Reader

J. D. D.
Chairman, Department of Physics and Chemistry

William M. Loller
Dean of Science and Engineering

ABSTRACT

When investigating the detection performance of a passive homing torpedo used against shallow draft surface ships, certain environmental factors such as the rough sea surface and the bubble-dominated inhomogeneous layer near the sea surface have to be considered. This thesis attempts to gain some insight into the behavior of a homing torpedo system during its critical attack phase, as well as getting some indications of the relative importance of the scattering mechanisms and the induced tactical limitations. An idealized propagation model was used as reference of comparison. For a given sea state and target speed the results stress the importance of low operating frequency as well as a high maximum turn rate. They also point to the importance of having a search depth below the bubble-dominated subsurface layer, and a variable speed capability during the torpedo's attack phase.

TABLE OF CONTENTS

| | | |
|------|---|----|
| I. | INTRODUCTION----- | 12 |
| II. | SCENARIO AND TORPEDO RUN GEOMETRY----- | 15 |
| III. | OCEANOGRAPHIC BACKGROUND MATERIAL----- | 17 |
| IV. | THE PASSIVE SONAR EQUATION----- | 21 |
| V. | REFERENCE MODEL----- | 22 |
| | A. INTRODUCTION----- | 22 |
| | B. IDEALIZED TRANSMISSION LOSS MODEL----- | 22 |
| | C. NOISE SOURCE MODEL----- | 23 |
| | 1. General Characteristics of Noise Sources-- | 23 |
| | 2. The Noise Source Model----- | 26 |
| | D. PASSIVE MODE RECEIVER CHARACTERISTICS----- | 31 |
| | 1. Assumptions----- | 31 |
| | 2. Derivations----- | 32 |
| | E. REFERENCE DETECTION PERFORMANCE----- | 38 |
| | 1. Introduction----- | 38 |
| | 2. 60 kHz Case----- | 38 |
| | 3. 30 kHz Case----- | 40 |
| VI. | THE EFFECT OF SURFACE SCATTERING----- | 42 |
| | A. OCEANOGRAPHIC DESCRIPTION OF THE SEA SURFACE-- | 42 |
| | B. SCATTERING THEORY----- | 45 |
| | C. GEOMETRICAL SHADOWING----- | 57 |
| | D. ESTIMATING THE SURFACE SCATTERING EFFECT----- | 61 |
| | E. CONCLUSION AND DISCUSSION----- | 67 |

| | |
|--|-----|
| VII. THE EFFECT OF SCATTERING AND ABSORPTION FROM THE SUBSURFACE OCEAN LAYER----- | 69 |
| A. GENERAL SCATTERING THEORY----- | 69 |
| B. ABSORPTION MODEL----- | 70 |
| C. THE COHERENT INTENSITY CASE----- | 75 |
| D. THE INCOHERENT INTENSITY CASE----- | 82 |
| E. SUMMARY AND DISCUSSION OF THE BUBBLE ATTENUATION----- | 83 |
| F. THE REFRACTION BY BUBBLES----- | 85 |
| VIII. THE TURN RATE LIMITATION----- | 89 |
| IX. CONCLUSIONS AND RECOMMENDATIONS----- | 99 |
| APPENDIX A: Detailed Oceanographic Background Material----- | 102 |
| APPENDIX B: Surface Scattering TI 59 Program----- | 110 |
| APPENDIX C: Bubble Dynamics TI 59 Program----- | 116 |
| APPENDIX D: Numerical Integration TI 59 Program----- | 121 |
| APPENDIX E: Turn Rate Limitation TI 59 Programs----- | 124 |
| APPENDIX F: Figures----- | 132 |
| LIST OF REFERENCES----- | 174 |
| INITIAL DISTRIBUTION LIST----- | 176 |

LIST OF TABLES

| | | |
|------|---|-----|
| I. | Relationship between Sea State (SS), Wind Speed, and Expected Significant Wave Heights (H_s)----- | 18 |
| II. | Source Level Data and Calculation for a Blade Surface Cavitating Propeller----- | 29 |
| III. | Detection Parameters and Ranges for $f=60$ kHz----- | 86 |
| IV. | Detection Parameters and Ranges for $f=30$ kHz----- | 87 |
| V. | Frequency Distribution of Wind Speed in Percent per Year at Weather Stations Along the Norwegian Coast --- | 104 |
| VI. | Frequency Distribution of Significant Wave Height in Percent at the Weather Station "Andenes"----- | 106 |

LIST OF FIGURES

| | |
|--|-----|
| 1. Torpedo Search and Attack Geometry----- | 132 |
| 2. Location of Weather Stations along the Norwegian Coast----- | 133 |
| 3. Average Monthly Wind Speed in Beaufort from the Weather Station "Andenes"----- | 134 |
| 4. Histogram of Significant Wave in Percent per Year from the Weather Station "Andenes"----- | 135 |
| 5. Resonant Bubble Density at 12 kHz as a Function of Depth----- | 136 |
| 6. Resonant Bubble Density at 38 kHz as a Function of Depth----- | 137 |
| 7. Resonant Bubble Density at 120 kHz as a Function of Depth----- | 138 |
| 8. Ambient Noise Level Curves----- | 139 |
| 9. Typical Sound Speed Profiles in Norwegian Coastal Waters----- | 140 |
| 10. Worst Case Ray Path During Winter----- | 141 |
| 11. Worst Case Ray Path During Summer----- | 142 |
| 12. Frequencies of Wind Directions in Percent for Stations along the Coast from "Hillesøy" to "Ona"----- | 143 |
| 13. Frequencies of Wind Directions in Percent for Stations along the Coast from "Myken" to "Furuholmen"----- | 144 |
| 14. Absorption Coefficient in dB/m as a Function of Frequency----- | 145 |
| 15. Average Radiated Spectrum Level for Surface Ship as a Function of Speed in kts----- | 146 |
| 16. General Noise Spectrum for a Cavitating Propeller----- | 147 |
| 17. Spectrum Level as a Function of Total Gas Content----- | 148 |
| 18. Measured Model and Full Scale Noise Spectra----- | 149 |

| | | |
|------|---|-----|
| 19. | Square Law Detector Scheme----- | 150 |
| 20. | Required Input S/N Ratio and BT Product for Various Operating Probabilities----- | 151 |
| 21. | Probability of Detection Versus Input S/N Ratio for Various Thresholds----- | 152 |
| 22. | $-20\log R - \alpha R$ Versus R for a Frequency of 60 kHz----- | 153 |
| 23. | $-20\log R - \alpha R$ Versus R for a Frequency of 30 kHz----- | 154 |
| 24a. | Geometry of the Sea Surface Scattering----- | 155 |
| 24b. | Specular Scattering Geometry----- | 156 |
| 25. | Rough Surface Shadowing Geometry----- | 157 |
| 26. | Calculation Scheme of the Surface Scattering Effect---- | 158 |
| 27. | ΔIL Versus R----- | 159 |
| 28. | Geometry of the Subsurface Propagation Model----- | 160 |
| 29a. | Chains of Successive Scattering----- | 161 |
| 29b. | Scattering Path Going Through the Same Scatterer More Than Once----- | 161 |
| 30. | Scattering Pattern----- | 162 |
| 31. | σ_e and σ_a for 60 kHz----- | 163 |
| 32. | σ_e and σ_a for 30 kHz----- | 164 |
| 33. | Interpolated Bubble Data----- | 165 |
| 34. | $\sigma_e(a)n(a)da$ for 60 kHz----- | 166 |
| 35. | $\sigma_e(a)n(a)da$ for 30 kHz----- | 167 |
| 36. | $\sigma_a(a)n(a)da$ for 60 kHz----- | 168 |
| 37. | $\sigma_a(a)n(a)da$ for 30 kHz----- | 169 |
| 38. | Pursuit Homing Geometry----- | 170 |
| 39. | $ \dot{\phi}K/V_s $ as a Function of ϕ with Parameter p----- | 171 |
| 40. | Hit Criterion Geometry----- | 172 |

41. AOB-Limitation Versus Ship Speed with Parameter Maximum
Turn Rate-----173

ACKNOWLEDGMENT

The author wishes to gratefully express his appreciation to his advisor, Professor Karlheinz E. Woehler, for his advice, encouragement and guidance in the preparation of this thesis.

I. INTRODUCTION

The following analysis examines several factors that limit the detection performance of a passive homing torpedo with the mission objective of countering shallow-draft targets in Norwegian coastal waters. Generally, these factors can be divided into three main groups:

- Environmental factors in the ocean
- Electrical mechanical and hydrodynamical factors in the torpedo system
- The users tactical situation

The factors that are generated in the ocean itself are the principal subject of this analysis. As our interest is confined to the layer immediately below the surface of the ocean, later called the subsurface ocean layer, the main factors affecting the sound propagation are:

- Scattering and absorption due to the bubble-dominated inhomogeneous subsurface ocean layer.
- Scattering from the rough sea surface

The concentration of air bubbles and the roughness of the sea surface are determined by the windspeed. The effectiveness of both these scattering mechanisms depends on the frequency of the incident wave and the geometry of the source and receiver. The following analysis is limited to

high frequencies in the region of 30-60 kHz which are characteristic of existing torpedo systems. At high frequency and low grazing angles for the incident and received signals, the phenomena of "shadowing" of the surface by other parts of the boundary occurs. Under these conditions, the effect from the inhomogeneous subsurface ocean layer becomes increasingly important. Obviously both the above mentioned scattering mechanisms are present simultaneously. Often these two effects cannot be resolved either theoretically or experimentally, as any signal with a finite duration will be scattered from the space near the surface simultaneously with that from the sea surface itself.

In order to adequately describe the scattering mechanisms, this analysis starts with a presentation of the oceanographic background material for:

- Typical windspeed and wave height
- Typical sound speed profiles
- Density and distribution of air bubbles in the subsurface layer
- Statistical description of the sea surface

The analysis proceeds by separately estimating the effect of:

- Scattering from a randomly rough surface
- Scattering and absorption caused by an inhomogeneous subsurface layer,

and comparing their relative importance. The method employed for these estimations is an approximation that is a combination of both ray and wave theories. Ray methods are used to follow the acoustic signal from its source to the vicinity of the scatterer. Wave theory is used to calculate the actual scattering process. Finally, ray theory is again used to follow the scattered signal to the receiver.

An idealized propagation model consisting of an isotropic stratified medium will be used as reference of comparison. This model is founded on:

- A noise source from a cavitating propeller blade.
- The operational characteristics for a square law detector (ROC-curves).
- A transmission loss model based on geometrical spreading and absorption losses in homogeneous sea water.

In this analysis, the passive sonar equation is used to predict the performance of the homing system. The detection range encountering the two scattering effects will be obtained from the sonar equation and compared to the detection range based on the reference model. Thus, the difference in ranges at which the homing device just acquires the target with and without scattering is a measure of efficiency.

II. SCENARIO AND TORPEDO RUN GEOMETRY

In the Norwegian coastal waters, the primary mission of a torpedo system is to counter an amphibious force consisting of escorts, supply ships, and shallow-draft landing crafts. Typical characteristics of these three ship types are as follows:

Supply ships:

- Displacement 5000 tons
- Length 100 m.
- Draft 6 m.
- Speed 15-20 kts.

Escort ships:

- Displacement 2000-3000 tons
- Length 85 m.
- Draft 3 m.
- Speed 35 kts.

Landing craft:

- Displacement 1000 tons
- Length 80 m.
- Draft 2 m.
- Speed 18 kts.

In order to simplify this analysis, moderate sea states (SS 3) are assumed. Since "moderate" wave heights of two meters

are appreciable when compared with the two-meters draft of the landing craft, the possibility of an acoustic torpedo impacting the target at a depth of two meters is very remote without the use of an influence exploder.

Two relevant search and attack schemes will be considered. These are illustrated in Fig. 1 together with the operation of the influence exploder. From target validation to completion of terminal attack, the torpedo continuously tracks in the azimuth plane. In Case A, ascent is inhibited after enable. For Case B, ascent is inhibited after the torpedo reaches terminal attack depth.

An assumed attack depth of six meters is consistent with the activation range of influence exploders and is deep enough to preclude wave or "free surface" induced disturbances of the torpedo. Success of the attack depends primarily on the availability of maintaining azimuth-plane steering to within a short horizontal range of the target, and the subsequent operation of the influence exploder.

Case A is of particular interest to this analysis, as both the search and attack-depth are within the subsurface layer.

III. OCEANOGRAPHIC BACKGROUND MATERIAL

The oceanographic background for predicting typical and extreme conditions of

- wind speed
- wave heights
- bubble densities and distributions
- ambient noise versus self noise
- sound speed profiles

are outlined in detail in Appendix A. Even though most data have general validity for Norwegian coastal waters, the region above 68°N are of particular interest. Thus, a typical area combining open as well as confined waters can be represented by "Andfjord" at 70°N , where the oceanographic conditions can be related to the weather station "Andenes," see Fig. 2.

Figures 3 and 4 [Ref. 1] show average windspeed and the occurrence of significant wave heights as a function of time of year at weather station "Andenes," respectively. The bulk of data is centered around a windspeed of Beaufort:4-5 (11-21 kts) and SS:3-4 (significant wave heights: 1-2 m). Table I gives the relationship between SS, windspeed and expected significant wave heights.

TABLE I
RELATIONSHIP BETWEEN SEA STATE (SS), WIND SPEED,
AND EXPECTED SIGNIFICANT WAVE HEIGHTS (H_s)

| Class Number | Significant Wave Height in m | Beaufort Scale |
|-----------------|---------------------------------|-------------------|
| SS | H_s | |
| 0 | 0 | 0 |
| 1 | 0 - 0.1 | 1 |
| 2 | 0.1 - 0.5 | 2 |
| 3 | 0.5 - 1.25 | 3-4 |
| 4 | 1.25 - 2.5 | 5 |
| 5 | 2.5 - 4.0 | 6-7 |
| 6 | 4.0 - 6.0 | 8 |
| 7 | 6.0 - 9.0 | 9-10 |
| 8 | 9.0 - 14.0 | 11 |
| 9 | >14 | 12 |

This, together with the low probability of having an amphibious operation occurring in high sea states ($SS > 5$) justifies the assumption of moderate sea state with wind-speed in the region of 12 kts and wave heights of 2 m.

The bubble data distribution taken from Ref. 2 was obtained in the area "Tromsö" - "Björnöya" during the period June-November 1978. These data correlate very well with a larger body of data obtained by H. Medwin [Ref. 3].

Figures 5, 6 and 7 [Ref. 2] show the density of resonant bubbles as a function of depth with windspeed as parameter for the 12, 38 and 120 kHz. As seen from these figures, the number of resonant bubbles are an increasing function of frequency and windspeed, and a decreasing function of depth. Below a depth of approximately 15 m, the number of bubbles is negligible for the windspeed of interest.

The effect of SS (windforce) on the ambient noise level is given in Fig. 8 [Ref. 4]. Shallow coastal Norwegian waters are typically 5-10 dB noisier than the corresponding deep water. However, great variability caused by local ship traffic, fishing fleet activity, marine life and local wind conditions makes ambient noise prediction difficult in these areas. This means that for accurate modeling, ambient noise prediction have to be done at each location as its level is both site and time dependent. However, Fig. 8 shows that for frequencies higher than 50 kHz, the

effect of windforce on the ambient noise level decreases to a lower bound determined by the thermal agitation. Based on the above discussion and experience related to noise levels for torpedo systems, the self noise will be assumed to be dominant through this analysis.

Figure 9, obtained from Ref. 5, shows that the sound speed profiles usually encountered in the area of interest results in extremely difficult sonar conditions. This is illustrated in Figs. 10 and 11, which show worst-case ray path derived from Fig. 9. In addition, the presence of bubbles in the subsurface layer causes the sound speed to be a function of frequency. The above two factors may frequently be the ones limiting the detection range of the torpedo. These effects can be minimized by selecting an appropriate search depth for a particular sound speed profile. In addition, for Case B the corresponding curved homing trajectories in the pitch plane give an error in apparent range to target. This effect will normally be taken into account by devising appropriate attack logic which is outside the scope of the present analysis.

IV. THE PASSIVE SONAR EQUATION

A measure of efficiency for a passive homing torpedo is the detection range obtained by solving the passive sonar equation for broadband noise:

$$SL + 10 \log B - TL(\text{geom}) - \alpha R + DI - NL - DT = 0 \quad (1)$$

where

SL = spectral level of the broadband noise
radiated by the target (in dB re $1 \mu\text{Pa}/\text{LHz}$ at
1m).

R = detection range (in m).

α = attenuation coefficient at the center frequency
(in dB/m).

DI = receiving sensitivity (directivity index)
(in dB re $1 \mu\text{Pa}$).

NL = noise level at the receiver in the bandwidth B
(in dB re $1 \mu\text{Pa}$).

DT = detection threshold; the signal to noise ratio
at the transducer output required for a de-
tection probability of p_D and associated false
alarm probability p_{FA} (in dB).

V. REFERENCE MODEL

A. INTRODUCTION

In order to produce the reference for the analysis the sonar equation is solved assuming ideal free-field conditions, a simple noise source model, and a generalized square-law detector.

B. IDEALIZER TRANSMISSION LOSS MODEL

Because the presence of refraction, scattering, and of ocean boundaries, free-field conditions associated with homogeneous (isovelocity) and unbounded medium seldom exist in the sea. However, as a basis for comparison, the ubiquitous spherical spreading law plus an added loss term due to "normal absorption" can be used as a reference model for measuring the effects of the previous mentioned scattering and absorption mechanisms. Thus, the reference transmission loss model can be expressed as:

$$TL=20\log R + \alpha R \quad (2)$$

where the absorption coefficient, expressed in dB/m, can be obtained from Fig. 14 taken from Ref. 8.

C. NOISE SOURCE MODEL

1. General Characteristics of Noise Sources

Sound is generated in a fluid medium by any process that causes an unsteady pressure field. Physically processes that can cause an unsteady pressure field include:

- Pulsation of a boundary surface of the medium
- The action of a nonsteady source on the fluid
- Turbulent motion in the fluid
- Oscillatory temperatures

It can be shown, e.g., Ref. 10, that each source mechanism mathematically corresponds to a dominant order of multipole. If all sources are of such a nature that their time variation can be described by a Fourier Integral, it can be shown [Ref. 10] that the Helmholtz Equation is

$$\nabla^2 p_\omega(x) + \frac{\omega^2}{C^2} p_\omega(x) = -4\pi f_\omega(x) \quad (3)$$

$$= \underbrace{\frac{\partial Q_\omega(x)}{\partial t}}_{\text{Term 1}} + \underbrace{\nabla \cdot F_\omega(x)}_{\text{Term 2}} - \underbrace{\frac{\partial^2 T_{\omega ij}}{\partial x_i \partial x_j}}_{\text{Term 3}}$$

Term 1 Term 2 Term 3

where the right hand side describes distributed source terms.

The terms on the right hand side of Eq. (3) have the following interpretations:

- Term 1: mass injection
- Term 2: external force
- Term 3: turbulent shear stress

In the long distance and long wavelength approximation, it can be shown that the mass injection term gives rise to a simple source; a zero order pole called a monopole. The monopole radiates omnidirectional with no angular dependence. At large distances the pressure field from the monopole radiation is that of a point source. Examples of this are:

- Pulsating bubbles
- Cavitation

The external force, in the long distance and long wavelength approximation, is associated with a dominant dipole which has a cosine directional pattern. Examples of this type of radiation is that caused by the vibratory motion of an un baffled rigid body.

Radiation from turbulent shear stresses is characterized by a lowest order term of quadrupole nature.

The efficiency of the source terms decreases with increasing dependence on the spatial derivatives. This can be understood when recognizing that wave functions of the general form $f(x-ct)$ have a time derivative

$$\left| \frac{\partial}{\partial t} f(x-ct) \right| = c f_t(x-ct) \quad (4)$$

which is magnitude c (sound speed) greater than the spatial derivative

$$\left| \frac{\partial}{\partial x} f(x-ct) \right| = f_x(x-ct) \quad (5)$$

Other factors being equal, the radiation from an external force is small compared to that from mass injection, and that from turbulent shear stress is the smallest; therefore, monopole radiation is the dominant term.

Propeller cavitation, when it occurs, is usually the dominant noise source for any marine vessel. Submarine and torpedoes often operate at a depth great enough to avoid cavitation. Surface ships, on the other hand, generally have well developed propeller cavitation with the result that their radiated spectrum from 5 Hz to 100 kHz is controlled by this source.

The basic phenomena of cavitation combined with propeller hydrodynamics give the fundamental characteristics of propeller cavitation noise. An excellent qualitatively discussion of this can be found in Ref. 9:Chs. 7 and 8, from which the following is extracted:

Propeller blades are rotating twisted wings that produce hydrodynamic forces. Depending on operating conditions, they experience cavitation on a number of different places. Of these there are three prominent types:

- Tip vortex cavitation
- Hub vortex cavitation
- Surface blade cavitation

In addition to the two types of vortex cavitation, there normally are two types of blade surface cavitation:

-Back: driving face

-Front: suction surface

Of all kinds of propeller cavitation, surface blade cavitation on the suction surface is normally the most noisy, while hub vortex cavitation is the least noisy.

2. The Noise Source Model

Due to lack of recorded and available noise data from the target in question, the noise source has been generalized on the basis of the following discussion and assumptions:

The noise source will be build up around a surface blade cavitating propeller operating in a good to poor wake; surface cavitation will be assumed to be dominant.

D. Ross [Ref. 9] has developed an approximate theory for cavitation noise, where dimensional analysis is combined with the basic results of cavitation theory that the acoustic pressure is proportional to the product of the collapse pressure of the cavities and the volume of cavitation produced per unit time. From this synthesis it is found that the total acoustic intensity varies as:

$$I \approx K_{ti} \frac{p_{obs} D (U_{ti})^3}{r^2} \left[\left(\frac{U_t}{U_{ti}} \right) \left(\frac{U_t}{U_{ti}} - 1 \right)^2 \right] \quad (6)$$

where

r = distance of the hydrophone from the source

K_{ti} = the cavitation inception parameter

U_t = blade tip speed

U_{ti} = blade tip speed for inception of cavitation

This expression shows that propeller cavitation noise power is proportional to the total number of blades, b , the blade chord, s , and to the propeller diameter, D , and is a function of the tip speed with the dependence on the tip speed being the strongest. The different blade surface sections where cavitation exist are uncorrelated and the radiated noise is treated as a single monopole radiation so that at a distance $r \gg a$ (where a is the characteristic dimension on the source region) the radiation is similar to that of a point source with no angular dependence.

Submarines and torpedoes with centerline propellers have a relatively symmetric inflow condition. Surface ship propellers, in contrast, operate under nonuniform inflow conditions. Circumferential wake variation causes the radiated sound to be amplitude modulated at the blade rate frequency. Furthermore, slight physical difference between the blades produces modulation at the shaft rate frequency. These amplitude variations gives a very distinct characteristic to the radiated noise that can be used for classification purposes to reduce the probability of false alarm.

The most complete source of data on surface ship radiated noise are measurements made during WWII, reported

in a compendium issued by the U.S. Office of Scientific Research and Development (OSRD) in 1945 and declassified in 1960. When these data are examined the radiated noise is found to depend on tip speed and the number of propeller blades with little dependence on the other variables. For surface ships near cruise speed, the source level for frequency over 100 Hz can be written as:

$$SL = SL' + 20 - 20 \log f; f > 100 \text{ Hz} \quad (7)$$

where

f = frequency in Hz

SL' = overall source level in dB re $1 \mu\text{Pa}$.

The overall level can be expressed as:

$$SL' = 175 + 60 \log U / 25 + 10 \log b / 4 \quad (8)$$

where

$$U = \pi n D \quad (9)$$

n = rotational speed (rpm)

D = diameter of the propeller (m).

The above expressions are used as the basis for the noise model with the following input data:

n = 300 rpm for maximum cruise speed of 15 kts.

n = 180 rpm for a cruise speed of 10 kts.

D = 2 m.

b = 5.

The resulting noise spectrum, in dB re $1 \mu\text{Pa}$ at 1 m, as a function of speed in kts. are tabulated in Table II.

TABLE II

SOURCE LEVEL DATA AND CALCULATION
FOR A BLADE SURFACE CAVITATING PROPELLER

| Rotational Frequency n rpm | Diameter of Propeller D m | Tip Speed U_t m/s | Advance Speed U m/s | Overall Level | | Average Source Level | |
|---------------------------------------|------------------------------------|------------------------------|------------------------------|------------------|------------------|-------------------------|------------------|
| | | | | SL' | dB re 1 μ Pa | SL | dB re 1 μ Pa |
| 300 | 5 | 2 | 15 | 182 | 106.0 | | |
| 180 | 3 | 2 | 10 | 168.6 | 93.0 | | |

and plotted in Fig. 15. A one sigma region (5 dB of uncertainty) is incorporated in Fig. 15.

The above noise spectrum estimation agrees very well in the high frequency limit, with more recent studies by A. Lövik [Refs. 11 and 12]. Here it is found that the cavitation spectra, both theoretically and experimentally, can be divided into four frequency regions, as illustrated in Fig. 16.

Region I is dominated by noise at the blade frequency and its harmonics. The emitted sound is caused by the volume variation of the main cavity.

Region II starts at the bubble frequency, which is the reciprocal of the lifetime of the main cavity. The mean power level is found to decrease with increasing frequency as $f^{-2.5}$.

Region III is an intermediate region.

Region IV associated with the shock waves starts at the mean collapse frequency f_c , given by the mean collapse time. The power level is found to decrease as f^{-2} , as in Eq. 5.

The number of gas bubbles in the water have a pronounced effect on the high frequency cavitation noise from the propeller. This is illustrated in Fig. 17, obtained from Ref. 12, where the power is found to decrease as much as 40 dB with increasing gas content.

Scaling laws are developed [Ref. 12] for each region based on a series of models and full scale measurements. These laws depend on the dynamic pressure induced by the propeller, the model ratio, and the gas content of the water. The full scale measurements were performed in cooperation with the Royal Norwegian Navy and the Marine Institute of Norway. The model experiments were performed in the largest cavitation tunnel at the Ship Research Institute of Norway.

In summary, the scaling of cavitation noise was demonstrated to be a useful tool in predicting a full scale cavitation noise as shown in Fig. 18 [Ref. 12] which compares measured noise spectra for the model and full scale measurements.

For the high frequency region, the source levels are of the same magnitude as predicted by the WWII empirical formula.

D. PASSIVE MODE RECEIVER CHARACTERISTICS

1. Assumptions

For receiver characteristics assume a square law detector with a center frequency $f = 60$ or 30 kHz and a bandwidth B . The detection scheme is shown in Fig. 16. The principal assumptions employed in the derivation are as follows:

- Gaussian signals in Gaussian noise
- Frequency independent signal and noise spectra

-Integration time T is sufficiently long to permit application of the central limit theorem.

2. Derivations

The detector input $r(t)$ is assumed to be a zero-mean Gaussian process composed of noise alone or signal plus noise expressed by the two well known hypotheses

$$H_0 r(t) = n(t) \quad (10)$$

$$H_1 r(t) = s(t) + n(t)$$

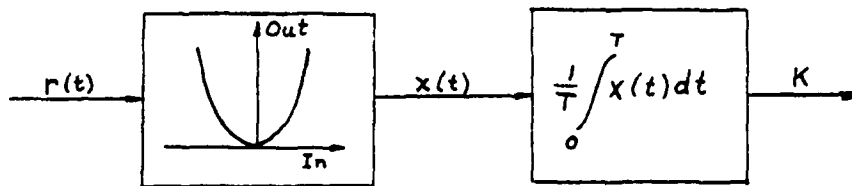
where:

$n(t)$: noise signal

$s(t)$: signal.

The two signals $s(t)$ and $n(t)$ are assumed to be independent.

Assume that the spectral shape of $s(t)$ and $n(t)$ are the same, such that H_0 and H_1 only differ in the total power level. Then the detector-smoother have the form:



Schematic of detector-smoother

and

$$x(t) = r^2(t) \quad (11)$$

Furthermore, let the noise variance be normalized to unity (for convenience) and the signal variance be denoted by σ^2

$$\text{Var}[n(t)] = 1 \quad (12)$$

$$\text{Var}[s(t)] = \sigma^2$$

Because of the assumed similarity in the spectral shapes, the autocorrelation functions are

$$R_n(\tau) = F^{-1}[N(f)] = \rho(\tau); \quad N(f) \text{ is the noise power spectral density.} \quad (13)$$

$$R_s(\tau) = \rho(\tau) \sigma^2$$

$$R_n(\tau) = H_0 \rho(\tau) + H_1 (1 + \sigma^2) \rho(\tau)$$

Furthermore, assume that the integration time T is long enough so the central limit theorem holds, implying that K also is a Gaussian random variable.

This yields that the probability density function of the output variable and hence the detection and false alarm probabilities are completely determined once the mean and the variance of K are derived.

If a process $V(t)$ is wide-sense stationary, then

$$E[V(t)] = E\left[\frac{1}{T} \int_0^T V(t) dt\right] = \frac{1}{T} \int_0^T E[V(t)] dt = v \text{ (constant)} \quad (14)$$

Thus, assuming that $r(t)$ is a wide-sense stationary process.

$$E[K] = E[x(t)] = E[r(t)] = 1 + \sigma^2 \quad (15)$$

and similarly

$$\text{Var}[V] = E[V^2] - \{E[V]\}^2 = \frac{1}{T^2} \iint_{00}^{TT} E[V(t)V(s)] dt ds - v^2 \quad (16)$$

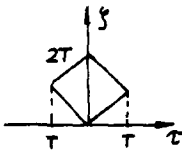
$$\text{Var}[V] = \frac{1}{T^2} \iint_{00}^{TT} [R_V(t-s) - v^2] dt ds = \frac{1}{T^2} \iint_{00}^{TT} \text{Cov}_V(t-s) dt ds$$

where $\text{Cov}_V(t-s)$ is a covariance function.

Then letting

$$\tau = t-s$$

$\zeta = t+s$, and substituting into Eq. (7) yields

$$\text{Var}[V] = \frac{1}{T^2} \iint_{\diamond} \text{Cov}_V(\tau) \frac{d\zeta d\tau}{2}$$


$$\text{Var}[V] = \frac{1}{T} \int_{-T}^T \left[1 - \frac{|\tau|}{T}\right] \text{Cov}_V(\tau) d\tau \quad (17)$$

Consequently

$$\text{Var}[K] = \frac{1}{T} \int_{-T}^T \left[1 - \frac{|\tau|}{T}\right] \text{Cov}_V(\tau) d\tau \quad (18)$$

Then, evaluating the covariance function from the autocorrelation function

$$R_X(\tau) = E[x(t)x(t-\tau)] = E[r^2(t)r^2(t-\tau)] \quad (19)$$

Since $r(t)$ is Gaussian, the above fourth moment can be expressed as product and sums of second moments:

$$\begin{aligned} R_X(\tau) &= r^2(t) \cdot r^2(t+\tau) + 2r(t)r(t-\tau) \cdot r(t)r(t-\tau) \\ &= R_r^2(0) + 2R_r^2(\tau) \\ R_X(\tau) &= (1+\sigma^2)^2 + 2(1+\sigma^2)^2 \rho^2(\tau) \end{aligned} \quad (20)$$

Thus, the covariance function is

$$\begin{aligned} \text{Cov}_X(\tau) &= R_X(\tau) - \{E[x(t)]\}^2 \\ &= (1+\sigma^2)^2 + 2(1+\sigma^2)^2 \rho^2(\tau) - (1+\sigma^2)^2 \end{aligned}$$

$$\text{Cov}_X(\tau) = 2(1+\sigma^2)^2 \rho^2(\tau) \quad (21)$$

Inserting Eq. (12) into Eq. (9) yields

$$\begin{aligned} \text{Var}[K] &= \frac{1}{T} \int_{-T}^T \left\{ \left[1 - \frac{|\tau|}{T} \right] 2(1+\sigma^2)^2 \rho^2(\tau) \right\} d\tau \\ \text{Var}[K] &= \frac{2(1+\sigma^2)^2}{T} \int_{-T}^T \left[1 - \frac{|\tau|}{T} \right] \rho^2(\tau) d\tau \end{aligned} \quad (22)$$

If T is large compared to the correlation time

$$TB \gg 1$$

then we can substitute the limit for Eq. (22) by

$$\begin{aligned} \text{Var}[K] &= \frac{2(1+\sigma^2)^2}{T} \int_{-\infty}^{\infty} \rho^2(\tau) d\tau \\ &= \frac{2(1+\sigma^2)^2}{T} \int_{-\infty}^{\infty} N^2(f) df \end{aligned} \quad (23)$$

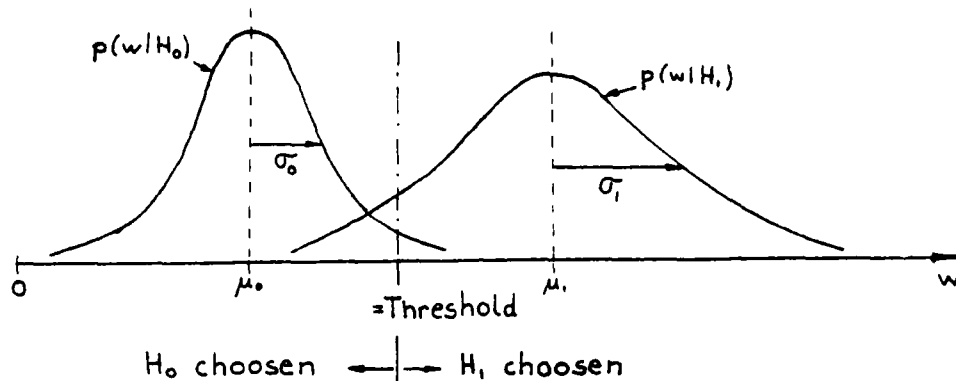
If we further make the assumption that the signal and noise have ideal flat bandpass spectra:

$$N(f) = \begin{cases} 1/2B, & f-B/2 < f < f+B/2 \\ 0, & \text{otherwise,} \end{cases} \quad (24)$$

Inserting Eq. (24) in Eq. (23) yields

$$\text{Var}[K] = \frac{(1+\sigma^2)^2}{BT} \quad (25)$$

The probability density function for the output of the detector have the following form



Here w is the outcome of all possible signals. The false alarm probability is obtained by integrating the conditional probability $p(w|H_0)$ over the outcome space for which to choose H_1 .

$$P_{FA} = \int_j^{\infty} p(w|H_0) dw = Q\left(\frac{j - \mu_0}{\sigma_0}\right) \quad (26)$$

Similarity, the miss probability = 1 - detection probability is obtained by integrating the conditional probability $p(w|H_1)$ over the outcome space for which to choose H_0 .

$$P_M = 1 - P_D = \int_{-\infty}^j p(w|H_1) dw = Q\left(\frac{\mu_1 - j}{\sigma_1}\right) \quad (27)$$

Further defining the input and output signal-to-noise ratios as

$$S/N(\text{input}) = \frac{\sigma^2}{1} = \sigma^2 \quad (28)$$

$$S/N(\text{output}) = \frac{(\mu_1 - \mu_0)^2}{\sigma_1^2} \quad (29)$$

For the square law detector where

$$\mu_0 = E[n^2(t)] = 1, \quad \mu_1 = E[r^2(t)] = E[K] = 1 + \sigma^2 \quad (30)$$

$$\begin{aligned} \sigma_0^2 = \text{Var}[n^2(t)] &= \frac{1}{BT}, \quad \sigma_1^2 = \text{Var}[r^2(t)] \\ &= \text{Var}[K] = \frac{(1 + \sigma^2)^2}{BT} \end{aligned}$$

The output signal-to-noise ratio:

$$S/N(\text{output}) = \frac{(1 + \sigma^2 - 1)^2}{\left[\frac{(1 + \sigma^2)^2}{BT} \right]} = \frac{BT \sigma^4}{(1 + \sigma^2)^2} \quad (31)$$

The input signal-to-noise ratio:

$$S/N(\text{input}) = \sigma^2 \quad (32)$$

The probability of false alarm:

$$P_{FA} = Q[\sqrt{BT}(j-1)] \quad (33)$$

The probability of detection:

$$P_D = 1 - Q\left[\sqrt{BT} \left(\frac{1 + \sigma^2 - j}{1 + \sigma^2} \right)\right] \quad (34)$$

The Equations (32), (33), and (34) are plotted for a variety of realistically encountered conditions. Figure 17 gives BT versus S/N(in) (identical to the detection threshold DT) for various combinations of p_D and p_{FA} .

Figure 18 gives p_D versus S/N(in) for various combinations of the threshold j and p_{FA} . This constitutes the ROC-curves for the generalized square law detector.

E. REFERENCE DETECTION PERFORMANCE

1. Introduction

As both the scattering and absorption are frequency dependent, it is necessary to have reference models for both 60 and 30 kHz.

2. 60 kHz Case

The range dependent portion of the sonar Equation (1):

$$-20\log r - \alpha R$$

is plotted in Fig. 19 for $\alpha=0.021$ dB/m taken from Fig. 14.

Figures 15, 17 and 19 are then used to estimate the detection range:

- (a) Select p_D , p_{FA} , B , and the integration time T .
The detection threshold $DT=S/N(\text{input})$ is then found from Fig. 17.
- (b) Select the speed of the target and find the SL from the noise source model (Fig. 15). Then, reasonable values for the receiver sensitivity DI and the self noise level NL yields the left hand side of the sonar equation (1) except for range dependent term.
- (c) Use Fig. 19 to solve the passive equation for R .

A realistic example may illustrate the above procedure.

(a) Entering Fig. 17 with

$$P_D = 0.5$$

$$P_{FA} = 10^{-6}$$

$$B = 4500 \text{ Hz}$$

$$T = 100 \text{ msec}$$

yields.

$$DT = -6.5 \text{ dB.}$$

(b) Selecting a target speed of 12 kts. gives

(from Fig. 15) $SL=100 \text{ dB}$. Selecting a

typical transducer sensitivity $DI = -180 \text{ dB}$.

Assuming the NL to be dominated by self noise
of typical value $NL=-124 \text{ dB}$. This yields

$$SL+10\log B+DI-NL-DT=87 \text{ dB.}$$

(c) Figure 19 with

$$-20\log R-0.02R=-87$$

yields

$$R=1200 \text{ m. for } a=0.02 \text{ dB/m and } f=50 \text{ kHz.}$$

The influence of different design parameters like self
noise and detection threshold on the passive detection
performance is now easily investigated by the above
procedure.

Although outside the main scope of this analysis,
the above statement can be confirmed with an example. As
seen from Fig. 18, a probability of false alarm $p_{FA} = 10^{-6}$
implies a threshold setting = 0.9 dB above the noise level.

Due to the variability of the noise level together with the practical difficulty in accurately setting the threshold, a more realistic goal for the threshold would typically be 3 dB. Going into Fig. 17 shows that the corresponding value for DT for $p_D = 0.5$ is $DT = 0$ dB, with a corresponding low value for the p_{FA} .

Letting $DT=0$ dB and keeping the previous assumed values of SL, DI, and NL yields:

$$SL+10\log B+DI-NL-DT=80.5 \text{ dB.}$$

The corresponding detection range is:

$$R = 1000 \text{ m, for } \alpha = 0.02 \text{ dB/m and } f = 60 \text{ kHz.}$$

Thus, this change in threshold setting caused a decrease in detection range from 1200 m to 1000 m in return of a significant decrease in the false alarm probability.

3. 30 kHz Case

In order to estimate the reference detection range for an operating frequency of 30 kHz, we utilize the sonar equation (1).

Assume that the receiver has the same generalized passive detector characteristics as in the 60 kHz case:

$$DI = -180 \text{ dB}$$

$$NL = -124 \text{ dB.}$$

$$DT = -6.5 \text{ dB, based on } p_D = 0.5 \text{ and } p_{FA} = 10^{-6}.$$

However, the empirical equation (7) for the source level:

$$SL=SL'+20-20\log f$$

shows that the source level falls off as f^{-2} . If the dynamical and dimensional parameters of the propeller are the same, SL will increase by +6 dB when the frequency is reduced from 60 to 30 kHz.

A source level of

$$SL=100+5=106 \text{ dB}$$

gives a range dependent solution of the sonar equation

$$-20\log R - \alpha R = -87 - 6 = -93 \text{ dB.}$$

A plot of

$$-20\log R - \alpha R$$

is given in Fig. 20 for an absorption coefficient $\alpha=0.01$ dB/m taken from Fig. 14.

Figure 20 then gives a detection range of

$$R = 2400 \text{ m.}$$

Thus, as seen from these ideal reference calculations, halving the frequency gives a higher source level and a lower absorption loss, resulting in a doubling of the detection range.

VI. THE EFFECT OF SURFACE SCATTERING

A. OCEANOGRAPHIC DESCRIPTION OF THE SEA SURFACE

The roughness of the sea surface is the essence of the scattering mechanism. Thus, to adequately describe the scattering of sound from a randomly rough sea surface, it is necessary to formulate a suitable description of the sea surface from an acoustical propagation point of view.

Generally the shape of the rough sea surface is most appropriately described in terms of time and spatial dependent random variables. However, observation of the ocean under the same environmental (meteorological) conditions indicates that the roughness is the same over large areas and for periods of at least several hours. The random processes responsible for the structure of the sea surface, therefore, can be considered stationary at least over periods of hours. With this assumption, the sea surface can be described in terms of the statistical description of the surface displacement function, and the distribution of signals reflected from the sea surface can then be related to this probability distribution function.

The most significant statistical parameters describing the scattering mechanism from the randomly rough surface are:

- the mean square slope
- the mean square surface height
- the correlation length.

Optical measurements made at sea by C. Cox and W. Munk [Ref. 13] showed that the sea surface with an arbitrary wide continuous spectrum of waves is characterized by a Gaussian distributed surface slope. The mean square slope, determined from these optical measurements is

$$\langle \zeta'^2 \rangle = \Sigma^2 = (3+5.12w) \times 10^{-3} \quad (35)$$

where

W=wind speed in m/s measured 41 ft (12.5 m) above
the sea surface.

The Gaussian distribution of surface slopes implies that the surface displacement function can be described by a Gaussian probability density function with zero mean

$$\langle \zeta \rangle = 0$$

and variance

$$\langle \zeta^2 \rangle = \sigma^2$$

and Gaussian correlation function

$$\langle \zeta(t)\zeta(t+\tau) \rangle$$

The mean square height σ^2 , is obtained by integrating the frequency spectrum of the fully developed sea. The frequency spectrum G is given by the commonly accepted semi-empirical expression of Piersom-Moskowitz [Ref. 14] as

$$G(\Omega) = \frac{\alpha g^2}{\Omega^5} \exp\left[-\beta \frac{\Omega_0}{\Omega}\right]^4 \quad (36)$$

where

Ω = frequency (in s^{-1})

$\alpha = 8.1$

$\beta = .74$

$\Omega_0 = g/W$ (in s^{-1}).

W = wind speed in m/s at 19.5m above the sea surface

g = gravitational acceleration (in m/s^2).

This gives

$$\sigma^2 = \int_0^{\infty} G(\Omega) d\Omega = \frac{\alpha W^4}{4\beta g^2} \quad (37)$$

For a Gaussian autocorrelation function expressed as

$$\psi(\tau) = \frac{1}{\sigma^2} \langle \zeta(t) \zeta(t+\tau) \rangle = e^{-\tau^2 / T^2} \quad (38)$$

where

T = correlation length.

The following relationship for the mean square height holds for sea of small roughness

$$\Sigma^2 = \frac{2\sigma^2}{T^2}, \text{ see later Eq. (60)} \quad (39)$$

and the correlation length is thus:

$$T = \sqrt{2} \frac{\sigma}{\Sigma} \quad (40)$$

B. SCATTERING THEORY

All real boundaries are rough for radiation with short enough wavelength, and the apparent roughness depends on the "viewing" conditions. The wave reflected by a plane surface has the same properties as the incident wave since the radiation is scattered coherently and there is a definite relation between the incident and scattered waves.

A randomly rough surface, however, such as the wind generated ocean surface, scatters radiation in all directions, i.e., an illuminated area is visible from any direction.

Heuristically there are two distinct approaches to this phenomena.

1. If the boundary is rough most of the radiation is scattered and there is little transmission in the specular direction. Thus, the attenuation caused by the irregularities can be included in the transmission equation.
2. If the surface is truly smooth, it can be assumed that the effect of the boundary is to supplement the original pressure field by an out-of-phase image contribution. For a randomly rough surface the reflected sound neither completely cancels the direct sound nor adds to give +6 dB pressure peaks of the interference pattern. For a rough surface, this supplement is a small fraction of the direct path.

The second approach will be used with the simplified assumption that the sea below the surface has an isotropic statistical description; i.e., the mean acoustic velocity and the mean density are assumed to be constant and have negligibly small mean square fluctuations.

The estimation of the scattering is based on an approximation method employing both ray and wave theory. Ray methods are used to follow the acoustic signal from the noise source to the vicinity of the sea surface. Then, wave theory is used to calculate the scattering process. Finally, ray theory is used to follow the scattered signal to the receiver.

The geometry is given in Fig. 24a. The origin of the coordinate system is at the center of the illuminated area. The x-y plane coincides with the mean of the rough surface as averaged over the illuminated area.

The source and receiver are at distances R_1 and R_2 , respectively, from the origin. R_1 is the xz-plane and makes the angle θ_1 with the z-axis. R_2 makes the angle θ_2 with the z-axis and the projection of R_2 on the xy-plane has an angle θ_3 relative to the x-axis.

For high frequencies R_1 and R_2 are much larger than the acoustic wavelength. Then both the incident wave and scattered waves can be treated as nearly plane waves.

The formulation of the scattering problem will be based on the Helmholtz integral which requires known values of the normal derivatives of the incident and reflected waves on the boundary. These are estimated by using the neuristic Kirchhoff's approximation, which assumes that the wave is locally reflected by a plane surface; i.e., an approximation restricted to a surface not too rough and not shadowed.

Further, the receiver directivity, as indicated by Fig. 24b, will be used to limit the surface area that is illuminated.

Since this procedure is based on a detailed development by I. Tolstoy and C. S. Clay [Ref. 15], only the main points will be outlined here to bring out the assumptions made and the inherent limitations of this approach.

The development starts by considering the inhomogeneous wave equation of the general form:

$$\nabla^2 p(\vec{x}_1, t) - \frac{1}{c^2} \frac{\partial^2 p(\vec{x}_1, t)}{\partial t^2} = -4\pi f(\vec{x}_1, t) \quad (41)$$

where

$f(\vec{x}_1, t)$ = is a known source distribution.

The development is based on the following initial assumptions:

- The medium is homogeneous.
- The medium is bounded by some surface S , onto which an incident wave impinges.

- The boundary is characterized by the specific acoustic admittance and the shape of the boundary.
- The incident wave is harmonic.

The assumed harmonic source implies that $f(\vec{x}, t)$ can be decomposed into a Fourier integral. Furthermore, assuming that the solution of Eq. (41) can be decomposed in time, we arrive at the Helmholtz equation

$$\nabla^2 p_\omega(x) + \frac{\omega^2}{c^2} p_\omega(x) = -4\pi f_\omega(x) \quad (42)$$

It should be noted here that L. Fortuin, in [Ref. 16] showed that the Helmholtz equation is not exactly correct for a medium with a time dependent boundary. The equation can, however, be used with a good approximation when the time derivative of the surface elevation is much smaller than the speed of the waves through the medium. For underwater sound waves scattered by the rough sea surface, this means that the wind speed has to be much less than the sound speed; a requirement easily fulfilled for our investigation.

Green's method allows the solution of this linear inhomogeneous wave equation to be expressed in the heuristic Helmholtz integral form:

$$p_\omega(x) = \int_V f_\omega(x^1) G_\omega(xx^1) d^3x^1 + \frac{1}{4\pi} \oint_S \left\{ G_\omega(xx^1) \frac{\partial p_\omega(x^1)}{\partial n^1} - p_\omega(x^1) \frac{\partial G_\omega(xx^1)}{\partial n^1} \right\} da^1 \quad (43)$$

The first integral on the RHS of Eq. (43) contains the sound sources and the bulk (volume) scattering. The second integral represents the surface scattering and is taken over all finite surfaces.

Now, disregarding the direct path, the signal at the receiver is given by the surface integral alone:

$$p_{\omega}^{(s)}(x_2) = \frac{1}{4\pi} \int_S \left\{ G(x_2 x^1) \frac{\partial p_{\omega}}{\partial n^1} - p_{\omega}(x^1) \frac{\partial G}{\partial n^1} \right\} da^1 \quad (44)$$

where the subscript s denotes the scattered field. In order to solve Eq. (44) the following must be done:

- Give an approximate expression for the incident wave.
- Find an appropriate Greens function.
- Make an approximation for $p_{\omega}(x^1)$ and $\partial p_{\omega}/\partial n$ at the surface.

As we already have assumed a simple harmonic source, the incident wave can be expressed as:

$$p_{\omega}^{(i)}(x^1) = \left(\frac{\Pi p c}{2\pi} \right)^{1/2} \frac{D}{R} e^{ikR} = \frac{BD}{R} e^{ikR} \quad (45)$$

where

Π : power output.

D : illumination function.

Assuming $kR \gg 1$, i.e., that the distance of the source is large compared to the wavelength, the wave in the bounded ensonified area can be considered as a plane wave

characterized by its propagation vector

$$k_i = -k \frac{\vec{x}_i}{|\vec{x}_i|}$$

thus obtaining the expression for the incident wave:

$$p_{\omega}^{(i)}(\vec{x}_1) = \frac{BD}{R} e^{ikR_1} e^{i\vec{k}_i \cdot \vec{x}_1} \quad (46)$$

Further assuming that the receiver is sufficiently far removed from the scattering area with the rest of the sea surface not contributing, then the scattering area acts as a small induced source in a free space and we can approximate the propagation of the scattered waves from the ensonified region in terms of the free field Greens function:

$$G(x_2 x_1) \approx \frac{e^{ikR_2}}{R_2} e^{-i\vec{k}_s \cdot \vec{x}_1} \quad (47)$$

where

$$k_s = k \frac{\vec{x}_2}{|\vec{x}_2|}$$

We further assume that each surface element da^1 acts as a small reflector, and that the response of da^1 to the incident wave is that of a "local reaction," i.e., independent of any other part of the ensonified area A.

Then, the Kirchhoff's approximation where it is assumed that p and $\partial p / \partial n$ vanish everywhere on the surface except at the ensonified area and that the values of p and $\partial p / \partial n$ are proportional to the incident wave, allow the scattered

"target" strength for the ensonified area to be approximated as:

$$p_{\omega}(x^1) \Big|_A = R p_{\omega}^{(i)}(x^1) \quad (48)$$

$$\frac{\partial p}{\partial n^1} \Big|_A = R \frac{\partial p^{(i)}}{\partial n^1}$$

where

p is the locally reflected wave.

R = reflection coefficient.

$$= \frac{p^1 c^1 \cos \theta - p c \cos \theta^1}{p^1 c^1 \cos \theta + p c \cos \theta^1}; \quad \frac{c}{\sin \theta} = \frac{c^1}{\sin \theta^1}$$

Finally, assuming a Gaussian illumination function:

$$D = e^{-\frac{x^2}{X^2} - \frac{y^2}{Y^2}} \quad (49)$$

where

X and Y are the effective dimensions of the illuminated area.

The scattering integral based on the Kirchhoff's approximation can be expressed as:

$$p_{\omega}^{(s)}(x_2) = -\frac{ikBe^{ik(R_1+R_2)}}{2\pi R_1 R_2} Rf(\theta_1, \theta_2, \theta_3) \iint_{-\infty}^{\infty} D e^{2i(\alpha x^1 + \beta y^1)} e^{2i\zeta(x^1 y^1)} dx^1 dy^1 \quad (50)$$

where

$$\alpha = \frac{k}{2} (\sin \theta_1 - \sin \theta_2 \cos \theta_3)$$

$$\beta = -\frac{k}{2} \sin \theta_2 \sin \theta_3$$

$$\gamma = -\frac{k}{2}(\cos \theta_1 + \cos \theta_2)$$

$\zeta(x^1 y^1)$ = surface displacement function.

The above scattering integral is then applied to a randomly rough surface where the surface displacement function ζ is a random variable assumed to be represented by a Gaussian PDF expressed as

$$W(\zeta) = \frac{1}{\sigma\sqrt{2\pi}} e^{-\zeta^2/2\sigma^2} \quad (51)$$

with zero mean and variance σ^2 .

Also, assume that the surface is slowly varying so that the signal reflects from an essentially stationary surface and that the succession of received scattered signals p_n are assumed to form a statistically independent set of sample functions from which sequence N the first and second moment of the field can be investigated. Doing so Clay and Tolstoy [Ref. 15] found that the mean reflected signal can be expressed as

$$\langle p_{\omega}^{(s)}(x_2) \rangle_{\zeta} = p_0 e^{-2\gamma^2 \sigma^2} \quad (52)$$

where

$$p_0 = p_{\omega}^{(s)}(x_2) \big|_{\zeta=0}$$

is the signal reflected by a mirror-like surface, other factors being the same.

It is seen from the above that

1. For $\sigma \rightarrow 0$, all displacements ζ have zero probability and the mean signal tends to p_0 . Furthermore, all elements contribute to the scattering coherently.
2. For $\sigma \gg k$, all displacements ζ are equally probable. There are large phase shifts between contributions from different surface elements and they tend to cancel each other and the scattering radiation is incoherent.

The second moment is defined as:

$$\langle s^2(t) \rangle \triangleq \frac{1}{T} \int_0^T s^2(t) dt = \langle pp^* \rangle_T - \langle \bar{p} \bar{p}^* \rangle_T \quad (53)$$

where

$$s^2(t) = \frac{1}{N} \left[\sum_{n=1}^N p_n^2(t) - N \langle p(t) \rangle_N^2 \right] \quad (54)$$

In this expression the operation of squaring the signal has to be considered. However, each surface element has a different ζ for a random surface. Thus, the probability of finding element $dx' dy'$ with ζ_1 , and element ζ_2 with $dx'' dy''$ is expressed in the bivariate distribution function assumed to be Gaussian and of the form:

$$W(\zeta_1, \zeta_2) = \frac{1}{2\pi\sigma^2(1-\psi^2)^{1/2}} e \left[-\frac{1}{2(1-\psi^2)\sigma^2} (\zeta_1^2 + \zeta_2^2 - 2\zeta_1\zeta_2\psi) \right] \quad (55)$$

where

$$\psi(\xi, \eta) = \frac{1}{\sigma^2} \langle \zeta_1(x'y't) \zeta_2(x''y''t) \rangle \quad (56)$$

is the cross-correlation function characterizing the surface shape.

Changing to polar coordinate leads to Eq. 6.51 of Ref. 15 where:

$$\langle s^2 \rangle_{\alpha} = \int_0^{\infty} D J_0(2\kappa r) [e^{-4\gamma^2 \sigma^2 (1-\psi)} - e^{-4\gamma^2 \sigma^2}] r dr \quad (57)$$

Here J_0 is the Bessel function of zero order and x is the transformation parameter given as

$$\kappa = \frac{\alpha}{\cos \theta}$$

As seen from Eq. (57)

1. For rough surface, $\gamma^2 \sigma^2$ is large and the second term in the bracket, the coherent part, is negligible.
2. For smooth surface, $\gamma^2 \sigma^2$ is zero and the whole bracket is zero.

Since Eq. (57) cannot be integrated directly, Clay and Tolstoy [Ref. 15] consider it for small and large $\gamma \sigma$ separately.

Thus, concentrating on the high frequency limit, Clay and Tolstoy assumed $\gamma^2 \sigma^2 \gg 1$ and showed that:

-The coherent component is negligible.

$-\langle s^2 \rangle \approx \langle pp^* \rangle$, as the means tends to zero,

$$\langle s^2 \rangle \approx \langle pp^* \rangle_{\alpha} = \int_0^{\infty} J_0(2\kappa r) e^{-4\gamma^2 \sigma^2 (1-\psi)} r dr; \quad \gamma^2 \sigma^2 \gg 1 \quad (58)$$

Equation (58) consists of the product of an oscillatory function and an exponential function. Because of the Bessel function, the main contribution to the integral is near $r=0$. Near $r=0$ the phase changes slowly and the expression can be evaluated by the method of stationary phase. Thus, the expression of ψ about $r=0$ is given as:

$$\psi \approx 1 + \psi''(0) \frac{r^2}{2} \quad (59)$$

Furthermore, Clay and Tolstoy show that $\psi''(0)$ can be related to the characteristics of the surface as:

$$|\psi''(0)| = \frac{1}{\sigma^2} \langle \zeta'^2 \rangle \quad (60)$$

Finally, Clay and Tolstoy show that the scattering signal can be expressed as:

$$\langle s^2 \rangle = \langle pp^* \rangle = \langle P_1 P_1^* \rangle \frac{A}{R_2^2} S_{hf}; \quad \begin{matrix} 4\gamma^2 \sigma^2 \gg 1 \\ (2\gamma^2 \langle \zeta'^2 \rangle) \gg \frac{1}{R^2} \end{matrix} \quad (61)$$

where

A = ensonified area

$\langle p_1 p_1^* \rangle$: the expected average value of p_1^2 , where p_1 is the incoming pressure to the illuminated area.

S_{hf} = scattering function

$$= \frac{f^2(\theta) R^2}{2\pi (\cos \theta_1 + \cos \theta_2)^2 \langle \zeta'^2 \rangle} e^{-\frac{x^2}{2\gamma^2 \langle \zeta'^2 \rangle}}$$

$$f(\theta) = f(\theta_1, \theta_2, \theta_3) = \frac{1 + \cos\theta_1 \cos\theta_2 - \sin\theta_1 \sin\theta_2 \cos\theta_3}{\cos\theta_1 + \cos\theta_2}$$

$$R = \frac{\rho^1 c^1 \cos\theta - \rho c \cos\theta^1}{\rho^1 c^1 \cos\theta + \rho c \cos\theta^1}; \quad \frac{c}{\sin\theta} = \frac{c^1}{\sin\theta^1}$$

$$\gamma = -\frac{k}{2} (\cos\theta_1 + \cos\theta_2)$$

$$\kappa = \frac{\alpha}{\cos\theta}$$

$$\alpha = \frac{k}{2} (\sin\theta_1 - \sin\theta_2 \cos\theta_3)$$

$$k = \frac{2\pi}{\lambda}$$

$$\langle \zeta^{12} \rangle = (3 + 5.12W) \times 10^{-3}; \quad W = \text{wind speed in m/s.}$$

Equation (61) is valid for:

$$4\gamma^2 \sigma^2 \gg 1$$

$$(2\gamma^2 \langle \zeta^{12} \rangle) \gg \frac{1}{R^2}$$

In summary, the reflection of high frequency signals yields scattered radiation which is incoherent. Furthermore, as pointed out by Clay and Tolstoy in [Ref. 15] although the radiation is primarily scattered in the specular direction, parts are scattered in all directions. As seen from Eq. (61) the scattering function S_{hf} is primarily dependent on the mean square slope of the surface $\langle \zeta^{12} \rangle$ and neither the mean square wave height σ^2 nor the correlation distance are important. Furthermore, it is noticeable that in the

high frequency limit the scattering function is independent of the frequency since

$$e - \frac{k^2}{(2\gamma^2 \langle \zeta^2 \rangle)} \rightarrow 1 \text{ when } r^2 \rightarrow \infty$$

C. GEOMETRICAL SHADOWING

The phenomena of shadowing of some surface areas by others has to be considered either when the surface irregularities are large with respect to the incident wavelength or when the grazing angle is small.

The few papers devoted to this subject are aimed mainly towards calculation of a "Shadowing function" based on the statistics of the surface.

An explicit method, geometrical shadowing, has been introduced by P. Bechmann [Ref. 17] where the shadowing function $S(\theta)$ is the probability that the point ζ (Fig. 25) is illuminated.

$$S(\theta) = \exp \left[- \int_0^\infty q(x) dx \right] \quad (62)$$

where:

$q(x)$ is the probability that ζ is shaded by ζ in the interval $(x, x+dx)$ given that it is not shaded in $(0, x)$.

This calculation of $S(\theta)$ only considers the elevation of the surface observation point. However, the slope also plays a role in that if its value exceeds $\cot\theta$ the point

will certainly be shaded. Thus, R. Wagner, in Ref. 18, incorporated both ζ and ζ^1 using P. Bechmann's method and found that the conditional probability that a point on the surface is illuminated, given that it has height ζ and slope ζ^1 , can be expressed as:

$$S(\theta_1 | \zeta_1, \zeta_1^1) = \exp\left[-\int_0^\infty q(x) dx\right] u(\cot\theta - \zeta^1) \quad (63)$$

where

u : is the unit step function.

$q(x)$: is the conditional probability that ζ is shadowed in the interval $(x, x+dx)$ given that it is not shadowed in $(0, x)$.

The function $q(x)$ cannot be calculated exactly. Thus, R. Wagner made the approximation that, for all x , the probability that ζ crosses the ray in dx is independent of the values of ζ and ζ^1 at $x=0$. In the above, no mention has been made of the direction of observation. However, in this respect, R. Wagner [Ref. 18] points out that in the high frequency limit only those portions of the surface which are illuminated simultaneously by rays in the direction of incidence and observation can contribute to the observed scattered power. For this condition, R. Wagner introduced both directions as independent variables in the so-called bistatic shadowing probabilities where he defines:

1. $S(\theta_1, \theta_2 | \zeta_1, \zeta_1')$ to be the conditional probability that the surface will not cross the incoming ray (Ray 1) or the outgoing ray (Ray 2) anywhere, given that both rays pass through an arbitrary point on the surface with displacement ζ and slope ζ^1 .
2. $S(\theta_1 | \theta_2, \zeta_1, \zeta_1')$ to be the conditional probability that the surface does not cross Ray 1, given that it does not cross Ray 2 and that both rays pass through the point ζ having slope ζ^1 .

Thus, the conditional shadowing function can be expressed as:

$$S(\theta_1, \theta_2 | \zeta_1, \zeta_1') = S(\theta_1 | \theta_2, \zeta_1, \zeta_1') S(\theta_2 | \zeta_1, \zeta_1') \quad (64)$$

The shadowing function is then obtained by averaging over all possible heights and slopes

$$S(\theta_1, \theta_2) = \iint_0^\infty S(\theta_1, \theta_2 | \zeta, \zeta') W(\zeta, \zeta') d\zeta d\zeta' \quad (65)$$

Here $w(\zeta, \zeta')$ is the bivariate PDF of the surface height and slope, assumed to be Gaussian

$$w(\zeta, \zeta') = \frac{1}{2\pi} (\psi_0 | \psi_0'')^{-\frac{1}{2}} \exp\left\{-\frac{\zeta^2}{2\psi_0} - \frac{\zeta^1}{2|\psi_0''|}\right\} \quad (66)$$

where $\psi_0 = \sigma^2$ and ψ'' are the values at $\tau=0$ of the correlation function and its second derivatives, respectively.

For the region $0 < \theta < \frac{\pi}{2}$ where the probability of crossing one ray is assumed independent of that of crossing the other, R. Wagner found that the bistatic shadowing function

could be expressed as:

$$S(\theta_1, \theta_2) = \frac{\{1 - \exp[-2(B_1 + B_2)]\} \times \{\operatorname{erf} v_1 + \operatorname{erf} v_2\}}{4(B_1 + B_2)} \quad (67)$$

where

$$B_i = \frac{\exp(-v_i^2) - \sqrt{\pi} v_i \operatorname{erfc} v_i}{4\pi v_i}; \quad i = 1, 2$$

$$v_i = \frac{\eta_i}{2\sigma^2 |\psi_0''|} = \frac{|\eta_i|}{2\Sigma^2}; \quad i = 1, 2$$

$$\begin{aligned} \text{as we from Eq. (60) have that } \sigma^2 |\psi''(0)| \\ = \langle \zeta^{12} \rangle = \Sigma^2 \end{aligned}$$

$$\eta_i = \cot \theta; \quad i = 1, 2$$

and noting that

$$\text{Error function } \operatorname{erf}(x) = \frac{2}{\sqrt{\pi}} \int_0^x e^{-t^2} dt$$

$$\text{Complementary error function } \operatorname{erfc}(x) = \frac{2}{\pi} \int_x^\infty e^{-t^2} dt$$

The shadowing function $S(\theta_1, \theta_2)$ is, in short, the fraction of the surface still illuminated. As seen from Eq. (60), the scattered field, in the high frequency case, is proportional to the illuminated area. Hence, the shadowing effect of a rough surface can be introduced by multiplying the ensonified area A by the shadowing function $S(\theta_1, \theta_2)$.

D. ESTIMATING THE SURFACE SCATTERING EFFECT

The following estimations are based on calculations in the specular direction, which is, as pointed out earlier, expected to give the maximum supplementary scattering effect. Hence, in the specular direction where $\theta_1 = \theta_2 = \theta$ and $\theta_3 = 0^\circ$, the scattering function S_{hf} reduces to the following expression:

$$S_{hf} = \frac{f^2(\theta) R^2}{2 (\cos\theta_1 + \cos\theta_2)^2 \langle \zeta^2 \rangle} e^{-\frac{k^2}{(2\gamma^2 \langle \zeta^2 \rangle)}} \quad (68)$$

$$S_{hf} = \frac{R^2}{8\pi \langle \zeta^2 \rangle}$$

as

$$f(\theta) = \cos\theta$$

$$\gamma = k \cos\theta$$

$$\alpha = 0$$

$$x = \frac{\alpha}{\cos\theta} = 0$$

As pointed out in the previous paragraph, the reflection of very high frequency signals by the sea surface yields scattered radiation that is incoherent under the assumption that

$$4\gamma^2 \sigma^2 \gg 1$$

$$(2\gamma^2 \langle \zeta^2 \rangle) \gg \frac{1}{R^2}$$

Before we launch into the calculations, we will verify these criteria for the frequency range of interest: 60 and 30 kHz.

Utilizing

$$\gamma^2 = k^2 \cos^2 \theta$$

$$\alpha = 8.1 \times 10^{-3}$$

$$\sigma^2 = \frac{\alpha W^4}{4\beta g^2}$$

$$\beta = 0.74$$

$$\langle \zeta^{12} \rangle = (3 + 5.12W) \times 10^{-3} \quad g = 9.81 \text{ m/s}^2$$

and assuming a windspeed of 10 m/s (SS3) yields

$$\alpha^2 = 0.30 \text{ m}^2 ; \sigma = 0.55 \text{ m}$$

$$\langle \zeta^{12} \rangle = 5.42 \times 10^{-2}$$

For 60 kHz ($\lambda = .025 \text{ m}$) and low grazing angles, e.g., $\theta = 85^\circ$

$$4\gamma^2\sigma^2 = 5.75 \times 10^2 \gg 1$$

$$(2\gamma^2\langle \zeta^{12} \rangle) = 5.2 \times 10^1 \gg \frac{1}{R^2}$$

and the first order $5.2 \gg \frac{1}{R^2}$, $R \geq 0.5 \text{ m}$.

Thus, for the 60 kHz case, the criteria are fulfilled.

For 30 kHz ($\lambda = .05 \text{ m}$) and $\theta = 85^\circ$.

$$4\sigma^2\gamma^2 = 1.44 \times 10^2 \gg 1$$

$$(2\gamma^2\langle \zeta^{12} \rangle) = 13 \gg \frac{1}{R}$$

again the first order $R > 1.0 \text{ m}$.

Thus, also for the 30 kHz case the criteria are fulfilled.

Similarly, for the shadowing function in the specular direction

$$0 < \theta_1 = \theta_2 = \theta < \pi/2 \quad \text{and} \quad \theta_3 = 0$$

we obtain the following simplified expression

$$S(\theta) = S(\theta_1, \theta_2) = \frac{[1 - \exp(-4B)] \operatorname{erfv}}{4B} \quad (69)$$

as

$$v_1 = v_2 = v = \frac{|\eta|}{(2\sigma^2 |\psi_0''|)^{\frac{1}{2}}} = \frac{|\eta|}{(2\bar{\Sigma}^2)^{\frac{1}{2}}}$$

$$\eta_1 = \eta_2 = \eta = \cot \theta$$

$$B_1 = B_2 = B = \frac{[\exp(-v^2) - \sqrt{\pi} v \operatorname{erfc} v]}{4\sqrt{\pi} v}$$

In summary, for specular scattering at the high frequency limit, the expected average value of p^2 , where p is the pressure field at the receiver, is then obtained from the following simplified expressions:

$$\langle s^2 \rangle = \langle pp^* \rangle \frac{AS(\theta)}{R_2^2} S_{hf} \quad (70)$$

$$\langle s^2 \rangle = \langle pp^* \rangle \frac{AS(\theta) R^2}{8\pi R_2^2 \langle \zeta^2 \rangle}$$

where

$$S(\theta) = \frac{1 - \exp(-4B) \operatorname{erfv}}{4B}$$

$$v = \frac{|\eta|}{(2\bar{\Sigma}^2)^{\frac{1}{2}}}$$

$$|\eta| = \cot \theta$$

$$B = \frac{[\exp(-v^2) - \sqrt{\pi} v \operatorname{erfc} v]}{4(\pi)^{\frac{1}{2}} v}$$

$$\langle \zeta^{12} \rangle = \Sigma^2 = (3 + 5.12W) \times 10^{-3} ; W = \text{windspeed in m/s.}$$

$$R = \frac{\rho^1 c^1 \cos \theta - \rho c \cos \theta^1}{\rho^1 c^1 \cos \theta + \rho c \cos \theta^1} ; \frac{c}{\sin \theta} = \frac{c^1}{\sin \theta^1}$$

From Ref. 19 we use the following air/sea water interface data:

1. For air $c' = 343$ m/s and $\rho^1 c^1 = 415$ Rayls.
2. For sea water $c = 1500$ m/s and $\rho c = 1.54 \times 10^6$ Rayls.

The estimation of the illuminated area A for specular scattering where $\theta_1 = \theta_2 = 0$ and $\theta_3 = 0$, is based on the geometry illustrated in Fig. 24b. The illuminated area is given by

$$A = \pi ab \quad (71)$$

Assuming the following data to be known

h_s = depth of the source

h_r = depth of the receiver

$\Delta\phi$ = the half beam width of the directional receiver.

Both a and b of Eq. (71) can be calculated in terms of the detection range R_D as follows:

$$x_2 = \frac{R_D h_r}{h_s + h_r} \quad (72)$$

$$x_1 = R_D - x_2 = R_D \left(1 - \frac{h_r}{h_s + h_r}\right) ; \theta = \tan^{-1} \left(\frac{R_D}{h_s + h_r}\right)$$

$$R_1 = \frac{x_1}{\sin\theta}$$

$$R_2 = \frac{x_2}{\sin\theta}$$

To a good approximation when $\theta = \pi/2$, we have

$$a = x_1 = R_D \left(1 - \frac{h_r}{h_s + h_r}\right) \quad (73)$$

$$b = R \sin(\Delta\phi) = \frac{R_D h_r}{(h_s + h_r) \sin\theta} \sin(\Delta\phi)$$

The expression for $\langle s^2 \rangle$ is then introduced as a supplement to the direct path to the receiver in the following way:

By utilizing the relationship

$$I = \frac{\overline{p^2}}{\rho c} \quad (74)$$

for the intensity, the scattering intensity at the receiver and the intensity at the ensonified area are, respectively,

$$I_s = \frac{\overline{p^2}}{\rho c} = \frac{\langle s^2 \rangle}{c}$$

$$I_1 = \frac{\overline{p_1^2}}{\rho c} = \frac{\langle p_1 p_1^* \rangle}{\rho c}$$

Equation (70) can thus be written as

$$I_s = I_1 \frac{AS(\theta) R^2}{8\pi R_2^2 \langle \zeta^{12} \rangle}$$

$$I_s/I_1 = \frac{AS(\theta) R^2}{8\pi R_2^2 \langle \zeta^{12} \rangle}$$

$$10\log I_s/I_1 = 10\log \frac{I_s/I_{ref}}{I_1/I_{ref}} = K_0$$

$$IL_s = IL(R_1) = K_0 \quad (75)$$

We then have to determine $IL(R_1)$

$$TL = SPL(1) - SPL(R_1) = 20\log R_1 \quad (76)$$

$$SPL(R_1) = IL(R_1) = 10\log I_1$$

$$SPL(1) = SL$$

yielding

$$IL(R_1) = SL - 20\log R_1 = K_1 \quad (77)$$

Then

$$IL_{suppl} = K_0 + K_1 \quad (78)$$

is the supplement to the direct path, and

$$IL_{direct} = SL - 20\log R_D = K_3$$

$$I_{direct}/I_{ref} = \text{anti log} \frac{IL_{direct}}{10} = K_4$$

$$I_{suppl}/I_{ref} = \text{anti log} \frac{IL_s}{10} = K_5$$

The total intensity of the receiver is thus

$$I_{Tot}/I_{ref} = \frac{I_{direct} + I_{suppl}}{I_{ref}} = K_4 + K_5 = K_6$$

$$IL_{Tot} = 10\log K_6 = K_7 \quad (79)$$

Thus, the effect of the randomly rough surface compared to the idealized free-field condition can be expressed as

$$\Delta IL = IL_{Tot} - IL_{direct} = K_s \quad (80)$$

A calculator program on a Texas Instrument 59 (later called TI 59) was developed to perform these calculations. A block diagram of the program is outlined in Fig. (26) and the programs steps together with a detailed description is given in Appendix B. The calculations are based on the following fixed data

$$h_s = 2 \text{ m}$$

$$h_r = 6 \text{ m}$$

$$\Delta\phi = 10^\circ$$

$$W = 10 \text{ m/s (SS3)}$$

Then, varying the detection range from $R = 2000 \text{ m}$ to 100 m gives the difference between IL_{Tot} and IL_{direct} plotted in Fig. (27).

E. CONCLUSION AND DISCUSSION

As seen from Fig. (27) the supplementary effect of the scattering from a rough surface in the high frequency case is negligible compared to the direct path.

In saying so, it also should be pointed out that the Helmholtz-Kirchhoff's approach may be limited as it does not take into account the diffraction effects from crests

and troughs of the ensonified area, an effect which becomes increasingly important at low grazing angles, high frequency and when the rough surface is a superposition of swell and capillary waves.

VII. THE EFFECT OF SCATTERING AND ABSORPTION FROM THE SUB-SURFACE OCEAN LAYER

A. GENERAL SCATTERING THEORY

Generally when a region (volume) scatters sound, some of the energy carried by the incident wave is dispersed.

The energy lost by the incident wave may be absorbed by the scatterers or it may be simply deflected from its original course. The amount of energy lost per second by the incident wave divided by the incident wave's intensity is called the total cross section σ_e of the region and is the sum of the absorption and scattering cross sections

$$\sigma_e = \frac{\pi_s + \pi_a}{I_p}$$

where

π_s = scattered power

π_a = absorbed power

The existence of gas bubbles in the subsurface ocean layer modifies the forward scattering in the following two major ways:

1. The bubbles can resonate. When the bubbles are excited at a frequency near its natural frequency, it very efficiently absorbs and scatters the incident wave. At resonance, the scattering and

absorption cross section of a typical bubble at sea is of the order 10^3 times its geometrical cross section.

2. The bubbles change the effective compressibility of the water and cause the speed of sound to be a function of frequency, i.e., the medium is dispersive.

We will investigate and discuss these effects by separately estimating:

1. The attenuation due to the bubbles and
2. the refraction by bubbles.

B. ABSORPTION MODEL

The choice of model for the subsurface ocean layer depends on whether the medium has a tenuous or a dense distribution of scatterers. When the bubble density is tenuous, both "single scattering" and "first order multiple scattering" approximation solutions are applicable.

On the other extreme, when the bubble density is high, the so-called "diffusion" approximation can be used. Between these two extremes, multiple scattering effects are important.

The multiple scattering theory, which in the limit also contains the first order approximation, will be used to estimate effects of attenuation due to bubbles, on the propagation of propeller noise from the target to the torpedo.

The geometry of the propagation model is illustrated in Fig. (28) where it is assumed that a plane wave is incident on a semi-infinite (disregarding the sea surface) slab of thickness x containing a number of randomly distributed bubbles. The plane wave approximation is valid if the incident sound has a wavelength λ much greater than the bubble-radius a

$$ka \ll 1$$

where

$$k = \omega/c = 2\pi/\lambda$$

The receiver is located outside the slab and the beam pattern of the receiver is represented by the solid angle Ω_r .

We are interested in the estimating of the total power received, taking into account the multiple scattering process in the inhomogeneous slab as well as the beam pattern of the receiver.

The mathematical formulation of this problem is based on Twersky's theory of multiple scattering. Since the theory is presented in Ref. 20 only, the basic formulation, major assumptions, and the end results will be presented here.

The total intensity is the average of the square of the magnitude of the total field:

$$\langle |\psi^a|^2 \rangle = \langle |\langle \psi^a \rangle + \psi_f^a|^2 \rangle = |\langle \psi^a \rangle|^2 + \langle |\psi_f^a|^2 \rangle \quad (81)$$

where

$$\psi^a = \psi_i^a + \sum_{s=1}^N u_s^a$$

the scalar field at the receiver location \vec{r}_a , see Fig. (29), is the sum of the incident wave ϕ_i and the contribution from all N scatterers.

$|\langle \psi^a \rangle|^2$ is the coherent intensity based on the average field $\langle \psi^a \rangle$. $\langle |\psi_f^a|^2 \rangle$ is the incoherent intensity based on the fluctuating field ψ_f^a .

In Twersky's theory, the multiple scattering process is described by the following set of integral equations which Eq. (81) must satisfy:

$$\langle |\psi^a|^2 \rangle = |\langle \psi^a \rangle|^2 + |\langle v_s^a \rangle|^2 \langle |\psi^s|^2 \rangle \rho(\vec{r}_s) d\vec{r}_s \quad (82)$$

where

$$v_s^a = U_s^a + U_t^a v_s^t \rho(\vec{r}_t) dt$$

is an operator representing all the scattering processes from s to a. (See Fig. (28).) It should be noted that Twersky's theory includes all the multiply scattered waves that involve chains of successive scattering going through different scatterers. (See Fig. (29a).) However, the theory neglects the terms which include an individual scatterer more than once, as illustrated by Fig. (29b).

Thus Twersky's theory is expected to give good results when back scattering is insignificant compared to the scattering in other directions.

As typical for most integral equations, Twersky being no exception, detailed complete solutions are difficult to obtain. However, Twersky gave an approximate solution to Eq. (81) and Eq. (82), which according to Ref. 20 have been found to agree reasonably well with experimental data. This solution is based on the following main assumptions:

- Backscattering is assumed to be small compared to scattering in other directions.
- Scattering is mostly concentrated in the forward direction. This is reasonable based on the assumed random distribution of the bubbles; i.e., no reinforcement of the radiation pattern occurs except in the direction of the incident wave.
- The angle θ_{as} is small, i.e., $\theta_{as} = 0^\circ$.

This leads to the following expression for the total intensity at the receiver:

$$\begin{aligned} \langle |\psi^a|^2 \rangle = T = & \exp(-\rho\sigma_a x) \exp(-\rho\sigma_s x) \\ & + q[1 - \exp(-\rho\sigma_s x)] \end{aligned} \quad (83)$$

where

- σ_a = absorption cross section
- σ_s = scattering cross section

$$q = \frac{\int_{\Omega_r} |f|^2 d\Omega_s}{4\pi \int |f|^2 d\Omega_s}$$

where

f = the amplitude function

q = the fraction of total scattered power collected by the receiver as illustrated in Fig. 30 and

ρ = is the bubble density, i.e., the number of scatterers per unit volume.

For small values of ρx we see from Eq. (82) that the coherent part dominates:

$$\ln T \approx -(\sigma_a + \sigma_s) \rho x \quad (84)$$

In this limit the multiple scattering result is equivalent to that obtained from single scattering considerations.

For large values of ρx which corresponds to very dense or very wide slab of scatterers, the incoherent intensity dominates

$$\ln T \approx \ln q - \sigma_a \rho x \quad (85)$$

In this latter case, it is notable that when $\Omega_r \geq 2\pi$, the receiver collects almost all the scattered power

$$\ln T \approx -\sigma_a \rho x \quad (86)$$

The first case, representing the situation for tenuous density of scatterers and/or narrow beam pattern of the receiver, gives a good approximation to the situation of interest in the thesis. It also represents the case for

which no scattered power is received. This will be approximately true for a narrow-beam width receiver. We will, therefore, investigate the coherent intensity first.

Also, the incoherent case, as represented by Eq. (86) will be investigated, where only losses due to absorption are incorporated.

C. THE COHERENT INTENSITY CASE

For the coherent case the intensity level after the incident wave has traversed a distance x is

$$I_x = I_p \exp[-(\sigma_a + \sigma_s) \rho x] \quad (87)$$

where

I_p = incident plane wave intensity.

The change in intensity over the distance x is

$$\begin{aligned} \Delta IL &= 10 \log \frac{I_x}{I_p} = \frac{I_p \exp [-(\sigma_a + \sigma_s) \rho x]}{I_p} \\ &= 10 \log \exp [-(\sigma_a + \sigma_s) \rho x] \end{aligned} \quad (88)$$

The excess attenuation per unit distance due to bubbles is thus

$$\begin{aligned} \alpha &= - \frac{\Delta IL}{x} = - \left[\frac{-(\sigma_a + \sigma_s) \rho x \log e}{x} \right] \\ &= (\sigma_a + \sigma_s) \rho \log e \\ \alpha &= 4.34 \sigma_e \rho, \text{ in dB/m.} \end{aligned} \quad (89)$$

However, this only takes into account bubbles of one size. In a bubbly medium there is a spectrum of radii.

The probability density function for finding a bubble size between radii a and $a+da$ is

$$W(a) = \frac{n(a)}{\rho} \quad (90)$$

where

$$\int_0^{\infty} W(a) da = 1$$

$n(a)da$ is the number of bubbles per unit volume having radii between a and $a+da$. It is common to use $da=1 \mu m$.

$$\rho = \int_0^{\infty} n(a) da \text{ is the total number of bubbles per unit volume.}$$

As the extinction cross section also is a function of the radius (See Eq. (93).), the absorption due to bubbles is obtained by integrating Eq. (89) over all possible radii

$$\alpha = 4.34 \int_0^{\infty} \sigma_e(a) n(a) da \quad (91)$$

To calculate the absorption coefficient, the extinction cross section σ_e must be derived from the general bubble dynamic relationship. This is done in detail by C. Clay and H. Medwin [Ref. 21] from which the following results are taken.

The scattering cross section

$$\sigma_s = \frac{\Pi_s}{I_p} \quad (92)$$

$$= \frac{4\pi a^2}{[(f_r/f)^2 - 1]^2 + \delta^2}$$

where

$$f_r = \text{resonance frequency} = \frac{1}{2\pi a} \left(\frac{2\gamma b \beta P_A}{\rho_A} \right)^{1/2}$$

$$f = f_o = \text{operating frequency}$$

$$\delta = \text{damping constant} = \delta_r + \delta_t + \delta_v$$

$$= ka + \left(\frac{d}{b} \right) \left(\frac{f_r}{f} \right)^2 + \frac{4\mu}{\rho_A \omega a^2}$$

$$a = \text{bubble radii}$$

$$\frac{d}{b} = 3(\gamma-1) \left[\frac{\bar{X}(\sin h \bar{X} + \sin \bar{X}) - 2(\cos h \bar{X} - \cos \bar{X})}{\bar{X}^2(\cos h \bar{X} - \cos \bar{X}) + 3(\gamma-1)(\sin h \bar{X} - \sin \bar{X})} \right]$$

$$\bar{X} = a \left(\frac{3\omega \rho_g C_{pg}}{k_g} \right)^{1/2}$$

$$k_g = \text{thermal conductivity of gas}$$

$$\rho_g = \text{density of gas} = \rho_{gA} \left[1 + \frac{2\tau}{(\rho_A a)} \right] (1+0.1z)$$

$$\rho_{gA} = \text{density of gas at sea level}$$

$$\tau = \text{surface tension}$$

$$P_A = 1.013 \times 10^6 (1+0.1z)$$

$$z = \text{bubble depth in m.}$$

$$C_{pg} = \text{specific heat of constant pressure of gas}$$

μ = shear viscosity of water

$\gamma = 7/5$, for diatomic gas

ρ_A = density for sea water

$$b = [1 + (\frac{d}{b})^2]^{-1} [1 + \frac{3\gamma-1}{\bar{X}} \frac{\sin h \bar{X} - \sin \bar{X}}{\cos h \bar{X} - \cos \bar{X}}]^{-1}$$

$$\beta = 1 + \frac{2\tau}{P_A a} (1 - \frac{1}{3\gamma b})$$

Furthermore:

$$\sigma_e = \sigma_a + \sigma_s = \frac{4\pi a^2 (\delta/ka)}{[(f_r/f)^2 - 1]^2 + \delta^2} \quad (93)$$

and

$$\sigma_a = \sigma_e - \sigma_s \quad (94)$$

A detailed computer program, as outlined in Appendix B, was developed for the TI 59 to handle the derivation of σ_s , σ_e , and σ_a based on an assumed receiver depth of $z = 6$ m.

For the 60 kHz case, both the extinction cross section σ_e and the absorption cross section σ_a are given in Fig. 31 as a function of bubble radius a .

Similarly, Fig. 32 gives σ_e and σ_a for the 30 kHz case. Superimposed on these figures are the curves for $n(a)da$ as calculated from the following: Figures 5 - 7 of Ref. 2 give the resonant bubble densities in a 1 μ m band as a function of depth and with the wind speed as parameter for the three discrete frequencies 12 kHz, 38 kHz and 120 kHz.

Based on these data, Fig. 33 shows the interpolated bubble density as a function of resonance frequency for sea state 2, 3, and 6.

Furthermore, both A. Lövik [Ref. 2] and H. Medwin [Ref. 3] found that the bubble density function $n(a)$ decreases with increasing bubble radii as

$$n(a) \propto a^{-x}$$

where H. Medwin [Ref. 3] found the power law of:

$$x = 4 \text{ for } a < 50\text{--}80 \text{ } \mu\text{m}.$$

$$x = 2 \text{ for } a > 50\text{--}80 \text{ } \mu\text{m}.$$

and A. Lövik [Ref. 2] found the power law of:

$$x = 4.2 \text{ between } 38 \text{ kHz and } 120 \text{ kHz}$$

$$x = 2.6 \text{ between } 12 \text{ kHz and } 38 \text{ kHz}$$

which, averaged over the depth interval, corresponds to the bubble radii of 380 μm (12 kHz), 120 μm (38 kHz) and 49 μm (120 kHz).

As suggested by A. Lövik [Ref. 2], the discrepancy between the two observations is not great and may be due to the few measuring frequencies used in the work of A. Lövik.

In summary, Fig. 33, from which we obtain the appropriate resonant bubble density in a 1 μm band $n(a_R)$ together with the power law $n(a) \propto a^{-x}$, comprise the full knowledge of $n(a)da$.

Performing a multiplication of σ_e and $n(a)da$, we obtain Fig. 34 and Fig. 35 for the 60 kHz and the 30 kHz case, respectively.

Finally, the integral

$$\int_0^{\infty} \sigma_e(a)n(a)da$$

was evaluated using a numerical integration based on Simpson's discrete approximation programmed for the TI 59 and documented in Appendix C.

Based on the above, the following absorption coefficient for the coherent case is obtained for $f = 60$ kHz

$$\begin{aligned} \alpha &= 4.34 \int_0^{\infty} \sigma_e(a)n(a)da = 4.34 (2.016 \times 10^{-1}) \\ &= 8.75 \times 10^{-1} \text{ dB/m.} \end{aligned}$$

$$\alpha \approx 0.88 \text{ dB/m} \quad (95)$$

with

$$n(a_R) = 1000$$

$$n(a) \propto a^{-4}$$

$$z = 6 \text{ m.}$$

Thus, it is seen that the attenuation due to bubbles is considerably greater than the "normal attenuation" due to chemical and viscous relaxation processes in sea water, which for the 60 kHz case is

$$\alpha = 0.02 \text{ dB/m.}$$

Thus, the total absorption coefficient for the 60 kHz case is

$$\alpha \approx 0.90 \text{ dB/m.} \quad (96)$$

For $f = 30 \text{ kHz}$, the absorption coefficient due to bubbles in the coherent case is

$$\begin{aligned} \alpha &= 4.34 \int_0^{\infty} \sigma_e(a) n(a) da = 4.34 (3.8375 \times 10^{-2}) \\ &= 1.665 \times 10^{-1} \text{ dB/m.} \\ \alpha &\approx 0.17 \text{ dB/m} \end{aligned} \quad (97)$$

with

$$\begin{aligned} n(a_R) &= 20 \\ n(a) &\propto a^{-2.6} \\ z &= 6 \text{ m.} \end{aligned}$$

For this case, the power law dependence of $n(a) \propto a^{-2}$ gives

$$\alpha \approx 1.655 \times 10^{-1}$$

Thus, the difference in power law dependence makes no significant difference in the absorption coefficient.

The absorption coefficient due to chemical and viscous relaxation processes is at 30 kHz

$$\alpha \approx 0.012 \text{ dB/m.}$$

The total absorption coefficient in the coherent case is

$$\alpha \approx 0.18 \text{ dB/m.} \quad (98)$$

D. THE INCOHERENT INTENSITY CASE

For the incoherent case, where only losses due to absorption are included, the product σ_a and $n(a)da$ for the 60 kHz and 30 kHz cases are given in Fig. 36 and Fig. 37, respectively. Performing a numerical integration based on the Simpson's discrete approximation leads to the following results:

For $f = 60$ kHz, the absorption coefficient due to bubbles is

$$\alpha = 4.34 \int_0^{\infty} \sigma_a(a) n(a) da = 4.34 (1.66 \times 10^{-1})$$
$$\alpha \approx 0.72 \text{ dB/m.} \quad (99)$$

with

$$n(a_R) = 1000$$

$$n(a) \propto a^{-4}$$

$$z = 6 \text{ m.}$$

Adding the "normal attenuation" in sea water for $f = \text{kHz}$, yields a total absorption coefficient of

$$\alpha \approx 0.74 \text{ dB/m} \quad (100)$$

For $f = 30$ kHz, the absorption coefficient due to bubbles is

$$\alpha = 4.34 \int_0^{\infty} \sigma_a(a) n(a) da = 4.34 (2.975 \times 10^{-2}) \quad (101)$$

$$\alpha \approx 0.13 \text{ dB/m}$$

with

$$n(a_R) = 20$$

$$n(a) \propto a^{-2}$$

$$z = 6 \text{ m.}$$

Adding the "normal attenuation" in sea water for $f = 30 \text{ kHz}$ yields a total absorption coefficient in the incoherent case of

$$\alpha \approx 0.14 \text{ dB/m} \quad (102)$$

E. SUMMARY AND DISCUSSION OF THE BUBBLE ATTENUATION

As seen from the above, the attenuation due to bubbles in the subsurface ocean layer is important for high frequency and high Sea State.

Accounting for the effect of bubbles at Sea State 3 in summary we found the following absorption coefficients in dB/m:

| $f = 60 \text{ kHz}$ | | $f = 30 \text{ kHz}$ | |
|----------------------|-----------------|----------------------|-----------------|
| coherent | incoherent | coherent | incoherent |
| $\alpha = 0.88$ | $\alpha = 0.72$ | $\alpha = 0.17$ | $\alpha = 0.13$ |

The main assumptions were:

- the back scattering is small compared to that in other directions.
- the scattering is mostly concentrated in the forward direction.

- the angle θ_{as} between the scatterer and the receiver is small, i.e., $\theta_{as} \approx 0^\circ$.
- the depth of the receiver is $z = 6$ m.
- the sea state is 3.

The range dependent portion of the passive sonar Eq. (1) $TL = -20\log R - \alpha R$ for both the 60 kHz and 30 kHz scattering results can now be compared with the reference data obtained in Section V.

For $f = 60$ kHz, Fig. 22 gives $TL = -20\log R - \alpha R$ as a function of R with

1. $\alpha = 0.021$ dB/m, the "normal attenuation" due to chemical and viscous relaxation processes.
2. $\alpha = 0.9$ dB/m, the total attenuation including the effect of bubbles in the coherent case.
3. $\alpha = 0.74$ dB/m, the total attenuation including the effect of bubbles in the incoherent case.

For the same example as in the reference model, Fig. 22 yields the detection ranges for 60 kHz.

$$R = 1200 \text{ m for } \alpha = 0.021 \text{ dB/m} \quad (103)$$

$$R = 60 \text{ m for } \alpha = 0.90 \text{ dB/m}$$

$$R = 70 \text{ m for } \alpha = 0.74 \text{ dB/m}$$

Not surprisingly, this result seems to exclude the possibility of having both a searching and attack depth near the surface, i.e., $z = 6$ m, for a torpedo system operating in a high frequency region, $f = 60$ kHz.

Similarly, for $f = 30$ kHz, Fig. 23 gives $TL = -20 \log R - \alpha R$ as a function of R with

1. $\alpha = 0.012$ dB/m, the "normal attenuation" in sea water.
2. $\alpha = 0.18$ dB/m, the total attenuation including the effect of bubbles in the coherent case.
3. $\alpha = 0.14$ dB/m, the total attenuation including the effect of bubbles in the incoherent case.

For the same detection example as in the reference model, Fig. 23 yields the detection ranges for 30 kHz:

$$R = 2400 \text{ m for } \alpha = 0.012 \text{ dB/m} \quad (104)$$

$$R = 250 \text{ m for } \alpha = 0.18 \text{ dB/m}$$

$$R = 310 \text{ m for } \alpha = 0.14 \text{ dB/m.}$$

Again, the bubbles give a major decrease in the detection range. A detection range of $R = 250$ m seems marginally acceptable as the turn rate requirement for a pursuit homing trajectory may become excessive.

The above results are summarized in Tables III and IV for the 60 kHz and 30 kHz, respectively.

F. THE REFRACTION BY BUBBLES

The presence of bubbles in the sea water affects the speed of sound (phase speed) primarily because of the change in compressibility. The derivation of this dispersive relationship on the sound speed has been done by H. Medwin

TABLE III
DETECTION PARAMETERS AND RANGES FOR $f=60$ kHz

| SL | DI | NL | P_D | P_{FA} | DT | Detection Range (m) | | SS | f |
|-----|------|------|-------|------------|------|---------------------|-------------|--------------|------|
| dB | dB | dB | | | dB | $\alpha=.021$ | $\alpha=.9$ | $\alpha=.74$ | kHz |
| 100 | -180 | -124 | .5 | 10^{-6} | -6.5 | 1200 | 60 | 70 | 3 60 |
| 100 | -180 | -124 | .5 | 10^{-99} | 0 | 1000 | -- | -- | 3 60 |

TABLE IV

DETECTION PARAMETERS AND RANGES FOR $f=30$ kHz

| SL | DI | NL | P_D | P_{FA} | DT | Detection Range (m) | | SS | f |
|-----|------|------|-------|------------|------|---------------------|--------------|-----|-----|
| dB | dB | dB | | | dB | $\alpha=.012$ | $\alpha=.14$ | | kHz |
| 106 | -180 | -124 | .5 | 10^{-6} | -6.5 | 2400 | 250 | 310 | 3 |
| 106 | -180 | -124 | .5 | 10^{-99} | 0 | 2200 | 220 | 290 | 3 |

[Ref. 22]. H. Medwin showed that the bubbles with resonant frequencies greater than the incident frequency decrease the sound speed, while bubbles with resonant frequency lower than the incident wave increase the sound speed.

Furthermore, H. Medwin [Ref. 22] predicts the sound speed gradient due to bubbles as a function of depth for a frequency range and wind speed compatible with our domain of interest.

He found the gradients

$$g = \partial c / \partial z = 0.26 \text{ s}^{-1} \text{ at } z = 0 \text{ m.}$$

$$g = \partial c / \partial z = 0.016 \text{ s}^{-1} \text{ at } z = 10 \text{ m.}$$

$$g = \partial c / \partial z = 0.005 \text{ s}^{-1} \text{ at } z = 20 \text{ m.}$$

For comparison, the sound speed gradient due to pressure in an isothermal water is

$$g = 0.017 \text{ s}^{-1}$$

This shows that the rays in the top 10 m are strongly influenced by bubbles. However, with respect to our surface scattering model (Section VI) where both the source and the receiver are situated very close to the surface and where relatively short propagation distances are encountered, this refraction phenomenon is assumed to have negligible effect.

VIII. THE TURN RATE LIMITATION

As pointed out in the previous section, the presence of bubbles near the surface may significantly reduce the range at which the target can be detected.

In this section, the turn rate necessary during pursuit homing at the previous estimated detection ranges will be studied. A computational procedure will be used to determine the range of angles on the bow (AOB) of the target at the beginning of homing which lead to miss on the initial attack. A trajectory where the torpedo velocity vector always is directed towards the instantaneous target position is called a pursuit homing trajectory. The derivation of the pursuit homing trajectory follows P. van Nostrand [Ref. 23] and is based on the geometry of Fig. 38, where

r = approach angle, i.e., angle between ship velocity vector and the line of sight.

$$\text{AOB} = 180 - \phi$$

The equation of motion is obtained by taking the component along r and the normal to r , yielding

$$\dot{r} = V_S \cos \phi - V_T \quad (105)$$

$$r\dot{\phi} = -V_S \sin \phi \quad (106)$$

where

\dot{r} = range rate

$\dot{\phi}$ = turn rate

V_S = target speed

V_T = torpedo speed.

Dividing Eq. (105) by Eq. (106) yields:

$$\frac{\dot{r}}{r} = \left(\frac{V_T}{V_S} \frac{1}{\sin \phi} - \cot \phi \right) \dot{\phi} ; r \neq 0$$

and defining

$$\frac{V_T}{V_S} \triangleq P$$

yields

$$\frac{\dot{r}}{r} = \left(\frac{P}{\sin \phi} - \cot \phi \right) \dot{\phi} \quad (107)$$

$$r = K \frac{(\sin \phi)^{P-1}}{(1 + \cos \phi)^P} \quad (108)$$

Then, introducing the initial conditions: r_0, ϕ_0 where

r_0 : initial detection range

ϕ_0 : initial approaching angle

yields

$$K = r_0 \frac{(1 + \cos \phi_0)^P}{(\sin \phi_0)^{P-1}} \quad (109)$$

For the geometry of Fig. 38, the turning rate is given by Eq. (105).

$$\dot{\phi} = -\frac{V_s}{r} \sin \phi \quad (110)$$

Substituting Eq. (108) into Eq. (110) yields:

$$\dot{\phi} = -\frac{V_s (1+\cos \phi)^P}{K(\sin \phi)^{P-2}} \quad (111)$$

From Eq. (108) we see that $r \rightarrow 0$ as $\phi \rightarrow 0$, i.e., ϕ tends to zero as the torpedo approaches the target ship. It is further of interest to determine the limiting value of the turning rate as the torpedo approaches the target for various values of the parameter p . This is done by taking the derivative of $\dot{\phi}$ with respect to ϕ . Thus, from Eq. (109) we get

$$\frac{d\dot{\phi}}{d\phi} = -\frac{V_s}{K} (\sin \phi)^{1-P} [1+\cos \phi]^P [2 \cos \phi - p] \quad (112)$$

For $1 < p < 2$, we see that Eq. (112) is zero at

$$\cos \phi = p/2 \quad (113)$$

$$\phi = \cos^{-1}(p/2)$$

with an associated maxima

$$|\dot{\phi}_{\max}| = \frac{V_s (1+p/2)^P [1-(p/2)^2]^{1-P/2}}{K} \quad (114)$$

Furthermore, the turn rate for $p < 2$ at impact is zero as the limit of Eq. (109) yields:

$$\lim_{\phi \rightarrow 0} \dot{\phi} = -\frac{V_s}{K} \lim_{\phi \rightarrow 0} (\sin \phi)^{2-P} [1+\cos \phi]^P \rightarrow 0 \quad (115)$$

For $p=2$ we see from Eq. (111) that

$$\lim_{\phi \rightarrow 0} \dot{\phi} = - \frac{V_s}{K} \lim_{\phi \rightarrow 0} (1 + \cos \phi)^2 = - \frac{4V_s}{K} \quad (116)$$

For $p>2$ we see from Eq. (111) that there is no zero value of $d\dot{\phi}/d\phi$ between $\phi = 0^\circ$ and $\phi = 180^\circ$, since all terms of Eq. (112) are nonzero terms for $0^\circ < \phi < 180^\circ$. Furthermore, the turn rate for $p>2$ at impact is

$$|\lim_{\phi \rightarrow 0} \dot{\phi}| = \left| - \frac{V_T}{K} \lim_{\phi \rightarrow 0} \frac{(1 + \cos \phi)^P}{(\sin \phi)^{P-2}} \right| \rightarrow \infty \quad (117)$$

as $(\sin \phi) \rightarrow 0$ since $(p-2)>0$.

Furthermore, as $\phi \rightarrow 180^\circ$, we get from Eq. (112)

$$\lim_{\phi \rightarrow 180} \frac{d\dot{\phi}}{d\phi} = \frac{V_O}{K}(2+p) \lim_{\phi \rightarrow 180} (\sin \phi)^{1-P} (1 + \cos \phi)^P$$

Evaluating

$$\lim_{\phi \rightarrow 180} (\sin \phi)^{1-P} (1 + \cos \phi)^P = \lim_{\phi \rightarrow 180} (\sin \phi) \left(\frac{1 + \cos \phi}{\sin \phi} \right)^P$$

by applying l' Hopitale rule to the term

$$\lim_{\phi \rightarrow 180} \frac{1 + \cos \phi}{\sin \phi} = \lim_{\phi \rightarrow 180} \frac{-\sin \phi}{\cos \phi} \rightarrow 0$$

Thus, the product $\sin \phi \left(\frac{1 + \cos \phi}{\sin \phi} \right)^P$ approaches zero for any $p>1$, since both terms in this product approach zero as $\phi \rightarrow 180$.

Figure 39 shows a plot of computed values of $|\dot{\phi}K/V_s|$ for different values of $p > 1$. From this we can draw the following summarizing conclusions.

For $1 < p < 2$ the turn rate has

- a maximum value at $\phi = \cos^{-1}(p/2)$
- the zero value at $\phi = 0^\circ$ and $\phi = 180^\circ$.

For $p = 2$ the turn rate

- is zero at $\phi = 180^\circ$.
- monotonically increasing with decreasing ϕ approaching the value $(4V_s/K)$ when $\phi = 0^\circ$.

For $p > 2$ the turn rate

- is zero at $\phi = 180^\circ$.
- is monotonically increasing with decreasing ϕ approaching ∞ as $\phi = 0^\circ$.

As seen from the above for $p > 2$, the turn rate increases monotonically with decreasing ϕ approaching an infinite turn rate to hit a point target. To avoid this singularity we must make some provision. If the torpedo's maximum turn rate is exceeded only at some very small range, a hit is likely.

Figure 40 illustrates the hit criterion used. Assume a rudder of length L_R is situated directly behind the propeller which is idealized as an acoustic point source.

If the torpedo becomes turn rate limited at some range $r = r'$, it at best can proceed along a circular path which lags the desired pursuit trajectory, or at worst it can

loose acoustic contact and go into "hold-in," maintaining a constant heading at the angle ϕ' . In this last case, it will cross the line of target ship's course in the time:

$$t = r'/V_r \quad (118)$$

If this advance is less than the length of the rudder L_R , the torpedo will impact the rudder. Hence, the limiting condition is

$$\frac{r'}{p} = L_R$$

$$r' = pL_R \quad (119)$$

For this analysis, we have arbitrarily chosen

$$L_R = 3 \text{ m} \quad (120)$$

Thus, the torpedo's turn rate has not been exceeded when the range to the target is

$$r' = pL_R = 3 p \quad (121)$$

and a hit is assumed.

Now we can analyze the cases $p > 2$ and $1 < p < 2$ on the same footing. If we match the torpedo's maximum turn rate to a particular range r' , it is certain that its turn rate has not been exceeded earlier in the run.

This turn rate-range matching is done by substituting the "hit-range" defined as $r' = 3 p$ into Eq. (106) and solving it for $\sin \phi$, yielding

$$\dot{\phi}_{\max} = - \frac{V_s}{3p} \sin \phi$$

$$\sin \phi = - \frac{\dot{\phi}_{\max}(3p)}{V_s}$$

Since $\dot{\phi}$ is always negative, $\sin \phi$ is always positive and equal to

$$\sin \phi = \frac{3p|\dot{\phi}|_{\max}}{V_s} \quad (122)$$

Two values of ϕ satisfies this equation, and they are denoted

$$\phi_A = \sin^{-1} \frac{3p|\dot{\phi}|_{\max}}{V_s}; \text{ for } \phi \leq 90^\circ \quad (123)$$

$$\phi_B = 180^\circ - \phi_A$$

A unique value of K may now be found using Eq. (111) for each of the angles ϕ_A and ϕ_B .

$$K = \frac{V_s (1 + \cos \phi)^P}{|\dot{\phi}|_{\max} (\sin \phi)^{P-2}}$$

These values of K are designated as K_A and K_B , and for each there is a corresponding value of ϕ_0 from Eq. (109) with ϕ_0 given by the initial detection range

$$(\phi_0)_A \text{ and } (\phi_0)_B$$

In the case of $1 < p < 2$, the turn rate does not necessarily increase monotonically during the pursuit homing trajectory, and we must check that either ϕ_A or ϕ_B , respectively, is not beyond the angle corresponding to $\dot{\phi}_{\max}$.

AD-A105 756

NAVAL POSTGRADUATE SCHOOL MONTEREY CA
THE EFFECT OF SCATTERING AND ABSORPTION ON NOISE FROM A CAVITAT--ETC(U)
JUN 81 Y D TRONSTAD

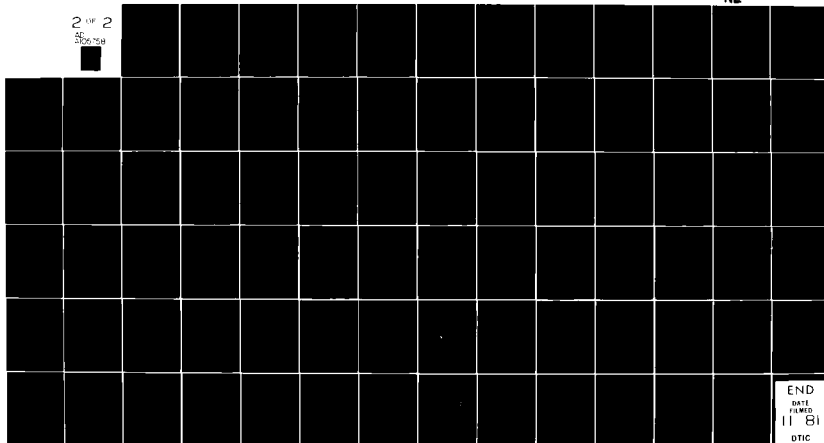
F/G 20/1

UNCLASSIFIED

NL

2 OF 2

SC 350-756



END

DATE

FILMED

11 81

DTIC

As seen from Eq. (113), the turn rate reaches a maximum at an angle given by

$$\phi^* = \cos^{-1}(P/2)$$

with a corresponding turn rate given by

$$|\dot{\phi}|_{\max} = \frac{V_s (1+P/2)^P [1-(P/2)^2]^{1-P/2}}{K}$$

Thus, the value of $K = K^*$ for which the limiting turn rate is achieved

$$K = \frac{V_s (1+P/2)^P [1-(P/2)^2]^{1-P/2}}{|\dot{\phi}|_{\max}}$$

It is important to note that, if $\phi_A < \phi^* < (\phi_O)_A$, the "A" trajectory is invalid since the maximum turn rate of the torpedo, reached at the range $r = 3p$ at $\phi = \phi_A$ is exceeded earlier in the trajectory. In that case, the limiting trajectory is the "*" trajectory. Along the same lines, we argue that the "B" trajectory always is a limiting trajectory, since the equality $\phi_B < \phi^* < (\phi_O)_B$ cannot be satisfied. This follows from the fact that

$$0^\circ < \phi^* < 90^\circ$$

and $\phi_B > 90^\circ$ as ϕ_B is the supplement of ϕ_A .

Below some critical ship speed, the torpedo will not be turn rate limited. This speed is obtained when the trajectory is normal to the ship's velocity vector, $\phi = 90^\circ$, at a range of $r = 3p$.

Thus, from Eq. (106), we obtain

$$(3p) |\dot{\phi}|_{\max} = (V_s)_{NL} \sin 90^\circ$$

yielding

$$(V_s)_{NL} = (3p) |\dot{\phi}|_{\max} \quad (124)$$

Then introducing $p = V_T / (V_s)_{NL}$, we get

$$(V_s)_{NL} = [3V_T |\dot{\phi}|_{\max}]^{1/2} \quad (125)$$

Furthermore, we see from Eq. (108) that for $\phi = 90^\circ$

$$(K)_{NL} = 3p \quad (126)$$

Again, by probing Eq. (88) we can obtain the corresponding values of ϕ_o , designated $(\phi_o)_{NL}$, where the subscript "NL" is used to indicate the "no-limit" boundary point.

The computational procedure is based on:

1. Assuming a torpedo speed $V = 35$ kts.
2. Using an initial detection range (beginning of homing) $r_o = 250$ m.
3. Assuming the following maximum turn rates:

| | | |
|-----------|-----------|-----------|
| a. 8 o/s | b. 12 o/s | c. 16 o/s |
| d. 24 o/s | e. 36 o/s | f. 48 o/s |
4. The following range of target speeds

$$0 < V_s < 25 \text{ kts}$$

The aim of the computation is to determine whether the limiting ϕ_o , and hence AOB, is governed by ϕ^* or by the turn rate at the range $r = 3p$.

The calculations are divided into two parts, and are performed on a TI 59 calculator.

For a given ship speed, Part I gives the sequential calculations of ϕ_A , K_A , ϕ_B , K_B , O^* and K^* for each of the turn rates. The computer program is given in Appendix E.

Then, in Part II, the probe calculation for $(\phi_O)_A$, $(\phi_O)_B$, $(\phi_O)^* = (\phi_O)_{A,B,*}$ are performed. The program is given in Appendix E.

The limiting results are given on a polar plot, Fig. 41 with

$$(AOB)_{A,B,*} = 180^\circ - (\phi_O)_{A,B,*}$$

As seen from Fig. 41, for a target speed of 15 kts, we need $AOB > 85^\circ$ at ϕ_O for a maximum turn rate 16 o/s in order to have a hit at the first attack.

IX. CONCLUSIONS AND RECOMMENDATIONS

The detection performance of a passive homing torpedo used against shallow-draft surface ships operating in moderate sea states was investigated. Attention was focused on the effects of scattering from the randomly rough sea surface and scattering and absorption from the bubble-dominated inhomogeneous layer just below the sea surface. The effects of these two scattering mechanisms were separately estimated and their relative importance were compared.

The passive sonar equation was used to predict the performance of the homing system, and the detection range considering these two scattering effects was obtained and compared to the detection range based on a reference model. An idealized propagation model was used as reference of comparison. This reference model was based on a noise source model for a cavitating propeller, the operational characteristics for a square-law detector, and a transmission model associated with a homogeneous, unbounded medium.

Due to high frequency, moderate sea state and low grazing angles, the scattering from the randomly rough sea surface was found to be dominated by the direct path.

This result includes effects from geometrical shadowing.

The effect of scattering and absorption from the bubble-dominated, inhomogeneous subsurface layer was investigated using multiple scattering theory. Both the coherent and incoherent limits were investigated by incorporating the associated absorption coefficient into the transmission equation.

The effect on the sound speed from the bubble content was found to be negligible.

At the assumed depth setting of 6 m for the torpedo's search and attack phase, the scattering from the bubbles increased the transmission loss. This increase depended on the frequency and the wind speed.

Two operating frequencies were investigated, 60 kHz and 30 kHz. For both cases, bubbles significantly decreased the detection range.

For a torpedo system operating at the high frequencies, e.g., 60 kHz, the result indicates the inadvisability of using a searching and attack depth near the surface, i.e., $z = 6$ m.

For an operating frequency around 30 kHz, the calculated detection ranges is such that the turn rate requirements for a pursuit homing trajectory become excessive. For a maximum turn rate of 16 o/s, this limitation can be avoided

by adapting a tactical procedure where the angle on bow (AOB) at the beginning of the torpedo attack is greater than 85° .

At sea state 3, the results show a consistent and general trend towards the need for lower operating frequency in order to increase the detection range. An operating frequency below 30 kHz seems indicated.

Furthermore, a search depth below the bubble-dominated subsurface layer, i.e., $z > 15-20$ m would result in an increased detection range.

To reduce the operational limitations induced by the scattering and absorption effects, a high maximum turn rate together with a variable speed capability, where $p \leq 2$ would be beneficial.

The result of this analysis has clearly demonstrated the importance of environmental factors on the torpedo capability, and is useful in giving insight into the behavior of a homing torpedo during its critical attack phase.

A valuable follow-on of this study would be an investigation of the effects of the bubble-dominated subsurface layer on target validation and pitch plane steering when the torpedo search depth is 50-60 m.

APPENDIX A

DETAILED OCEANOGRAPHIC BACKGROUND MATERIAL

A. GEOGRAPHIC DESCRIPTION

The Norwegian coastal waters constitute the eastern boundary of the Norwegian Sea. Although some general aspects related to the Norwegian Sea will be covered, this analysis will be concentrated on the Norwegian coastal waters above 68°N.

B. WIND

The northern region of the Norwegian Sea is affected by the Polar Easterlies and the southern region by the prevailing Westerlies. There are two dominant air masses which are relatively permanent:

- The Greenland high.

- The Iceland low.

These pressure systems produce storms which are carried across the Norwegian Sea in a belt from Iceland towards the Norwegian Coast causing steady precipitation and wind most of the year. The steep Norwegian Coast has a considerable influence on the winds and consequently also on the waves in the coastal waters. The main general modifications are that the streamlines tend to run parallel

to the coast and that wind and sea increases with distance from the sheltered coast into open ocean.

Strong local variation may occur. The most important of these are the marked local increase in wind speed in areas where the coast sharply changes direction. One such "corner effect," caused by the confluence of the streamlines, occurs near "Nordkapp" (North Cape). Also of importance are monsoonal effects due to the different heat capacities between the ocean and the continent. Drainage of cold air from the inland valleys in the wintertime causes a marked increase in the wind speed in several areas along the coast. Most of these coastal effects are significantly dissipated at distances of approximately 50 nmi. from the coast. The fact that the wind tends to blow along the coast is clearly demonstrated in Figs. 12 and 13 which include data from weather stations from "Hillesøy" to "Ona" and "Myken" to "Furuholmen" respectively. The high frequency of offshore winds is caused by the drainage of cold air from the inland valleys during winter time. That this phenomenon is closely connected to the coast is illustrated by the fact that it is missing at weather station "Skomvaer" situated approximately 50 nmi. off the main coast. A frequency distribution of observed wind speeds along the coast, obtained from Ref. 1, is presented in Table V. A summary of this table follows:

TABLE V

FREQUENCY DISTRIBUTION OF WIND SPEED IN PERCENT PER YEAR
AT WEATHER STATIONS ALONG THE NORWEGIAN COAST

| m/sec | 0-7 | 8-13 | 14-20 | ≥ 21 |
|------------|-----|------|-------|---------------|
| Beaufort | 0-4 | 5+6 | 7+8 | ≥ 9 |
| Ferder | 67 | 28 | 5 | 0.1 |
| Lyngor | 79 | 19 | 2 | 0.2 |
| Lista | 67 | 28 | 5 | 0.2 |
| Utsira | 73 | 22 | 5 | 0.3 |
| Hellisöy | 77 | 19 | 4 | 0.2 |
| Krakenes | 58 | 28 | 11 | 2.7 Jan-Dec |
| Ona | 70 | 22 | 7 | 0.7 1949-1975 |
| Sula | 61 | 30 | 8 | 1.1 |
| Nordoyan | 49 | 35 | 14 | 1.9 |
| Myken | 64 | 26 | 9 | 1.2 |
| Skomvær | 58 | 31 | 10 | 0.9 |
| Andenes | 79 | 18 | 3 | 0.1 |
| Torsvar | 72 | 23 | 5 | 0.4 |
| Fruholmen | 54 | 32 | 12 | 1.8 |
| Vardo | 75 | 22 | 3 | 0.1 |
| Biornoya | 63 | 31 | 6 | 0.4 1956-1975 |
| Polarfront | 46 | 30 | 14 | 1.4 |

The highest winds are reported from the areas between 62°N and 68°N . The frequency of high winds in this area are significantly greater than those found at stations to the south of 62°N and also to the north of 68°N . The wind condition around North Cape, are very severe. This area can be compared with the other coastal area of high wind speed such as "Stadt" (represented by the weather station, "Krakenes"). In these areas the frequency of storms is greater than at "Polarfront" situated in the open Norwegian Sea.

C. WAVES

Frequency distribution of significant wave heights are represented in Table VI.

The station north of 68°N is characterized by comparatively small frequency of high waves. Even at "Furuholmen" where wind conditions are very severe, the frequency distribution of significant wave heights is similar to more sheltered areas like "Utsira."

The seasonal variation for the area of interest around 70°N is given in Figs. 3 and 4. The average monthly distribution of significant wave heights for a typical station like "Andenes" is given in Fig. 3 and Fig. 4 gives the yearly distribution for this station.

TABLE VI

FREQUENCY DISTRIBUTION OF SIGNIFICANT WAVE
HEIGHT IN PERCENT AT THE WEATHER STATION "ANDENES"

STATION: Andenes

YEARS: 1949-1972

| SS | 0+1+2 | 3 | 4 | 5 | 6 | 7 | 8 | 9 | |
|-------|---------|-----------|-----------|-----------|-----------|-----------|------------|------|------|
| H_S | 0 - 0.4 | 0.5 - 1.2 | 1.3 - 2.4 | 2.5 - 3.9 | 4.0 - 5.9 | 6.0 - 8.9 | 9.0 - 13.9 | | N |
| JAN | 15.3 | 26.9 | 33.3 | 15.5 | 6.6 | 2.3 | 0.18 | 0.00 | 2542 |
| FEB | 17.7 | 28.7 | 31.3 | 14.2 | 5.9 | 2.0 | 0.14 | 0.00 | 2295 |
| MAR | 18.1 | 28.9 | 30.8 | 14.3 | 5.8 | 1.9 | 0.17 | 0.00 | 2529 |
| APR | 24.5 | 33.1 | 27.4 | 10.8 | 3.4 | 0.8 | 0.04 | | 2293 |
| MAY | 30.9 | 35.5 | 23.9 | 7.7 | 1.7 | 0.3 | 0.01 | | 1720 |
| JUN | 37.4 | 36.9 | 20.2 | 4.8 | 0.6 | 0.1 | 0.00 | | 1565 |
| JUL | 42.6 | 36.2 | 17.1 | 3.7 | 0.4 | 0.0 | 0.00 | | 1618 |
| AUG | 40.6 | 36.4 | 18.0 | 4.3 | 0.5 | 0.1 | | | 1621 |
| SEP | 29.7 | 34.3 | 24.4 | 8.9 | 2.1 | 0.5 | 0.01 | | 2301 |
| OCT | 21.8 | 31.3 | 29.4 | 12.4 | 4.1 | 1.0 | 0.01 | | 2374 |
| NOV | 21.7 | 31.5 | 29.9 | 11.7 | 4.1 | 1.1 | 0.06 | | 2303 |
| DEC | 18.5 | 30.1 | 32.2 | 13.2 | 4.7 | 1.2 | 0.09 | | 2379 |
| YEAR | 26.6 | 32.5 | 26.5 | 10.1 | 3.3 | 0.9 | 0.06 | 0.00 | |

N = Number of Observations

SS = Class Interval, State of Sea

 H_S = Significant Wave Height

D. AMBIENT NOISE

Due to the fact that the Norwegian Sea is physically separated from the Atlantic by the Faeröy-Shetland-Iceland ridge, and from the Greenland Sea by the Jan Mayan ridge, little long distance shipping noise is transferred into the area. This, combined with relatively low shipping traffic in the central and northern parts of the Norwegian Sea, produces a relatively low ambient noise level for the frequency band $100 < f < 1000$ Hz, especially when noise from marine life is not included. Further, in the absence of nearby shipping and marine life, the ambient noise level in the frequency band $1 < f < 50$ kHz is, according to Ref. 4, dominated by the wind.

A typical area for the central part of the Norwegian Sea can be represented by the weather station "Polarfront" at 66°N , 2°E . Reference 1 shows that there is approximately a 15% chance of finding wind forces of Beaufort > 6 . These effects predict a moderate ambient noise level in the frequency range 100 Hz-50 kHz for the central and northern regions of the Norwegian Sea.

The shallow coastal Norwegian waters are, according to Ref. 4, typically 5-10 dB noisier than the corresponding deep waters. However, great variability caused by local traffic, fishing fleet activity, marine life, and local wind conditions makes ambient noise level prediction

difficult in these areas. This means that accurate ambient noise level determinations have to be made on the spot, as it is both site and time dependent.

A noticeable influence on the ambient noise level is rain, which is a year around feature along the Norwegian coast. As seen from Fig. 8, taken from Ref. 4, rain has a tendency to produce a constant high ambient noise level over a large frequency range, thus dominating other effects. Furthermore, for the upper frequency of interest, i.e., around 60 kHz the lower bound for the ambient noise is determined by the thermal agitation, see Fig. 8.

In determining the figure of merit (FOM) for a passive sonar system, the noise level will be the larger of either the self noise or the ambient noise. For a torpedo the self noise will typically be dominant.

E. SOUND SPEED PROFILES

Again, concentrate on data relevant to Norwegian coastal waters. According to Ref. 6, which covers the southern part of the Norwegian coast, low sound speeds are common because of the influence of water from the Baltic Sea combined with fresh water drainage from the fjords. Furthermore, great variability, both seasonal and within seasons, is encountered. Figure 9 obtained from Ref. 5 gives a picture of the sound speed profiles

for the northern Norwegian coast. Again, large variations are common. Noticeable in both sets of data is a typical seasonal pattern of strong cooling of the surface layer during winter and a similarly strong heating during summer. Furthermore, note that the minimum and maximum are relatively shallow, i.e., less than 50 m.

Also characteristic is the influence of the cold and fresh melt waters drained out through the fjord-arms during spring and summer.

To illustrate the sonar problems associated with these sound speed profiles, ray paths for the extremes of Fig. 9 are shown in Figs. 10 and 11, where the source is 3 m below the sea surface.

APPENDIX B

SURFACE SCATTERING TI 59 PROGRAM

A. INTRODUCTION

This program gives specular scattered power at the receiver versus incoming power at the randomly rough surface in the high frequency limit according to Eq. (70).

Shadowing of surface areas by other parts of the boundary are taken into account by the bistatic shadowing function $S(\theta)$.

Furthermore, the program gives the effect of the randomly rough surface compared to the idealized free-field condition as expressed in Eq. (80). The results of these calculations is given in Fig. 27.

B. PROGRAM STEPS

A block-diagram of the computer program is given in Fig. 26.

The program uses the partitioning ratio of program to data space according to code 4 OP17. The users instructions are as follows:

| Procedure | Enter | Press | Display |
|---|-----------------|-------|---|
| Enter data | Detection range | 2nd A | R_D^1 |
| Enter data | Source depth | R/S | h_s^1 |
| Enter data | Receiver depth | R/S | h_r^1 |
| Enter data | Beam width | R/S | ϕ^1 |
| Enter data | Wind speed | R/S | w^1 |
| Calculate θ , R_1, R_2, A | -- | 2nd B | A $(\theta, R_1, R_2, A)^1$ |
| Calculate $\langle \zeta^{12} \rangle$ | -- | 2nd C | $\langle \zeta^{12} \rangle^1$ |
| Calculate v | -- | 2nd D | v^1 |
| Calculate erfc v | -- | A | erfc v^1 |
| Calculate $S(\theta)$ | -- | B | $S(\theta)^1$ |
| Calculate $\frac{\langle s^2 \rangle}{\langle p_1 p_1^* \rangle}$ | -- | C | $\frac{\langle s^2 \rangle^1}{\langle p_1 p_1^* \rangle^1}$ |
| Calculate ΔIL | -- | D | ΔIL^1 |

¹These values are printed automatically if the calculator is connected to the PC-100A Print Cradle.

For the error function complement we have

$$\text{erfc}(v) = \frac{2}{\sqrt{\pi}} \int_v^{\infty} e^{-\alpha^2} d\alpha$$

in contrast to the normal distribution

$$Q(u) = \frac{1}{\sqrt{2\pi}} \int_u^{\infty} e^{-t^2/2} dt$$

However, there is a linear relationship between the two functions.

The numerical equation used to calculate the $\text{erfc}(v)$ is a modified program from Texas Instruments [Ref. 24].

$$\text{erfc}(v) = Z(v) [b_1\alpha + b_2\alpha^2 + b_3\alpha^3 + b_4\alpha^4 + b_5\alpha^5]$$

where

$$\alpha = \frac{1}{1+\rho v}$$

$$p = .231649$$

$$b_1 = .451673691$$

$$b_2 = -.504257336$$

$$b_3 = 2.51939026$$

$$b_4 = -2.563346623$$

$$b_5 = 1.881292139$$

The program steps are listed below, giving location (LOC), code (COD), key symbol (KEY), and comments.

| | | | | | | | | |
|-----|----|-----|-----|----|-----|-----|----|-----|
| 000 | 76 | LBL | 023 | 17 | B' | 046 | 05 | 05 |
| 001 | 16 | A' | 024 | 53 | (| 047 | 55 | ÷ |
| 002 | 42 | ST | 025 | 53 | (| 048 | 43 | RCL |
| 003 | 00 | 00 | 026 | 43 | RCL | 049 | 02 | 02 |
| 004 | 99 | PRT | 027 | 00 | 00 | 050 | 54 |) |
| 005 | 91 | R/S | 028 | 65 | x | 051 | 22 | INV |
| 006 | 42 | STO | 029 | 43 | RCL | 052 | 30 | TAN |
| 007 | 01 | 01 | 030 | 02 | 02 | 053 | 54 |) |
| 008 | 99 | PRT | 031 | 54 |) | 054 | 42 | STO |
| 009 | 91 | R/S | 032 | 55 | + | 055 | 06 | 06 |
| 010 | 42 | STO | 033 | 53 | (| 056 | 99 | PRT |
| 011 | 02 | 02 | 034 | 43 | RCL | 057 | 53 | (|
| 012 | 99 | PRT | 035 | 01 | 01 | 058 | 53 | (|
| 013 | 91 | R/S | 036 | 85 | + | 059 | 43 | RCL |
| 014 | 42 | STO | 037 | 43 | RCL | 060 | 05 | 05 |
| 015 | 03 | 03 | 038 | 02 | 02 | 061 | 55 | ÷ |
| 016 | 99 | PRT | 039 | 54 |) | 062 | 53 | (|
| 017 | 91 | R/S | 040 | 54 |) | 063 | 43 | RCL |
| 018 | 42 | STO | 041 | 42 | STO | 064 | 06 | 06 |
| 019 | 04 | 04 | 042 | 05 | 05 | 065 | 38 | SIN |
| 020 | 99 | PRT | 043 | 53 | (| 066 | 54 |) |
| 021 | 91 | R/S | 044 | 53 | (| 067 | 54 |) |
| 022 | 76 | LBL | 045 | 43 | RCL | 068 | 42 | STO |

069 07 07
 070 99 PRT
 071 53 (
 072 53 (
 073 43 RCL
 074 00 00
 075 75 -
 076 43 RCL
 077 05 05
 078 54)
 079 55 ÷
 080 53 (
 081 43 RCL
 082 06 06
 083 38 SIN
 084 54)
 085 54)
 086 42 STO
 087 08 08
 088 99 PRT
 089 53 (
 090 43 RCL
 091 07 07
 092 85 +
 093 43 RCL
 094 08 08
 095 54)
 096 42 STO
 097 09 09
 098 25 CLR
 099 69 OP
 100 00 00
 101 01 1
 102 03 3
 103 03 3
 104 05 5
 105 01 1
 106 07 7
 107 01 1
 108 03 3
 109 69 OP
 110 04 04
 111 53 (
 112 53 (
 113 89 π
 114 65 x
 115 43 RCL
 116 08 08
 117 54)
 118 65 x
 119 53 (

120 43 RCL
 121 03 03
 122 38 SIN
 123 65 x
 124 43 RCL
 125 07 07
 126 54)
 127 54)
 128 42 STO
 129 10 10
 130 69 OP
 131 06 06
 132 91 R/S
 133 76 LBL
 134 18 C'
 135 25 CLR
 136 69 OP
 137 00 00
 138 00 00
 139 06 6
 140 02 2
 141 07 7
 142 03 3
 143 02 2
 144 03 3
 145 03 3
 146 69 OP
 147 04 04
 148 53 (
 149 53 (
 150 53 (
 151 43 RCL
 152 04 04
 153 65 x
 154 05 5
 155 93 .
 156 01 1
 157 02 2
 158 54)
 159 85 +
 160 03 3
 161 54)
 162 65 x
 163 93 .
 164 00 0
 165 00 0
 166 01 1
 167 54)
 168 50 1x1
 169 42 STO
 170 11 11

171 69 OP
 172 06 06
 173 91 R/S
 174 76 LBL
 175 19 D'
 176 53 (
 177 43 RCL
 178 06 06
 179 30 TAN
 180 35 1/x
 181 54)
 182 42 STO
 183 12 12
 184 53 (
 185 43 RCL
 186 12 12
 187 55 ÷
 188 53 (
 189 53 (
 190 02 2
 191 65 x
 192 43 RCL
 193 11 11
 194 54)
 195 34 \sqrt{x}
 196 54)
 197 54)
 198 42 STO
 199 13 13
 200 99 PRT
 201 91 R/S
 202 76 LBL
 203 11 A
 204 53 (
 205 53 (
 206 53 (
 207 53 (
 208 43 RCL
 209 13 13
 210 33 x^2
 211 54 (
 212 55 ÷
 213 02 2
 214 54)
 215 94 +/-
 216 22 INV
 217 23 LNX
 218 54)
 219 65 x
 220 53 (
 221 53 (

222 89 π
 223 34 \sqrt{x}
 224 65 x
 225 02 2
 226 54)
 227 35 1/x
 228 54)
 229 54)
 230 42 STO
 231 14 14
 232 53 (
 233 53 (
 234 53 (
 235 53 (
 236 43 RCL
 237 13 13
 238 65 x
 239 93 .
 240 02 2
 241 03 3
 242 01 1
 243 06 6
 244 04 4
 245 01 1
 246 09 9
 247 86 +
 248 01 1
 249 54)
 250 35 1/x
 251 54)
 252 42 STO
 253 15 15
 254 53 (
 255 53 (
 256 43 RCL
 257 14 14
 258 65 x
 259 01 1
 260 93 .
 261 08 8
 262 01 1
 263 54)
 264 65 x
 265 53 (
 266 43 RCL
 267 15 15
 268 65 x
 269 93 .
 270 03 3
 271 .01 1
 272 09 9

273 03 3
 274 08 8
 275 01 1
 276 05 5
 277 03 3
 278 75 -
 279 93 .
 280 03 3
 281 05 5
 282 06 6
 283 05 5
 284 06 6
 285 03 3
 286 07 7
 287 08 8
 288 02 2
 289 65 x
 290 43 RCL
 291 15 15
 292 33 x^2
 293 85 +
 294 01 1
 295 93 .
 296 97 7
 297 08 8
 298 01 1
 299 04 4
 300 07 7
 301 07 7
 302 09 9
 303 03 3
 304 07 7
 305 65 x
 306 43 RCL
 307 15 15
 308 45 Y^X
 309 03 3
 310 75 -
 311 01 1
 312 93 .
 313 08 8
 314 02 2
 315 01 1
 316 02 2
 317 05 5
 318 05 5
 319 09 9
 320 07 7
 321 08 8
 322 00 0
 323 65 x

324 43 RCL
 325 15 15
 326 45 Y^X
 327 04 4
 328 85 +
 329 01 1
 330 93 .
 331 03 3
 332 03 3
 333 00 0
 334 02 2
 335 07 7
 336 04 4
 337 04 4
 338 02 2
 339 09 9
 340 00 0
 341 65 x
 342 43 RCL
 343 15 15
 344 45 Y^X
 345 05 5
 346 54)
 347 54)
 348 42 STO
 349 16 16
 350 99 PRT
 351 91 R/S
 352 76 LBL
 353 12 B
 354 53 (
 355 53 (
 356 53 (
 357 43 RCL
 358 13 13
 359 33 x^2
 360 94 +/-
 361 22 INV
 362 23 LNX
 363 54)
 364 75 -
 365 53 (
 366 89 π
 367 34 \sqrt{x}
 368 65 x
 369 43 RCL
 370 13 13
 371 65 x
 372 43 RCL
 373 16 16
 374 54)

| | | | | | |
|-----|---------------|-----|----------|-----|--------|
| 375 | 54) | 426 | 99 PRT | 477 | 14 D |
| 376 | 55 ÷ | 427 | 91 R/S | 478 | 25 CLR |
| 377 | 53 (| 428 | 76 LBL | 479 | 69 OP |
| 378 | 89 π | 429 | 13 C | 480 | 00 00 |
| 379 | 34 \sqrt{x} | 430 | 25 CLR | 481 | 01 1 |
| 380 | 65 x | 431 | 69 OP | 482 | 06 6 |
| 381 | 04 4 | 432 | 00 00 | 483 | 01 1 |
| 382 | 65 x | 433 | 03 3 | 484 | 04 4 |
| 383 | 43 RCL | 434 | 06 6 | 485 | 69 OP |
| 384 | 13 13 | 435 | 01 1 | 486 | 04 04 |
| 385 | 54) | 436 | 05 5 | 487 | 53 (|
| 386 | 54) | 437 | 01 1 | 488 | 53 (|
| 387 | 42 STO | 438 | 03 3 | 489 | 43 RCL |
| 388 | 17 17 | 439 | 03 3 | 490 | 19 19 |
| 389 | 53 (| 440 | 07 7 | 491 | 28 LOG |
| 390 | 53 (| 441 | 69 OP | 492 | 54) |
| 391 | 53 (| 442 | 04 04 | 493 | 65 x |
| 392 | 01 1 | 443 | 53 (| 494 | 01 1 |
| 393 | 75 - | 444 | 53 (| 495 | 00 0 |
| 394 | 53 (| 445 | 43 RCL | 496 | 54) |
| 395 | 53 (| 446 | 10 10 | 497 | 42 STO |
| 396 | 53 (| 447 | 65 x | 498 | 20 20 |
| 397 | 43 RCL | 448 | 43 RCL | 499 | 69 OP |
| 398 | 17 17 | 449 | 18 18 | 500 | 06 06 |
| 399 | 65 x | 450 | 54) | 501 | 91 R/S |
| 400 | 04 4 | 451 | 55 ÷ | | |
| 401 | 54) | 452 | 53 (| | |
| 402 | 94 +/- | 453 | 53 (| | |
| 403 | 54) | 454 | 53 (| | |
| 404 | 22 INV | 455 | 53 (| | |
| 405 | 23 LNX | 456 | 43 RCL | | |
| 406 | 54) | 457 | 07 07 | | |
| 407 | 54) | 458 | 33 x^2 | | |
| 408 | 65 x | 459 | 54) | | |
| 409 | 53 (| 460 | 65 x | | |
| 410 | 01 1 | 461 | 08 8 | | |
| 411 | 75 - | 462 | 54) | | |
| 412 | 43 RCL | 463 | 65 x | | |
| 413 | 16 16 | 464 | 89 π | | |
| 414 | 54) | 465 | 54) | | |
| 415 | 54) | 466 | 65 x | | |
| 416 | 55 ÷ | 467 | 43 RCL | | |
| 417 | 53 (| 468 | 11 11 | | |
| 418 | 43 RCL | 469 | 54) | | |
| 419 | 17 17 | 470 | 54) | | |
| 420 | 65 x | 471 | 42 STO | | |
| 421 | 04 4 | 472 | 19 19 | | |
| 422 | 54) | 473 | 69 OP | | |
| 423 | 54) | 474 | 06 06 | | |
| 424 | 42 STO | 475 | 91 R/S | | |
| 425 | 18 18 | 476 | 76 LBL | | |

APPENDIX C

BUBBLE DYNAMICS TI 59 PROGRAM

A. INTRODUCTION

This program gives the resonant frequency f_r and the damping constant δ for bubbles according to Eq. (92). Furthermore, the program gives scattering cross section σ_s , extinction cross section σ_e , and absorption cross section σ_a as a function of bubble radius a , incoming frequency f , and depth z . The results of the calculations are given in Figs. 31 and 32.

B. PROGRAM STEPS

The user's instructions are as follows:

| Procedure | Enter | Press | Display |
|--|--------------------|-------|------------------------------|
| Enter data | Bubble Radius | 2nd A | a^1 |
| Enter data | Incoming Frequency | R/S | f^1 |
| Enter data | Depth | R/S | z^1 |
| Calculate X | -- | 2nd B | X^1 |
| Calculate coshX and sinhX | -- | 2nd C | $\cosh X^1$ $\sinh X^1$ |
| Calculate d/b | -- | 2nd D | d/b^1 |
| Calculate b | -- | 2nd E | b^1 |
| Calculate β | -- | A | β^1 |
| Calculate f_r | -- | B | f_r^1 |
| Calculate δ | -- | C | δ^1 |
| Calculate σ | -- | D | σ_e^1 |
| Calculate σ_s and σ_a | -- | E | σ_s^1 σ_a^1 |

¹These values are printed automatically if the calculator is connected to PC-100A Print Cradle.

The program steps are listed below giving location (LOC), code (COD), key (KEY) and comments.

| | | | | | | | | |
|-----|----|-----|-----|----|-----|-----|----|-----|
| 000 | 76 | LBL | 043 | 55 | ÷ | 086 | 01 | 01 |
| 001 | 16 | A' | 044 | 43 | RCL | 087 | 99 | PRT |
| 002 | 42 | STO | 045 | 11 | 11 | 088 | 91 | R/S |
| 003 | 11 | 11 | 046 | 54 |) | 089 | 76 | LBL |
| 004 | 99 | PRT | 047 | 85 | + | 090 | 18 | C' |
| 005 | 91 | R/S | 048 | 93 | . | 091 | 53 | (|
| 006 | 42 | STO | 049 | 00 | 0 | 092 | 53 | (|
| 007 | 12 | 12 | 050 | 00 | 0 | 093 | 43 | RCL |
| 008 | 99 | PRT | 051 | 01 | 1 | 094 | 01 | 01 |
| 009 | 91 | R/S | 052 | 02 | 2 | 095 | 22 | INV |
| 010 | 42 | STO | 053 | 09 | 9 | 096 | 23 | LNx |
| 011 | 13 | 13 | 054 | 65 | x | 097 | 85 | + |
| 012 | 99 | PRT | 055 | 53 | (| 098 | 43 | RCL |
| 013 | 91 | R/S | 056 | 01 | 1 | 099 | 01 | 01 |
| 014 | 76 | LBL | 057 | 85 | + | 100 | 94 | X/- |
| 015 | 17 | B' | 058 | 93 | . | 101 | 22 | INV |
| 016 | 53 | (| 059 | 01 | 1 | 102 | 23 | LNx |
| 017 | 53 | (| 060 | 65 | x | 103 | 54 |) |
| 018 | 53 | (| 061 | 43 | RCL | 104 | 55 | ÷ |
| 019 | 53 | (| 062 | 13 | 13 | 105 | 02 | 2 |
| 020 | 53 | (| 063 | 54 |) | 106 | 54 |) |
| 021 | 53 | (| 064 | 54 |) | 107 | 42 | STO |
| 022 | 04 | 4 | 065 | 54 |) | 108 | 02 | 02 |
| 023 | 65 | x | 066 | 65 | x | 109 | 99 | PRT |
| 024 | 89 | π | 067 | 93 | . | 110 | 53 | (|
| 025 | 54 |) | 068 | 02 | 2 | 111 | 53 | (|
| 026 | 65 | x | 069 | 04 | 4 | 112 | 43 | RCL |
| 027 | 43 | RCL | 070 | 54 |) | 113 | 01 | 01 |
| 028 | 12 | 12 | 071 | 55 | ÷ | 114 | 22 | INV |
| 029 | 54 |) | 072 | 93 | . | 115 | 23 | LNx |
| 030 | 65 | x | 073 | 00 | 0 | 116 | 75 | - |
| 031 | 53 | (| 074 | 00 | 0 | 117 | 43 | RCL |
| 032 | 53 | (| 075 | 00 | 0 | 118 | 01 | 01 |
| 033 | 93 | . | 076 | 00 | 0 | 119 | 94 | +/- |
| 034 | 00 | 0 | 077 | 05 | 5 | 120 | 22 | INV |
| 035 | 00 | 0 | 078 | 06 | 6 | 121 | 23 | LNx |
| 036 | 00 | 0 | 079 | 54 |) | 122 | 54 |) |
| 037 | 00 | 0 | 080 | 34 | √x | 123 | 55 | ÷ |
| 038 | 00 | 0 | 081 | 65 | x | 124 | 02 | 2 |
| 039 | 00 | 0 | 082 | 43 | RCL | 125 | 54 |) |
| 040 | 01 | 0 | 083 | 11 | 11 | 126 | 42 | STO |
| 041 | 09 | 9 | 084 | 54 |) | 127 | 03 | 03 |
| 042 | 01 | 1 | 085 | 42 | STO | 128 | 99 | PRT |

| | | | | | | | | |
|-----|----|----------------|-----|----|-----|-----|----|----------------|
| 129 | 91 | R/S | 180 | 53 | (| 231 | 54 |) |
| 130 | 76 | LBL | 181 | 01 | 1 | 232 | 54 |) |
| 131 | 17 | D' | 182 | 93 | . | 233 | 55 | ÷ |
| 132 | 53 | (| 183 | 02 | 2 | 234 | 53 | (|
| 133 | 53 | (| 184 | 65 | x | 235 | 43 | RCL |
| 134 | 53 | (| 185 | 43 | RCL | 236 | 02 | 02 |
| 135 | 53 | (| 186 | 01 | 01 | 237 | 75 | - |
| 136 | 43 | RCL | 187 | 54 |) | 238 | 43 | RCL |
| 137 | 01 | 01 | 188 | 65 | x | 239 | 01 | 01 |
| 138 | 65 | x | 189 | 53 | (| 240 | 39 | COS |
| 139 | 53 | (| 190 | 43 | RCL | 241 | 54 |) |
| 140 | 43 | RCL | 191 | 03 | 03 | 242 | 54 |) |
| 141 | 03 | 03 | 192 | 75 | - | 243 | 85 | + |
| 142 | 85 | + | 193 | 43 | RCL | 244 | 01 | 1 |
| 143 | 43 | RCL | 194 | 01 | 01 | 245 | 54 |) |
| 144 | 01 | 01 | 195 | 38 | SIN | 246 | 35 | 1/x |
| 145 | 38 | SIN | 196 | 54 |) | 247 | 65 | x |
| 146 | 54 |) | 197 | 54 |) | 248 | 53 | (|
| 147 | 54 |) | 198 | 54 |) | 249 | 54 | (|
| 148 | 75 | - | 199 | 54 |) | 250 | 43 | RCL |
| 149 | 02 | 2 | 200 | 65 | x | 251 | 04 | 04 |
| 150 | 65 | x | 201 | 01 | 1 | 252 | 33 | x ² |
| 151 | 53 | (| 202 | 93 | . | 253 | 54 |) |
| 152 | 43 | RCL | 203 | 02 | 2 | 254 | 85 | + |
| 153 | 02 | 02 | 204 | 54 |) | 255 | 01 | 1 |
| 154 | 75 | - | 205 | 42 | STO | 256 | 54 |) |
| 155 | 43 | RCL | 206 | 04 | 04 | 257 | 35 | 1/x |
| 156 | 01 | 01 | 207 | 99 | PRT | 258 | 54 |) |
| 157 | 39 | COS | 208 | 91 | R/S | 259 | 42 | STO |
| 158 | 54 |) | 209 | 76 | LBL | 260 | 05 | 05 |
| 159 | 54 |) | 210 | 10 | E | 261 | 99 | PRT |
| 160 | 55 | ÷ | 211 | 53 | (| 262 | 91 | R/S |
| 161 | 53 | (| 212 | 53 | (| 263 | 76 | LBL |
| 162 | 53 | (| 213 | 53 | (| 264 | 11 | A |
| 163 | 53 | (| 214 | 53 | (| 265 | 53 | (|
| 164 | 43 | RCL | 215 | 53 | (| 266 | 53 | (|
| 165 | 01 | 01 | 216 | 03 | 3 | 267 | 53 | (|
| 166 | 33 | x ² | 217 | 93 | . | 268 | 01 | 1 |
| 167 | 54 |) | 218 | 02 | 2 | 269 | 05 | 5 |
| 168 | 65 | x | 219 | 55 | ÷ | 270 | 00 | 0 |
| 169 | 53 | (| 220 | 43 | RCL | 271 | 55 | ÷ |
| 170 | 43 | RCL | 221 | 01 | 01 | 272 | 53 | (|
| 171 | 02 | 02 | 222 | 54 |) | 273 | 01 | 1 |
| 172 | 75 | - | 223 | 65 | x | 274 | 00 | 0 |
| 173 | 43 | RCL | 224 | 53 | (| 275 | 01 | 1 |
| 174 | 01 | 01 | 225 | 43 | RCL | 276 | 03 | 3 |
| 175 | 39 | COS | 226 | 03 | 03 | 277 | 00 | 0 |
| 176 | 54 |) | 227 | 75 | - | 278 | 00 | 0 |
| 177 | 54 |) | 228 | 43 | RCL | 279 | 00 | 0 |
| 178 | 85 | + | 229 | 01 | 01 | 280 | 65 | x |
| 179 | 53 | (| 230 | 38 | SIN | 281 | 43 | RCL |

282 11 11
 283 65 x
 284 53 (
 285 01 1
 286 85 +
 287 93 .
 288 01 1
 289 65 x
 290 43 RCL
 291 13 13
 292 54)
 293 54)
 294 54)
 295 65 x
 296 53)
 297 01 1
 298 75 -
 299 53 (
 300 53 (
 301 04 4
 302 93 .
 303 02 2
 304 65 x
 305 43 RCL
 306 05 05
 307 54)
 308 35 1/x
 309 54)
 310 54)
 311 54)
 312 85 +
 313 01 1
 314 54)
 315 42 STO
 316 06 06
 317 99 PRT
 318 91 R/S
 319 76 LBL
 320 12 B
 321 53 (
 322 53 (
 323 53 (
 324 53 (
 325 04 4
 326 93 .
 327 02 2
 328 65 x
 329 43 RCL
 330 05 05
 331 65 x
 332 43 RCL

333 06 06
 334 65 x
 335 01 1
 336 00 0
 337 01 1
 338 03 3
 339 00 0
 340 00 0
 341 00 0
 342 54)
 343 65 x
 344 53 (
 345 01 1
 346 85 +
 347 93 .
 348 01 1
 349 65 x
 350 43 RCL
 351 13 13
 352 52)
 353 54)
 354 55 ÷
 355 01 1
 356 93 .
 357 00 0
 358 02 2
 359 06 6
 360 54)
 361 50 1x1
 362 34 \sqrt{x}
 363 65 x
 364 53 (
 365 53 (
 366 89 π
 367 65 x
 368 02 2
 369 65 x
 370 43 RCL
 371 11 11
 372 54)
 373 35 1/x
 374 54)
 375 54)
 376 42 STO
 377 07 07
 378 99 PRT
 379 91 R/S
 380 76 LBL
 381 13 C
 382 53 (
 383 53 (

384 53 (
 385 93 .
 386 00 0
 387 00 0
 388 00 0
 389 00 0
 390 04 4
 391 01 1
 392 08 8
 393 08 8
 394 07 7
 395 09 9
 396 65 x
 397 43 RCL
 398 12 12
 399 65 x
 400 43 RCL
 401 11 11
 402 54)
 403 85 +
 404 53 (
 405 43 RCL
 406 04 04
 407 65 x
 408 53 (
 409 53 (
 410 43 RCL
 411 07 07
 412 55 ÷
 413 43 RCL
 414 12 12
 415 54)
 416 33 x^2
 417 54)
 418 54)
 419 54)
 420 85 +
 421 53 (
 422 93 =
 423 00 0
 424 00 0
 425 06 6
 426 02 2
 427 00 0
 428 05 5
 429 55 ÷
 430 53 (
 431 43 RCL
 432 12 12
 433 65 x
 434 53 (

435 43 RCL
 436 11 11
 437 33 x^2
 438 54)
 439 54)
 440 54)
 441 54)
 442 42 STO
 443 08 08
 444 99 PRT
 445 91 R/S
 446 76 LBL
 447 14 D
 448 53 (
 449 53 (
 450 04 4
 451 65 x
 452 89 π
 453 65 x
 454 43 RCL
 455 11 11
 456 54)
 457 65 x
 458 53 (
 459 53 (
 460 43 RCL
 461 08 08
 462 65 x
 463 01 1
 464 05 5
 465 00 0
 466 00 0
 467 00 0
 468 00 0
 469 55 \div
 470 53 (
 471 89 π
 472 65 x
 473 02 2
 474 65 x
 475 43 RCL
 476 12 12
 477 54)
 478 54)
 479 54)
 480 55 \div
 481 53 (
 482 53 (
 483 53 (
 484 53 (
 485 53 (

486 43 RCL
 487 07 07
 488 55 \div
 489 43 RCL
 490 12 12
 491 54)
 492 33 x^2
 493 54)
 494 75 -
 495 01 1
 496 54)
 497 33 x^2
 498 54)
 499 85 +
 500 53 (
 501 43 RCL
 502 08 08
 503 33 x^2
 504 54)
 505 54)
 506 54)
 507 42 STO
 508 09 09
 509 99 PRT
 510 91 R/S
 511 76 LBL
 512 15 E
 513 53 (
 514 53 (
 515 04 4
 516 65 x
 517 89 π
 518 65 x
 519 53 (
 520 43 RCL
 521 11 11
 522 33 x^2
 523 54)
 524 54)
 525 55 \div
 526 53 (
 527 53 (
 528 53 (
 529 53 (
 530 53 (
 531 43 RCL
 532 07 07
 533 55 \div
 534 43 RCL
 535 12 12
 536 54)

537 33 x^2
 538 54)
 539 75 -
 540 01 1
 541 54)
 542 33 x^2
 543 53)
 544 85 +
 545 53 (
 546 43 RCL
 547 08 08
 548 33 x^2
 549 54)
 550 54)
 551 54)
 552 42 STO
 553 10 10
 554 99 PRT
 555 66 PAU
 556 53 (
 557 43 RCL
 558 09 09
 559 75 -
 560 43 RCL
 561 10 10
 562 54)
 563 42 STO
 564 11 11
 565 99 PRT
 566 91 R/S

APPENDIX D

NUMERICAL INTEGRATION TI 59 PROGRAM

A. INTRODUCTION

In order to perform the numerical integration of $\sigma n(a)da$, a standard Texas Instrument's program was used [Ref. 25]. This program performs the integration by using Simpson's discrete approximation based on the following expression

$$I = \int_{x_0}^{x_n} f(x) dx \approx \frac{h}{3} (f_0 + 4f_1 + 2f_2 + 4f_3 + 2f_4 + \dots + 2f_{n-2} + 4f_{n-1} + f_n)$$

where

$f(x)$ must be known at $n+1$ equally spaced points $(f_0 - f_n)$.

$$h = \frac{x_n - x_0}{n} ; x_n > x_0$$

$n+7 \leq$ number of data registers available

n = number of subintervals = 2, 4, 6,

B. PROGRAM INSTRUCTIONS

The program is taken from the master library program package by using the code 2nd Pgm 10 on the calculator.

The user's instructions are as follows

| Procedure | Enter | Press | Display |
|------------|-----------------|-------|---------|
| Enter data | Subintervals | A | n^1 |
| Enter data | h | B | h^1 |
| Enter data | Function values | | |
| | 0 | C | 0 |
| | f_0 | R/S | f_0^1 |
| | f_1 | R/S | f_1^1 |
| | . | . | |
| | . | . | |
| | f_n | R/S | f_n^1 |
| Calculate | - | D | I^1 |

¹These values are printed automatically if the calculator is connected to PC-100A Print Cradle.

The program steps are listed below giving location (LOC), key symbol (KEY), and comments.

| | | | | | | | | |
|-----|----|-----|-----|----|------------|-----|----|------------|
| 000 | 76 | LBL | 019 | 99 | PRT | 038 | 06 | 6 |
| 001 | 11 | A | 020 | 92 | RTN | 039 | 54 |) |
| 002 | 53 | (| 021 | 76 | LBL | 040 | 42 | STO |
| 003 | 50 | 1x1 | 022 | 52 | EE | 041 | 01 | 01 |
| 004 | 42 | STO | 023 | 00 | 0 | 042 | 32 | $x \leq t$ |
| 005 | 05 | 05 | 024 | 35 | 1/x | 043 | 98 | ADV |
| 006 | 55 | ÷ | 025 | 92 | RTN | 044 | 92 | RTN |
| 007 | 02 | 2 | 026 | 76 | LBL | 045 | 76 | LBL |
| 008 | 54 |) | 027 | 12 | B | 046 | 50 | 1x1 |
| 009 | 42 | STO | 028 | 42 | STO | 047 | 76 | ST* |
| 010 | 02 | 02 | 029 | 03 | 03 | 048 | 01 | 01 |
| 011 | 22 | INV | 030 | 99 | PRT | 049 | 32 | $x \geq t$ |
| 012 | 59 | INT | 031 | 92 | RTN | 050 | 01 | 1 |
| 013 | 29 | CP | 032 | 76 | LBL | 051 | 44 | SUM |
| 014 | 22 | INV | 033 | 13 | C | 052 | 01 | 01 |
| 015 | 67 | EQ | 034 | 53 | (| 053 | 32 | $x \leq t$ |
| 016 | 52 | EE | 035 | 24 | CE | 054 | 99 | PRT |
| 017 | 43 | RCL | 036 | 85 | + | 055 | 92 | RTN |
| 018 | 05 | 05 | 037 | 32 | $x \leq t$ | 056 | 61 | GTO |

| | | | | | |
|-----|----|----------------|-----|----|-----|
| 057 | 50 | 1x1 | 108 | 44 | SUM |
| 058 | 76 | LBL | 109 | 04 | 04 |
| 059 | 14 | D | 110 | 53 | (|
| 060 | 53 | (| 111 | 43 | RCL |
| 061 | 43 | RCL | 112 | 03 | 03 |
| 062 | 05 | 05 | 113 | 55 | ÷ |
| 063 | 85 | + | 114 | 03 | 3 |
| 064 | 06 | 6 | 115 | 54 |) |
| 065 | 54 |) | 116 | 49 | PRD |
| 066 | 42 | STO | 117 | 04 | 04 |
| 067 | 01 | 01 | 118 | 43 | RCL |
| 068 | 73 | RC* | 119 | 04 | 04 |
| 069 | 01 | 01 | 120 | 98 | ADV |
| 070 | 42 | STO | 121 | 99 | PRT |
| 071 | 04 | 04 | 122 | 92 | RTN |
| 072 | 76 | LBL | | | |
| 073 | 45 | y ^x | | | |
| 074 | 01 | 1 | | | |
| 075 | 22 | INV | | | |
| 076 | 44 | SUM | | | |
| 077 | 01 | 01 | | | |
| 078 | 53 | (| | | |
| 079 | 73 | RC* | | | |
| 080 | 01 | 01 | | | |
| 081 | 65 | x | | | |
| 082 | 04 | 4 | | | |
| 083 | 54 |) | | | |
| 084 | 44 | SUM | | | |
| 085 | 04 | 04 | | | |
| 086 | 01 | 1 | | | |
| 087 | 22 | INV | | | |
| 088 | 44 | SUM | | | |
| 089 | 01 | 01 | | | |
| 090 | 22 | INV | | | |
| 091 | 97 | DSZ | | | |
| 092 | 02 | 02 | | | |
| 093 | 33 | x ² | | | |
| 094 | 53 | (| | | |
| 095 | 73 | RC* | | | |
| 096 | 01 | 01 | | | |
| 097 | 65 | x | | | |
| 098 | 02 | 2 | | | |
| 099 | 54 |) | | | |
| 100 | 44 | SUM | | | |
| 101 | 04 | 04 | | | |
| 102 | 61 | GTO | | | |
| 103 | 45 | y ^x | | | |
| 104 | 76 | LBL | | | |
| 105 | 33 | x ² | | | |
| 106 | 73 | RC* | | | |
| 107 | 01 | 01 | | | |

APPENDIX E

TURN RATE LIMITATION TI 59 PROGRAMS

A. INTRODUCTION

The turn rate limitation calculations are divided into two parts with separate programs.

B. PART I PROGRAM

For a given initial detection range and a given ship speed, Part I performs a sequential calculation of $\phi_A, K_A, \phi_B, K_B, \phi^*$ and K^* for each of the maximum turn rates investigated, together with the "no limit" conditions $(V_s)_{NL}$ and K_{NL} based on

$$\phi_A = \sin^{-1} \left(\frac{3p|\dot{\phi}|_{\max}}{V_s} \right); \leq 90^\circ$$

$$\phi_B = 180^\circ - \phi_A$$

$$K_{A,B} = \frac{V_s (1 + \cos \phi_{A,B})^P}{|\dot{\phi}|_{\max} (\sin \phi_{A,B})^{P-2}}$$

$$\phi^* = \cos^{-1} (P-2)$$

$$K^* = \frac{V_s (1+P/2)^P [1-(P/2)^2]^{1-P/2}}{|\dot{\phi}|_{\max}}$$

$$(V_s)_{NL} = (3V_T |\dot{\phi}|_{\max})^{1/2}$$

$$K_{NL} = 3p$$

For $p > 2$, the solution for $*$ and K^* are not valid.
Furthermore, for V_s (V_s)_{NL} no solutions are valid for any of the quantities.

The program is based on the fixed torpedo speed of $V_T = 35$ kts (18 m/s) and an initial detection range of $T_O = R_D = 250$ m.

The user instructions for the program are as follows:

| Prodcedure | Enter | Press | Display |
|------------------------------------|-------------------|-------|--------------------|
| Enter data | Maximum Turn Rate | A | $ \phi _{\max}^1$ |
| Enter data | Ship speed | B | V_T^1 |
| Calculate ϕ^* and K^* | -- | C | ϕ^*, K^{*1} |
| Calculate ϕ_A and ϕ_B | -- | D | ϕ_A, ϕ_B^1 |
| Calculate K_A and K_B | -- | E | K_A, K_B^1 |

¹These values are printed automatically if the calculator is connected to PC-100A Print Cradle.

A listing of the program steps follows giving location (LOC), code (COD), key symbol (KEY), and comments.

| | | |
|------------|------------|------------|
| 000 76 LBL | 012 69 OP | 024 54) |
| 001 11 A | 013 00 00 | 025 42 STO |
| 002 42 STO | 014 03 3 | 026 03 03 |
| 003 01 01 | 015 03 3 | 027 69 OP |
| 004 99 PRT | 016 69 OP | 028 06 06 |
| 005 91 R/S | 017 04 04 | 029 25 CLR |
| 006 76 LBL | 018 53 (| 030 69 OP |
| 007 12 B | 019 01 1 | 031 00 00 |
| 008 42 STO | 020 08 8 | 032 02 2 |
| 009 02 02 | 021 55 ÷ | 033 06 6 |
| 010 99 PRT | 022 43 RCL | 034 03 3 |
| 011 25 CLR | 023 02 02 | 035 01 1 |

036 02 2
 037 07 7
 038 69 OP
 039 04 04
 040 53 (
 041 43 RCL
 042 03 03
 043 65 x
 044 03 3
 045 54)
 046 42 STO
 047 10 10
 048 69 OP
 049 06 06
 050 25 CLR
 051 69 OP
 052 00 00
 053 04 4
 054 02 2
 055 03 3
 056 06 6
 057 03 3
 058 01 1
 059 02 2
 060 07 7
 061 69 OP
 062 04 04
 063 53 (
 064 53 (
 065 53 (
 066 03 3
 067 65 x
 068 01 1
 069 08 8
 070 54)
 071 65 x
 072 43 RCL
 073 01 01
 074 54)
 075 34 \sqrt{x}
 076 54)
 077 42 STO
 078 11 11
 079 69 OP
 080 06 06
 081 91 R/S
 082 76 LBL
 083 13 C
 084 25 CLR
 085 69 OP
 086 00 00

087 03 3
 088 03 3
 089 02 2
 090 03 3
 091 05 5
 092 01 1
 093 69 OP
 094 04 04
 095 53 (
 096 53 (
 097 53 (
 098 43 RCL
 099 03 03
 100 55 \div
 101 02 2
 102 54)
 103 22 INV
 104 39 COS
 105 54)
 106 54)
 107 42 STO
 108 04 04
 109 69 OP
 110 06 06
 111 25 CLR
 112 69 OP
 113 00 00
 114 02 2
 115 06 6
 116 05 5
 117 01 1
 118 69 OP
 119 04 04
 120 53 (
 121 53 (
 122 53 (
 123 53 (
 124 43 RCL
 125 02 02
 126 65 x
 127 53 (
 128 53 (
 129 01 1
 130 85 +
 131 53 (
 132 43 RCL
 133 03 03
 134 55 \div
 135 02 2
 136 54)
 137 54)

138 45 y^x
 139 43 RCL
 140 03 03
 141 54)
 142 54)
 143 65 x
 144 53 (
 145 53 (
 146 01 1
 147 75 -
 148 53 (
 149 53 (
 150 43 RCL
 151 03 03
 152 55 \div
 153 02 2
 154 54)
 155 33 x^2
 156 54)
 157 54)
 158 45 y^x
 159 53 (
 160 01 1
 161 75 -
 162 53 (
 163 43 RCL
 164 03 03
 165 55 \div
 166 02 2
 167 54)
 168 54)
 169 54)
 170 54)
 171 55 \div
 172 43 RCL
 173 01 01
 174 54)
 175 42 STO
 176 05 05
 177 69 OP
 178 06 06
 179 91 R/S
 180 76 LBL
 181 14 D
 182 25 CLR
 183 69 OP
 184 00 00
 185 03 3
 186 03 3
 187 02 2
 188 03 3

189 01 1
 190 03 3
 191 69 OP
 192 04 04
 193 53 (
 194 53 (
 195 53 (
 196 53 (
 197 53 (
 198 43 RCL
 199 03 03
 200 65 x
 201 03 3
 202 54)
 203 65 x
 204 43 RCL
 205 01 01
 206 54)
 207 55 ÷
 208 43 RCL
 209 02 02
 210 54)
 211 22 INV
 212 38 SIN
 213 54)
 214 42 STO
 215 06 06
 216 69 OP
 217 06 06
 218 25 CLR
 219 69 OP
 220 00 00
 221 03 3
 222 03 3
 223 02 2
 224 03 3
 225 01 1
 226 04 4
 227 69 OP
 228 04 04
 229 53 (
 230 01 1
 231 08 8
 232 00 0
 233 75 -
 234 43 RCL
 235 06 06
 236 54)
 237 42 STO
 238 07 07
 239 69 OP

240 06 06
 241 91 R/S
 242 76 LBL
 243 15 E
 244 25 CLR
 245 69 OP
 246 00 00
 247 02 2
 248 06 6
 249 01 1
 250 03 3
 251 69 OP
 252 04 04
 253 53 (
 254 53 (
 255 43 RCL
 256 02 02
 257 65 x
 258 53 (
 259 53 (
 260 01 1
 261 85 +
 262 53 (
 263 43 RCL
 264 06 06
 265 39 COS
 266 54)
 267 54)
 268 45 y^x
 269 43 RCL
 270 03 03
 271 54)
 272 54)
 273 55 ÷
 274 53 (
 275 43 RCL
 276 01 01
 277 65 x
 278 53 (
 279 53 (
 280 43 RCL
 281 06 06
 282 38 SIN
 283 54)
 284 45 y^x
 285 53 (
 286 43 RCL
 287 03 03
 288 75 -
 289 02 2
 290 54)

291 54)
 292 54)
 293 54)
 294 42 STO
 295 08 08
 296 69 OP
 297 06 06
 298 25 CLR
 299 69 OP
 300 00 00
 301 02 2
 302 06 6
 303 01 1
 304 04 4
 305 69 OP
 306 04 04
 307 53 (
 308 53 (
 309 43 RCL
 310 02 02
 311 65 x
 312 53 (
 313 53 (
 314 01 1
 315 85 +
 316 53 (
 317 43 RCL
 318 07 07
 319 39 COS
 320 54)
 321 54)
 322 45 y^x
 323 43 RCL
 324 03 03
 325 54)
 326 54)
 327 55 ÷
 328 53 (
 329 43 RCL
 330 01 01
 331 65 x
 332 53 (
 333 53 (
 334 43 RCL
 335 07 07
 336 38 SIN
 337 54)
 338 45 y^x
 339 53 (
 340 43 RCL
 341 03 03

```

342 75 -
343 02 2
344 54 )
345 54 )
346 54 )
347 54 )
348 42 STO
349 09 09
350 69 OP
351 06 06
352 91 R/S
353 02 2
354 54 )
355 54 )
356 54 )
357 54 )
358 42 STO
359 09 09
360 69 OP
361 06 06
362 91 R/S

```

C. PART II PROGRAM

Given K from Part I, Part II program performs the probe calculations of the corresponding initial approach angles $(\phi_O)_A$, $(\phi_O)_B$, $(\phi_O)^*$, and $(\phi_O)_{NL}$ based on the relationship

$$f(\phi_O) = K_{A,B,*,NL} [\sin(\phi_O)_{A,B,*,NL}]^{P-1} \\ -r_O [(1+(\cos\phi_O)_{A,B,*,NL})^P] = 0$$

The program used a fixed torpedo speed of $V_T = 35$ kts (18 m/s) and an initial detection range of $r_O = R_D = 250$ m. The purpose of this general probe program is to locate roots of the given function $y = f(\phi_O)$ to evaluate the slope of the tangent line, and to find the maximum and minimum points on a graph. We will only use the first feature.

The program requires a subroutine for the function to be investigated. This subroutine starts at program location 140 and is located at label 2nd C. The user's instructions for the program are as follows:

| Procedure | Enter | Press | Display |
|---|-------------------------------|-------|----------------------------|
| Enter data | Starting Value of ϕ_0 | 2nd D | ϕ_0 |
| Enter data | The increment $\Delta\phi_0$ | 2nd E | $\Delta\phi_0$ |
| Calculate $f(\phi_0 + \Delta\phi_0)$ | -- | A | $f(\phi_0 + \Delta\phi_0)$ |
| Calculate $f(\phi_0 - \Delta\phi_0)$ | -- | B | $f(\phi_0 - \Delta\phi_0)$ |
| Display current value of ϕ_0 | -- | E | ϕ_0 |

If the value of $\Delta\phi_0$ is chosen too large, $\Delta\phi_0$ may be replaced by $\Delta\phi_0/10$ by pressing label 2nd A. Similarly, if a larger value of $\Delta\phi_0$ is required, $\Delta\phi_0$ can be replaced by $10\Delta\phi_0$ by pressing label 2nd B. A listing of the program steps follows, giving location (LOC), code (COD), key symbol (KEY), and comments.

Associated with the subroutine, it should be noted that the value of K, r_0 and p are entered separately in the memory locations 10, 11, and 12, respectively.

| | | | | | | | | |
|-----|----|-----|-----|----|-----|-----|----|-----|
| 000 | 76 | LBL | 051 | 42 | STO | 102 | 75 | - |
| 001 | 19 | D' | 052 | 03 | 03 | 103 | 43 | RCL |
| 002 | 42 | STO | 053 | 53 | (| 104 | 04 | 04 |
| 003 | 01 | 01 | 054 | 43 | RCL | 105 | 54 |) |
| 004 | 91 | R/S | 055 | 01 | 01 | 106 | 55 | ÷ |
| 005 | 76 | LBL | 056 | 75 | - | 107 | 43 | RCL |
| 006 | 10 | E' | 057 | 43 | RCL | 108 | 02 | 02 |
| 007 | 42 | STO | 058 | 02 | 02 | 109 | 54 |) |
| 008 | 02 | 02 | 059 | 55 | ÷ | 110 | 91 | R/S |
| 009 | 91 | R/S | 060 | 02 | 2 | 111 | 76 | LBL |
| 010 | 76 | LBL | 061 | 54 |) | 112 | 15 | E |
| 011 | 11 | A | 062 | 71 | SBR | 113 | 43 | RCL |
| 012 | 53 | (| 063 | 18 | C' | 114 | 01 | 01 |
| 013 | 43 | RCL | 064 | 42 | STO | 115 | 91 | R/S |
| 014 | 01 | 01 | 065 | 04 | 04 | 116 | 76 | LBL |
| 015 | 85 | + | 066 | 53 | (| 117 | 16 | A' |
| 016 | 43 | RCL | 067 | 53 | (| 118 | 53 | (|
| 017 | 02 | 02 | 068 | 43 | RCL | 119 | 43 | RCL |
| 018 | 54 |) | 069 | 03 | 03 | 120 | 02 | 02 |
| 019 | 42 | STO | 070 | 75 | - | 121 | 55 | ÷ |
| 020 | 01 | 01 | 071 | 43 | RCL | 122 | 01 | 1 |
| 021 | 71 | SBR | 072 | 04 | 04 | 123 | 00 | 0 |
| 022 | 18 | C' | 073 | 54 |) | 124 | 54 |) |
| 023 | 91 | R/S | 074 | 55 | ÷ | 125 | 42 | STO |
| 024 | 76 | LBL | 075 | 43 | RCL | 126 | 02 | 02 |
| 025 | 12 | B | 076 | 02 | 02 | 127 | 91 | R/S |
| 026 | 53 | (| 077 | 54 |) | 128 | 76 | LBL |
| 027 | 43 | RCL | 078 | 91 | R/S | 129 | 17 | B' |
| 028 | 01 | 01 | 079 | 76 | LBL | 130 | 53 | (|
| 029 | 75 | - | 080 | 14 | D | 131 | 43 | RCL |
| 030 | 43 | RCL | 081 | 53 | (| 132 | 02 | 02 |
| 031 | 02 | 02 | 082 | 43 | RCL | 133 | 65 | x |
| 032 | 54 |) | 083 | 01 | 01 | 134 | 01 | 1 |
| 033 | 42 | STO | 084 | 85 | + | 135 | 00 | 0 |
| 034 | 01 | 01 | 085 | 43 | RCL | 136 | 54 |) |
| 035 | 71 | SBR | 086 | 02 | 02 | 137 | 42 | STO |
| 036 | 18 | C' | 087 | 54 |) | 138 | 02 | 02 |
| 037 | 91 | R/S | 088 | 71 | SBR | 139 | 91 | R/S |
| 038 | 76 | LBL | 089 | 18 | C' | 140 | 76 | LBL |
| 039 | 13 | C | 090 | 42 | STO | 141 | 18 | C' |
| 040 | 53 | (| 091 | 03 | 03 | 142 | 42 | STO |
| 041 | 43 | RCL | 092 | 43 | RCL | 143 | 00 | 00 |
| 042 | 01 | 01 | 093 | 01 | 01 | 144 | 70 | RAD |
| 043 | 85 | + | 094 | 71 | SBR | 145 | 53 | (|
| 044 | 43 | RCL | 095 | 18 | C' | 146 | 53 | (|
| 045 | 02 | 02 | 096 | 42 | STO | 147 | 43 | RCL |
| 046 | 55 | ÷ | 097 | 04 | 04 | 148 | 10 | 10 |
| 047 | 02 | 2 | 098 | 53 | (| 149 | 65 | x |
| 048 | 54 |) | 099 | 53 | (| 150 | 53 | (|
| 049 | 71 | SBR | 100 | 43 | RCL | 151 | 53 | (|
| 050 | 18 | C' | 101 | 43 | RCL | 152 | 43 | RCL |

153 00 00
154 38 SIN
155 54)
156 45 y^x
157 43 RCL
158 13 13
159 54)
160 54)
161 75 -
162 53 (
163 43 RCL
164 11 11
165 65 x
166 53 (
167 53 (
168 01 1
169 85 +
170 53 (
171 43 RCL
172 00 00
173 39 COS
174 54)
175 54)
176 45 y^x
177 43 RCL
178 12 12
179 54)
180 54)
181 54)
182 92 RTN

APPENDIX F
FIGURES

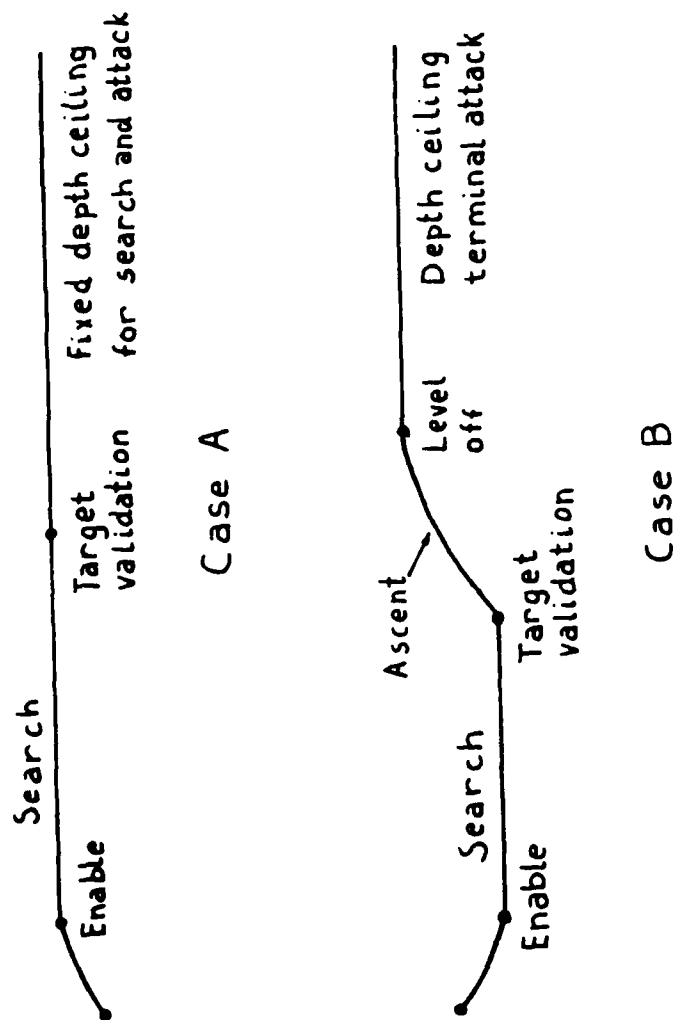


Fig. 1. Torpedo Search and Attack Geometry.

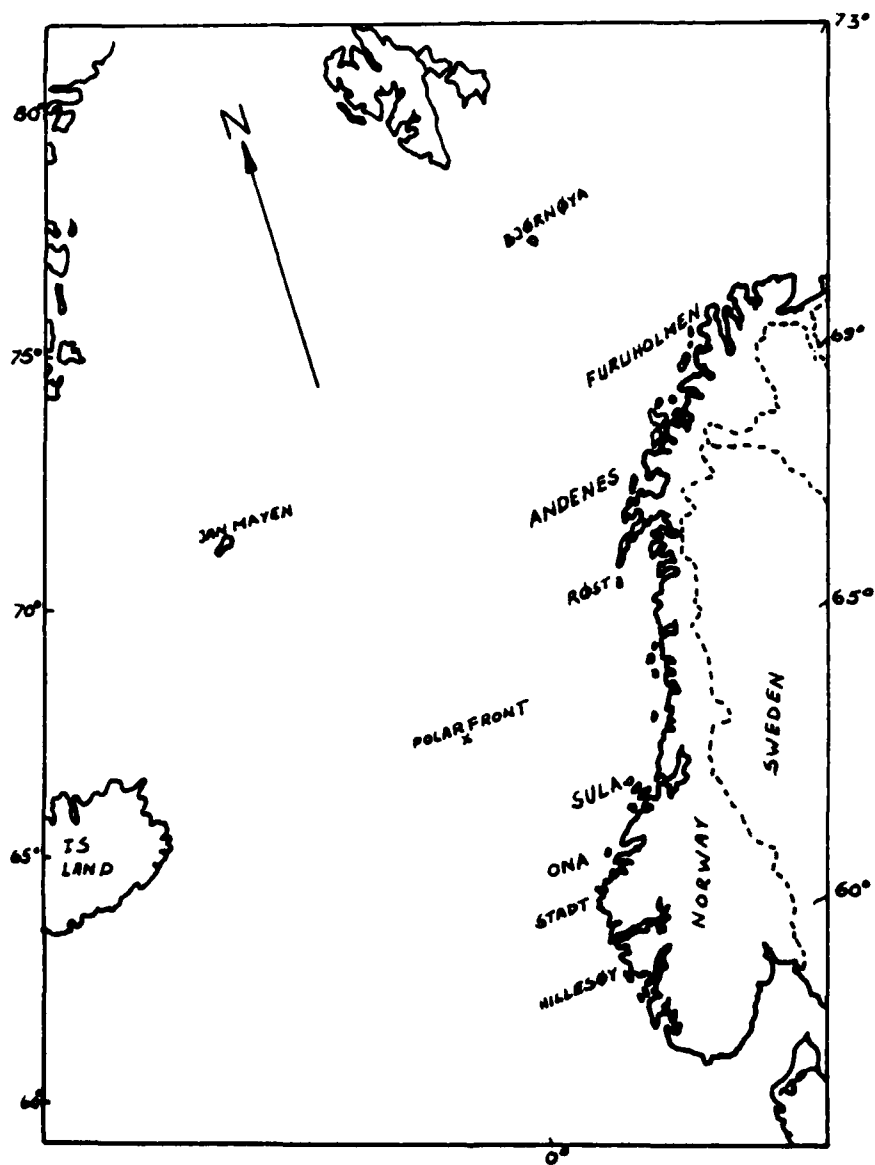


Fig. 2. Location of Weather Stations Along the Norwegian Coast.

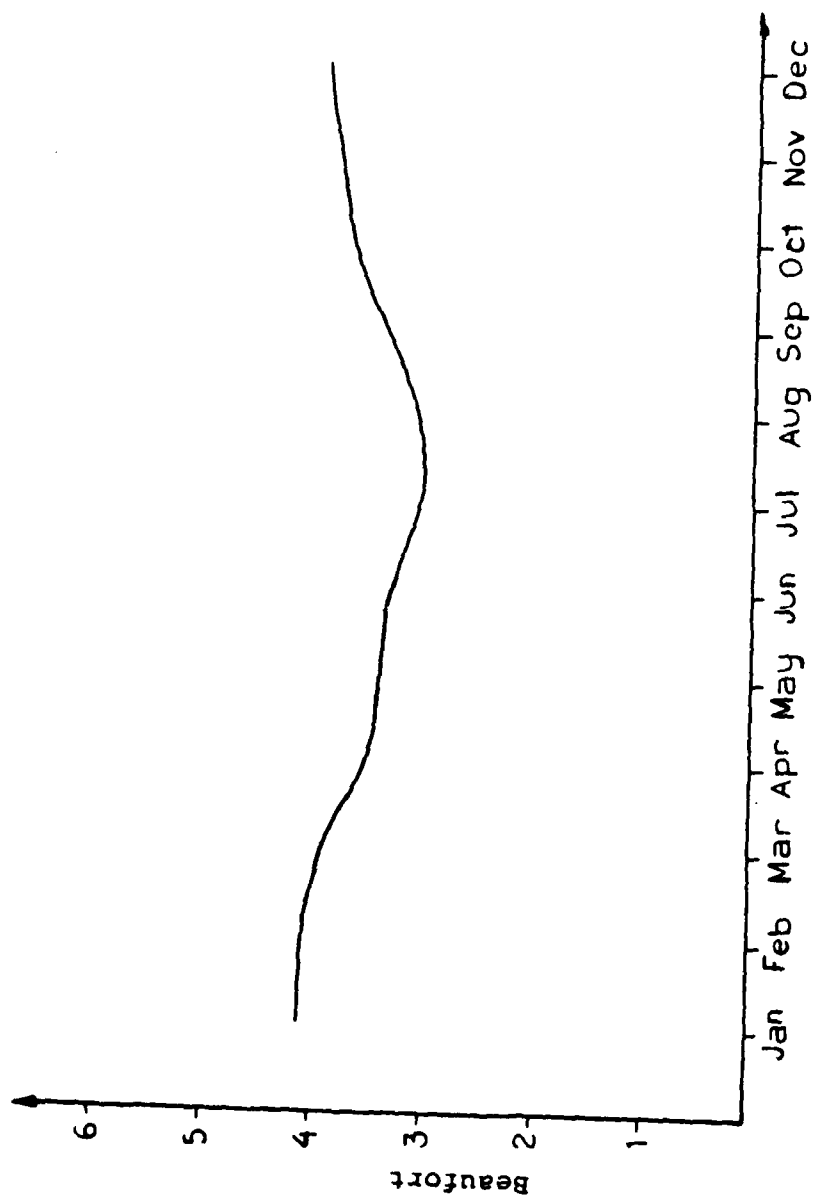


Fig. 3. Average Monthly Wind Speed in Beaufort from the Weather Station "Andenes."

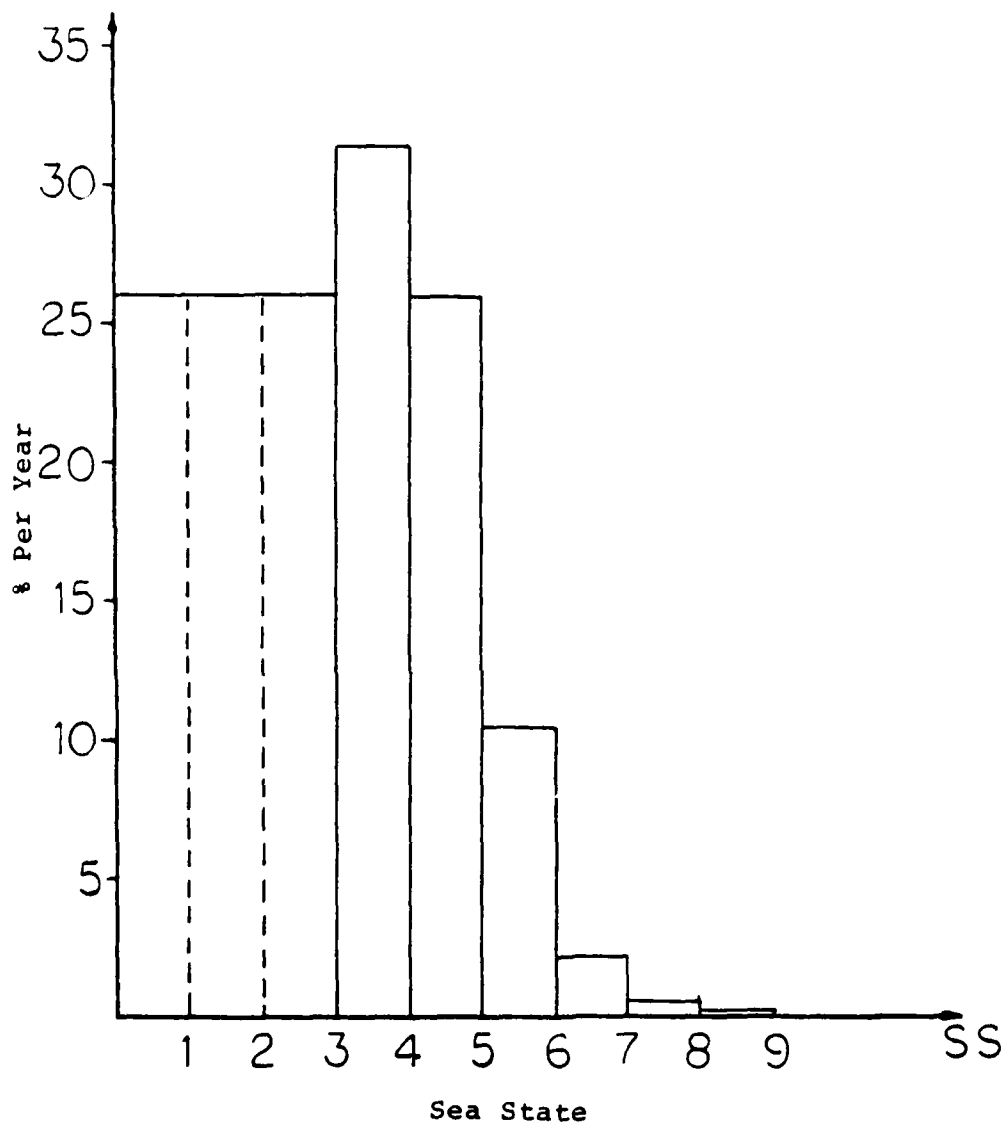


Fig. 4. Histogram of Significant Wave in Percent per Year from the Weather Station "Andenes."

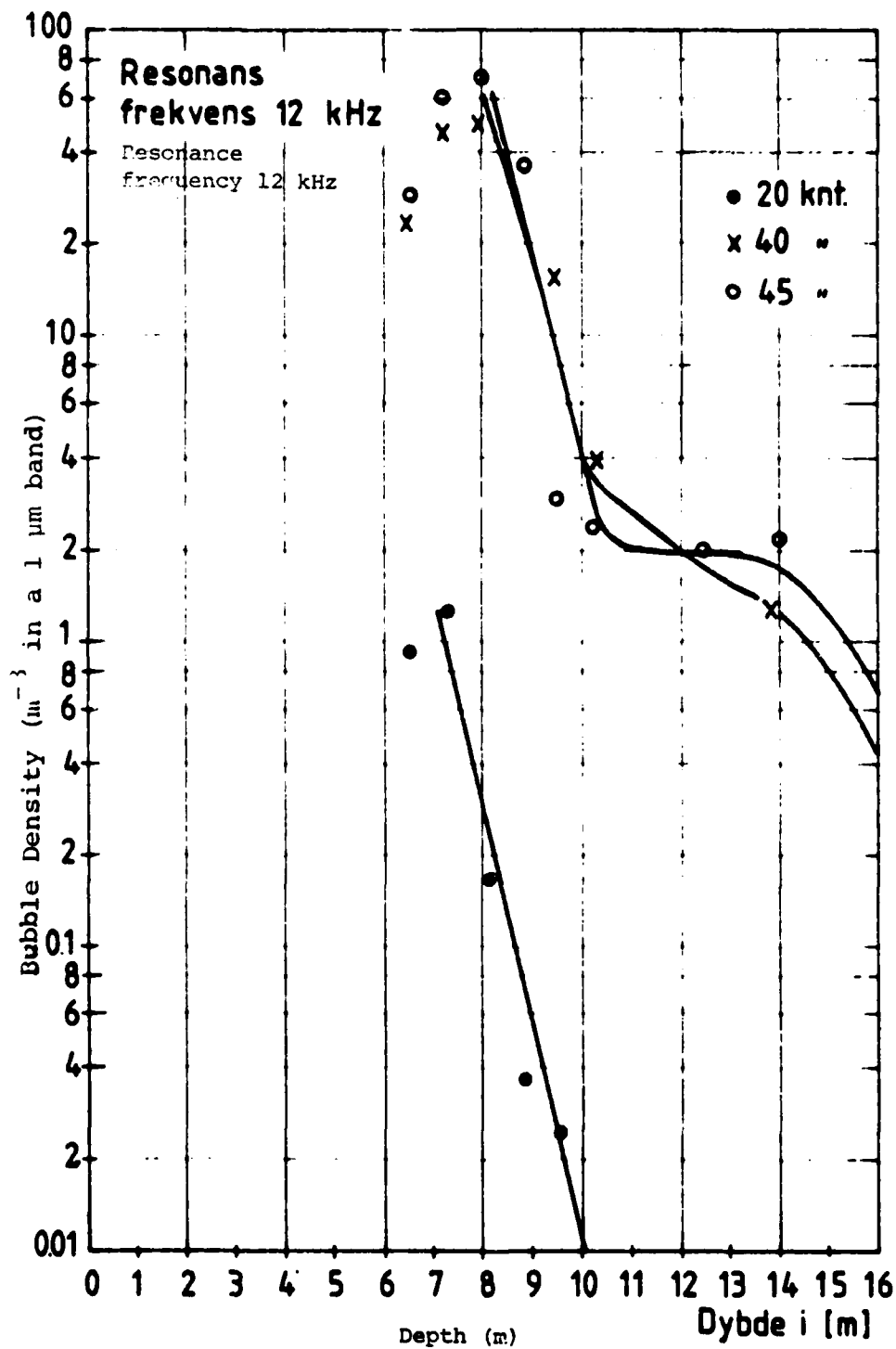


Fig. 5. Resonant Bubble Density at 12 kHz as a Function of Depth.

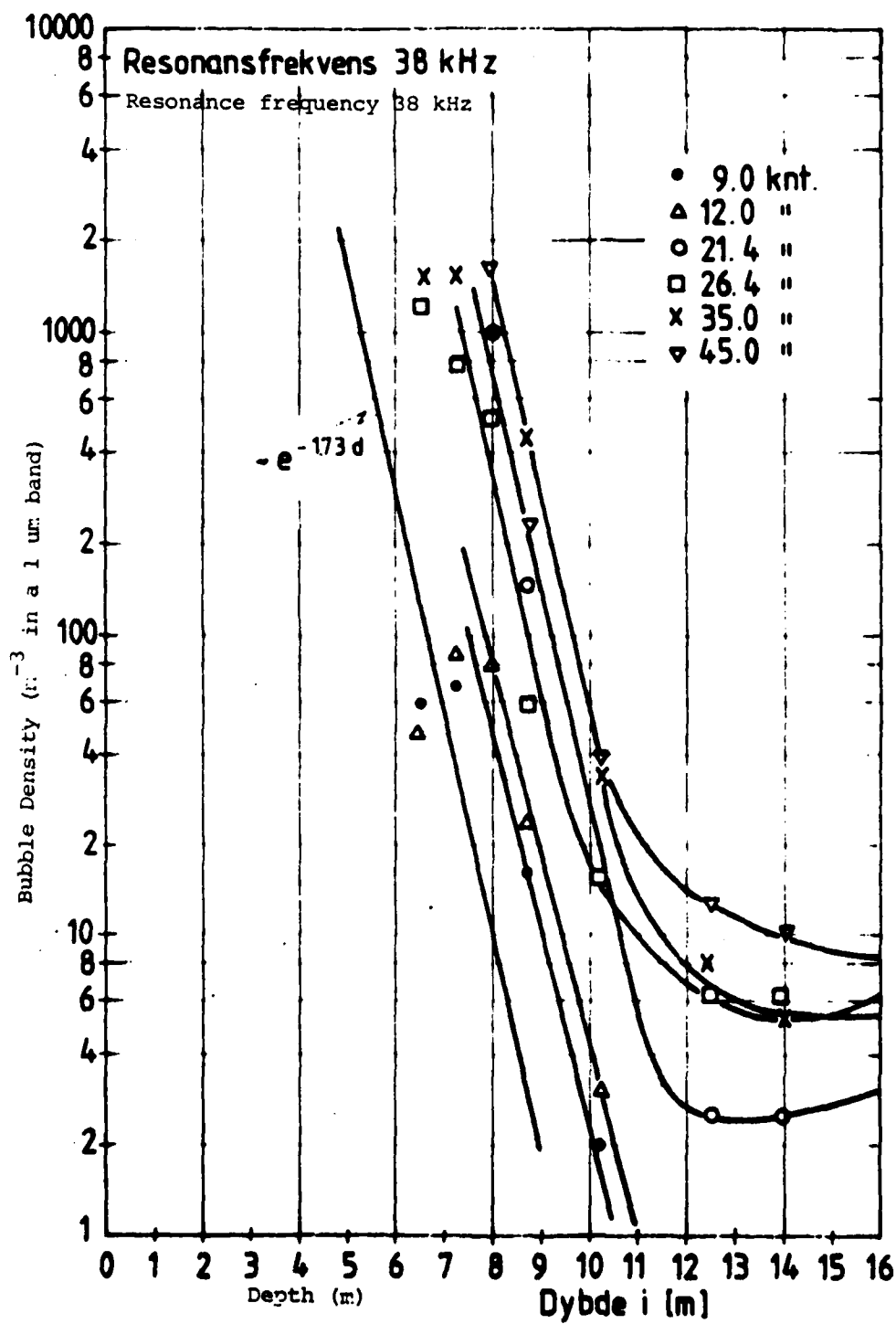


Fig. 6. Resonant Bubble Density at 38 kHz as a Function of Depth.

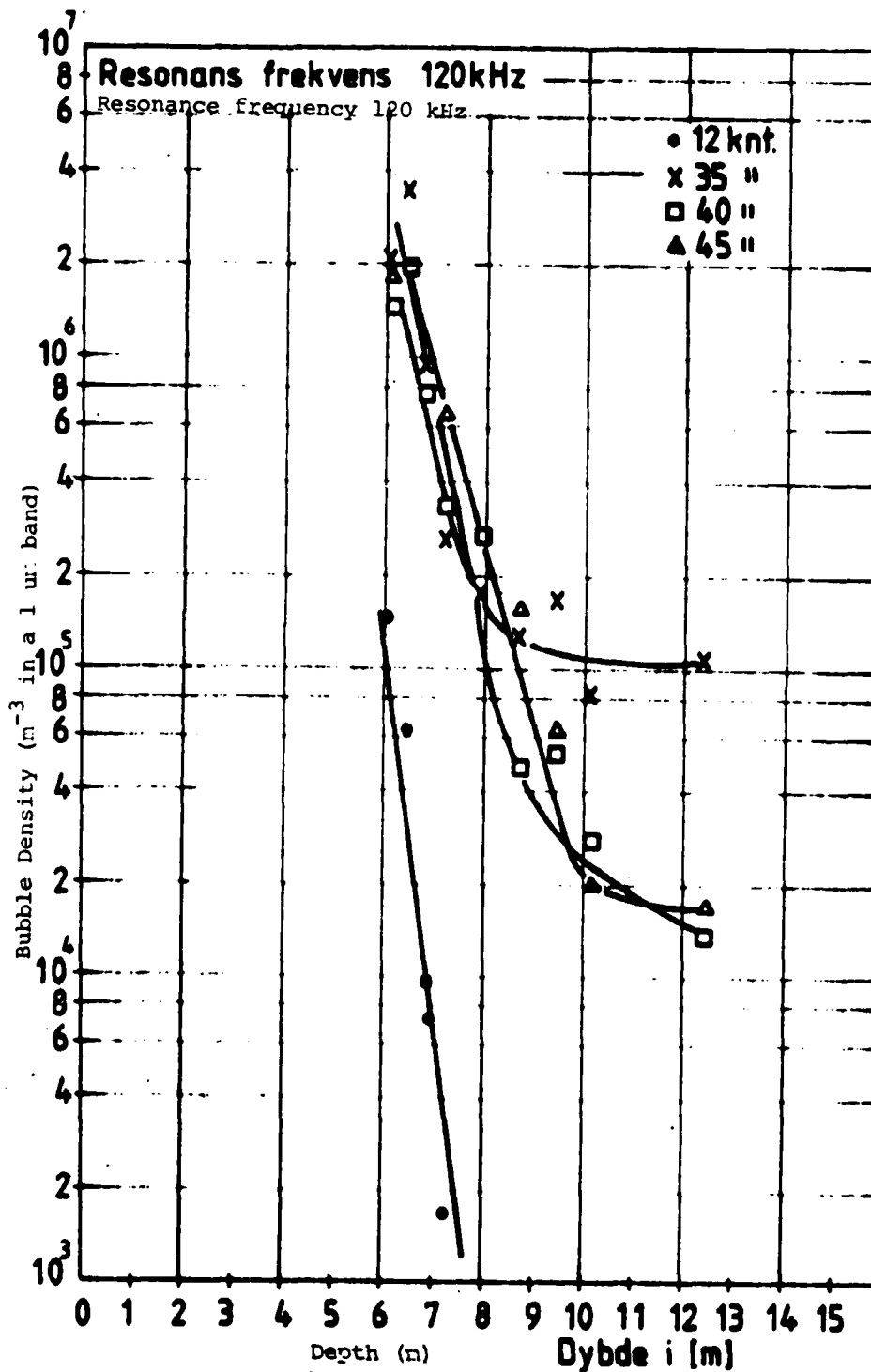


Fig. 7. Resonant Bubble Density at 120 kHz as a Function of Depth.

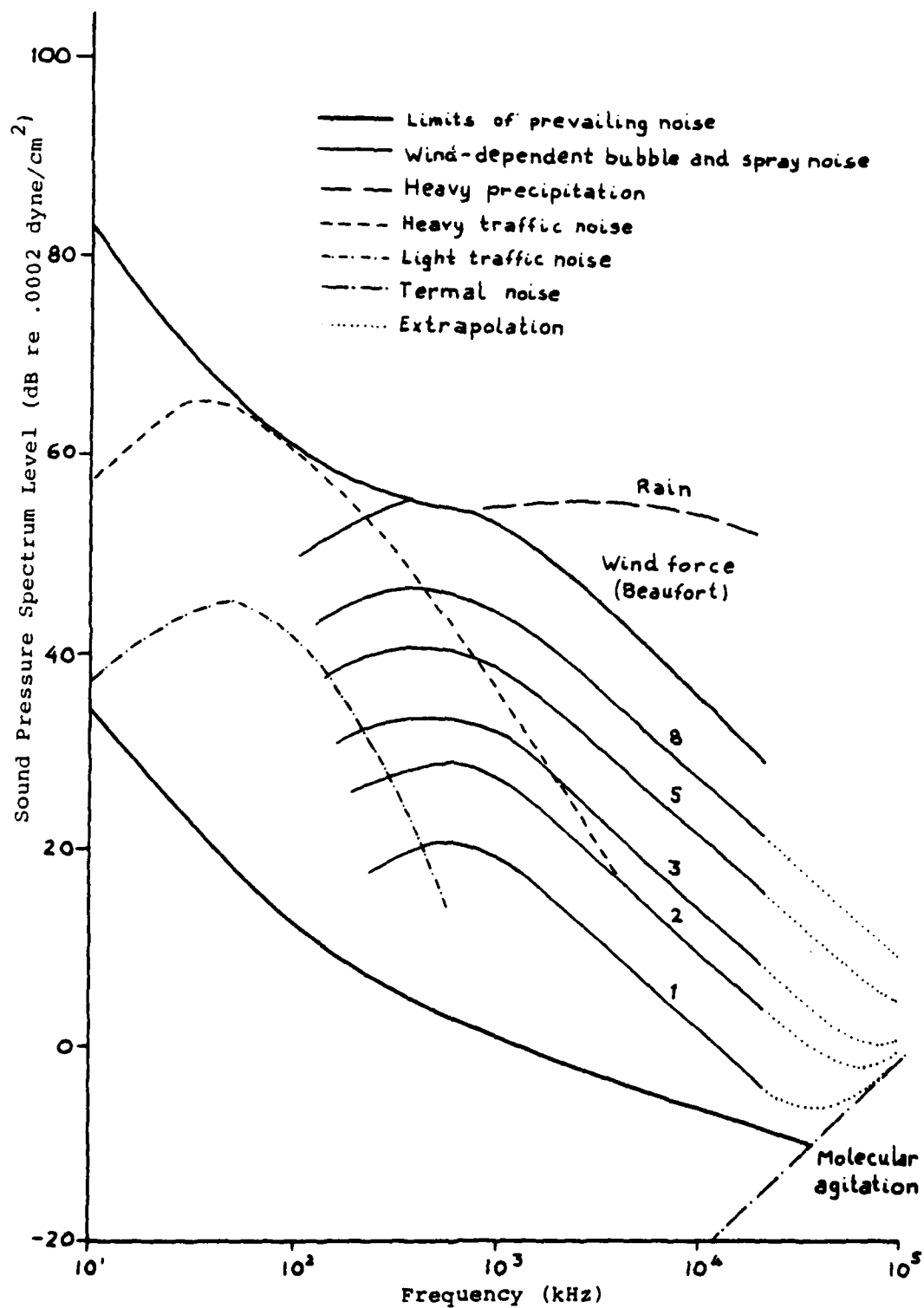


Fig. 8. Ambient Noise Level Curves.

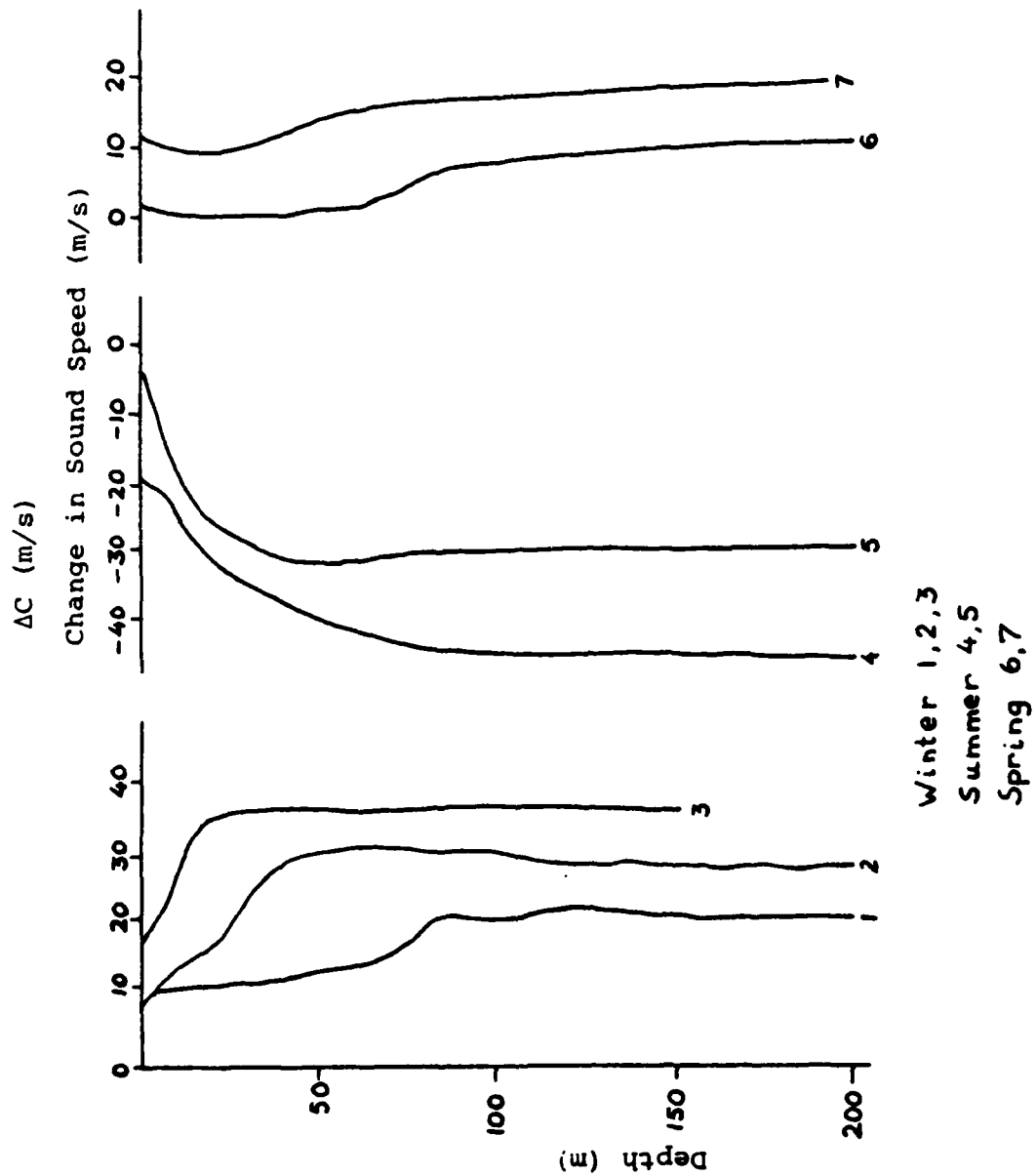
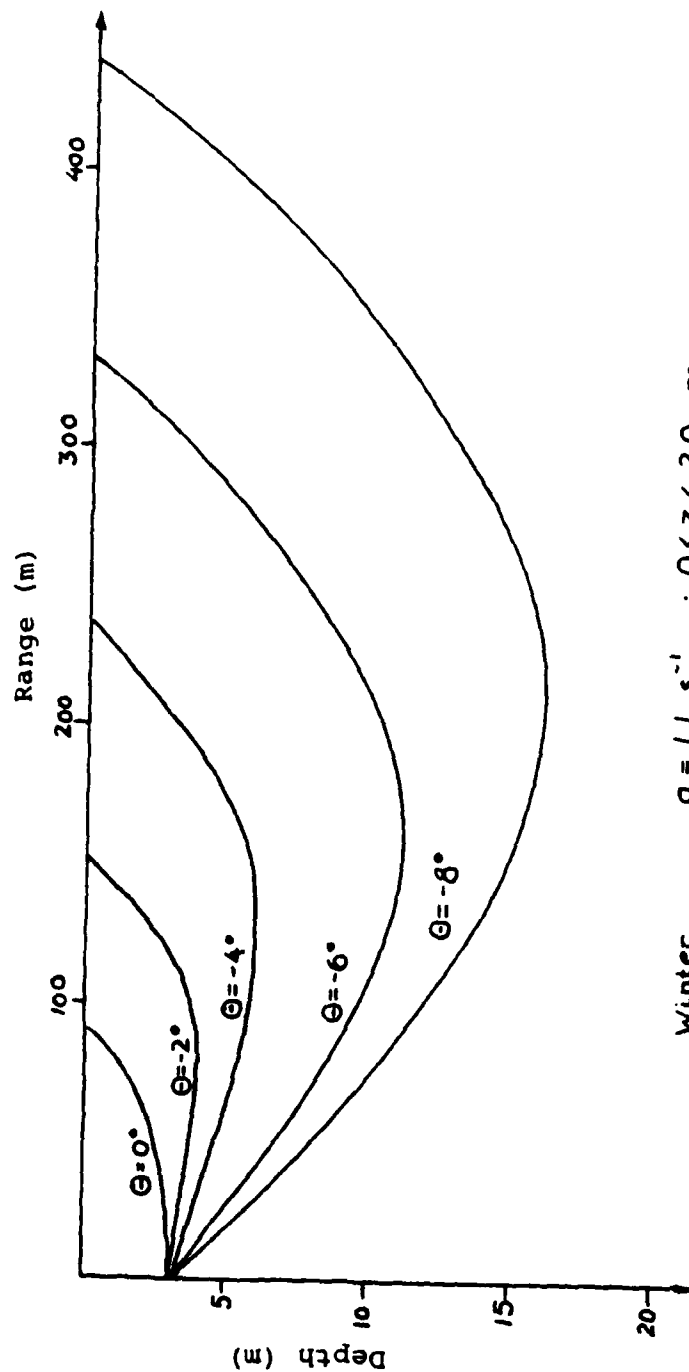
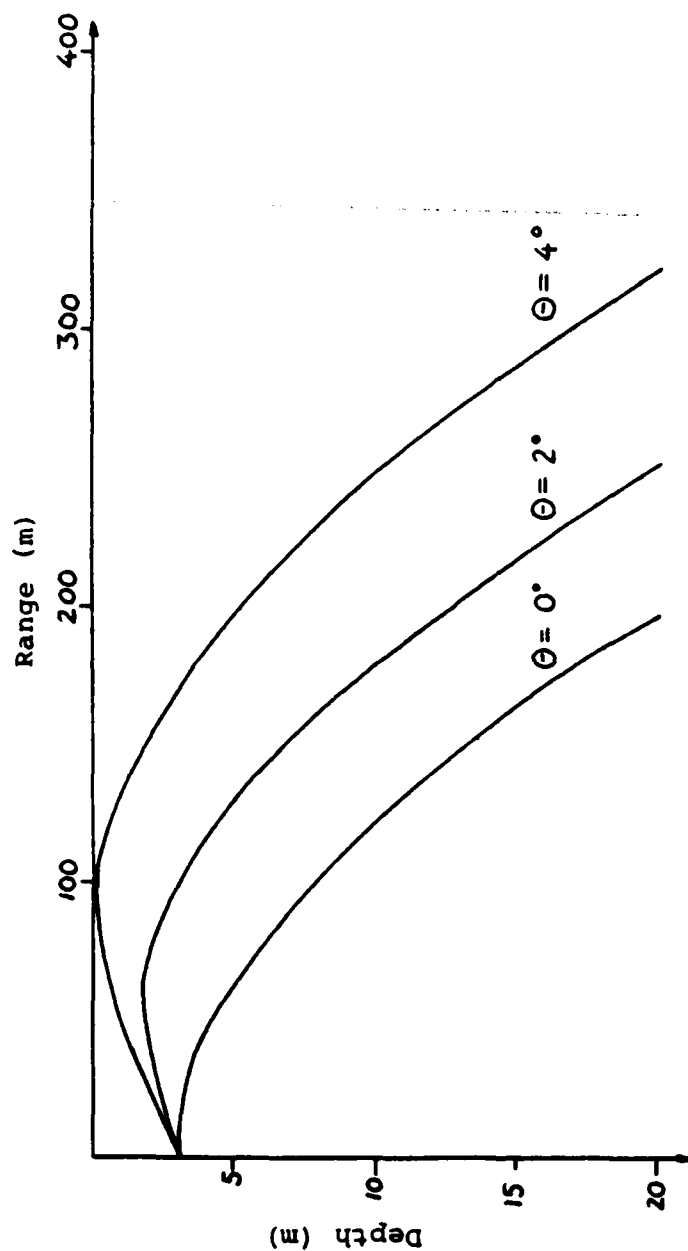


Fig. 9. Typical Sound Speed Profiles in Norwegian Coastal Waters.



Winter , $g = 1.1 \text{ s}^{-1}$; $0 < z < 20 \text{ m}$

Fig. 10. Worst Case Ray Path During Winter.



Summer, $g = 1.25 \text{ s}^{-1}$; $0 < z < 20 \text{ m}$

Fig. 11. Worst Case Ray Path During Summer.

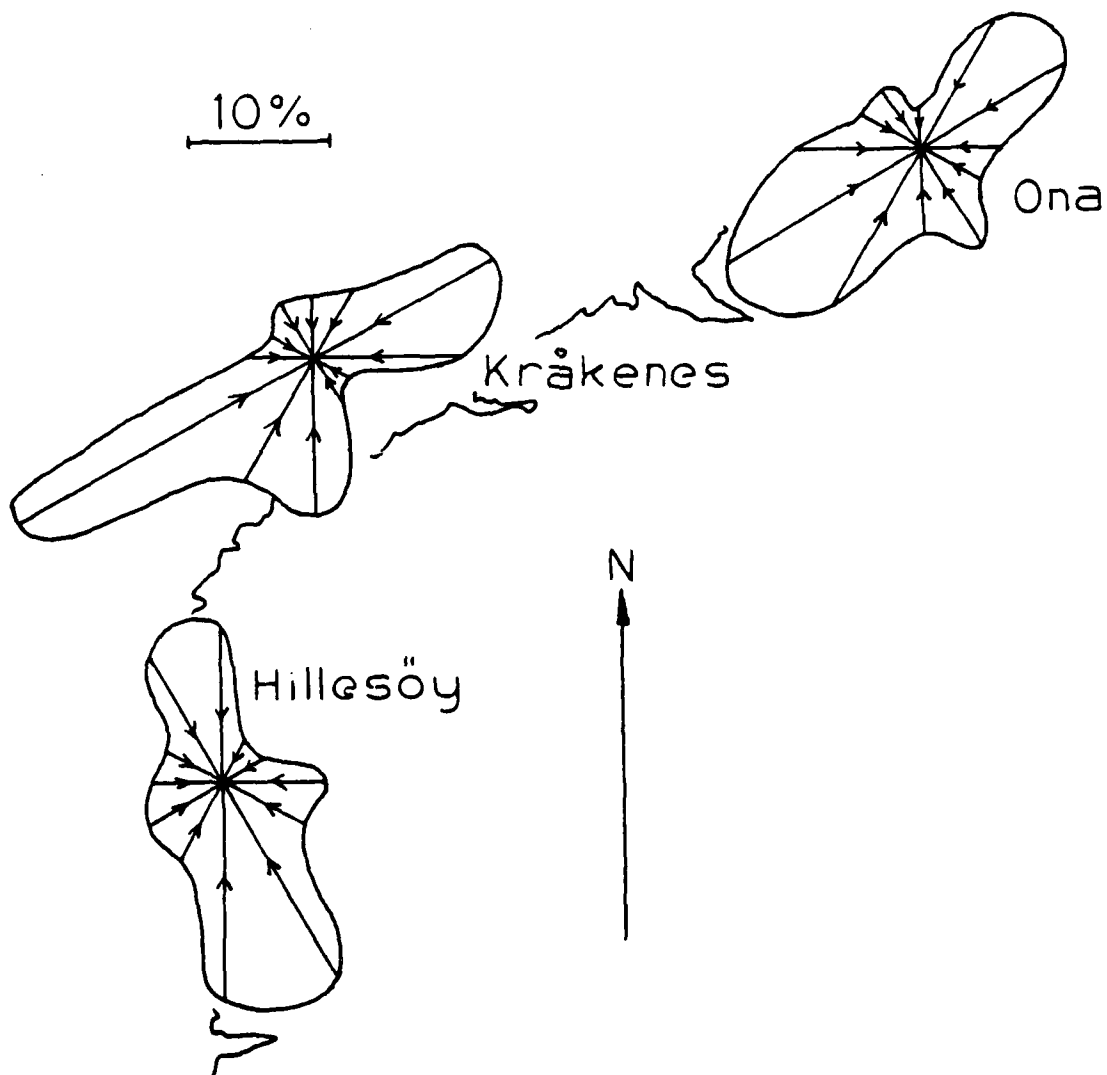


Fig. 12. Frequencies of Wind Directions in Percent for Stations Along the Coast from "Hillesøy" to "Ona."

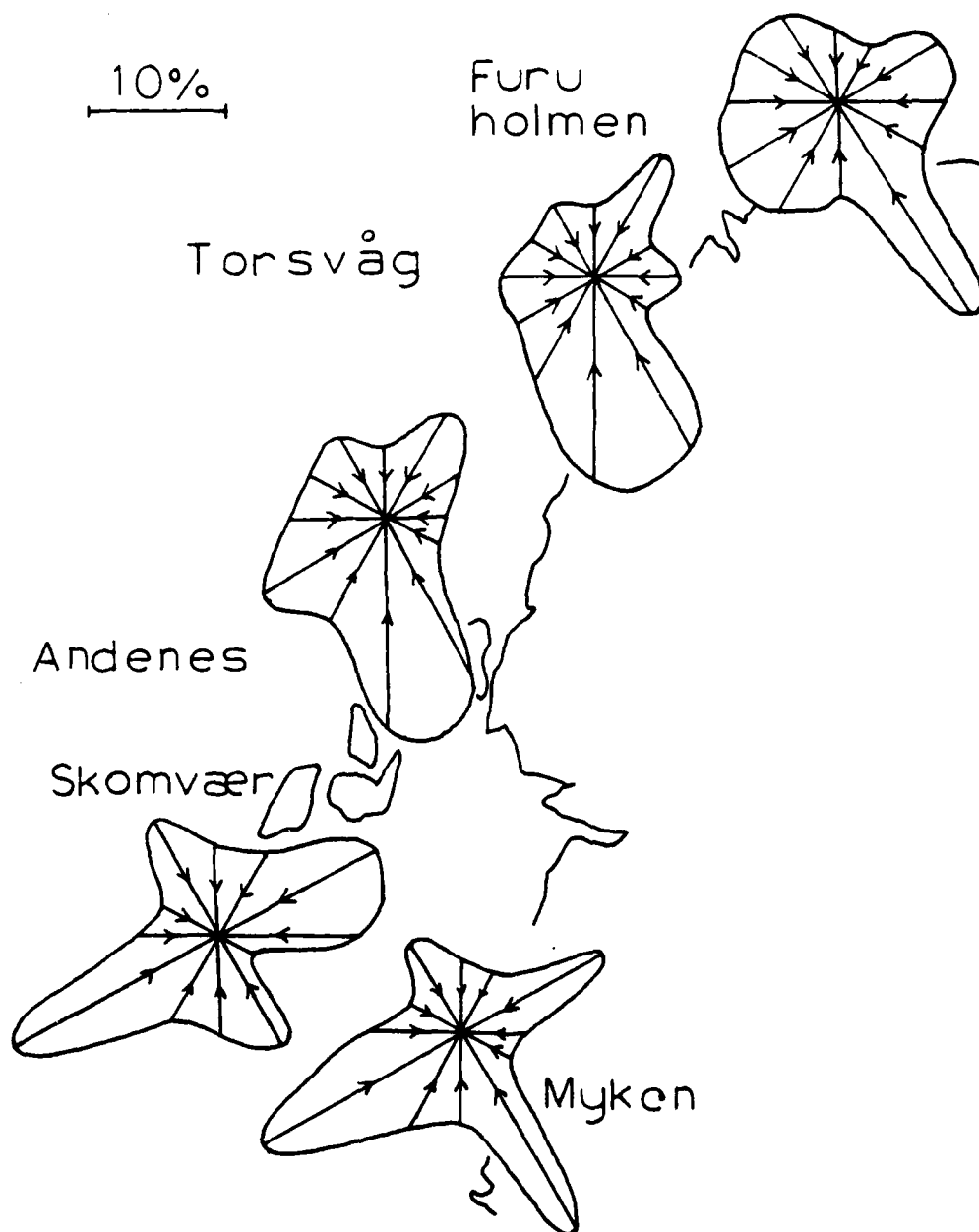


Fig. 13. Frequencies of Wind Directions in Percent for Stations Along the Coast from "Myken" to "Furuholmen."

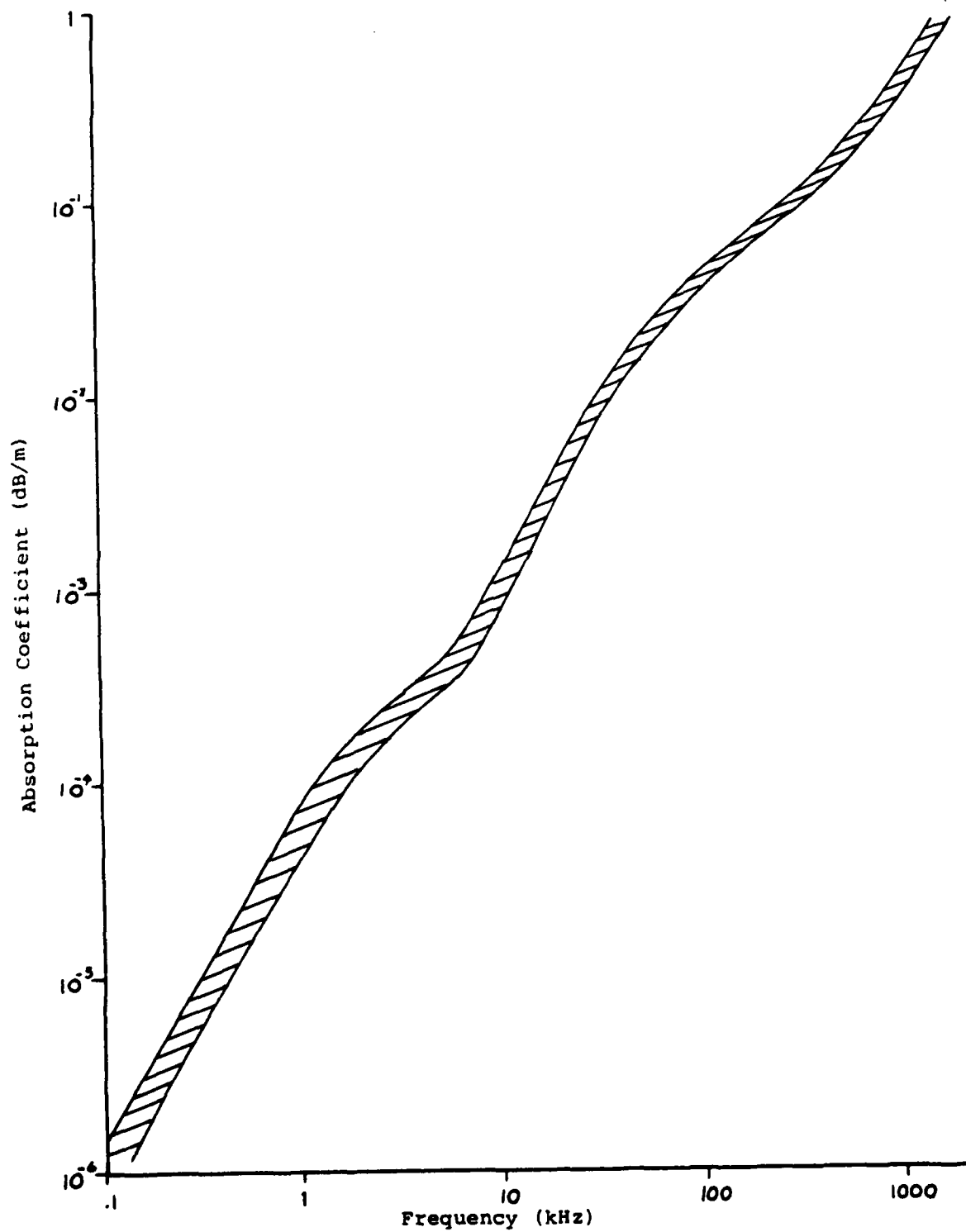


Fig. 14. Absorption Coefficient in dB/m as a Function of Frequency.

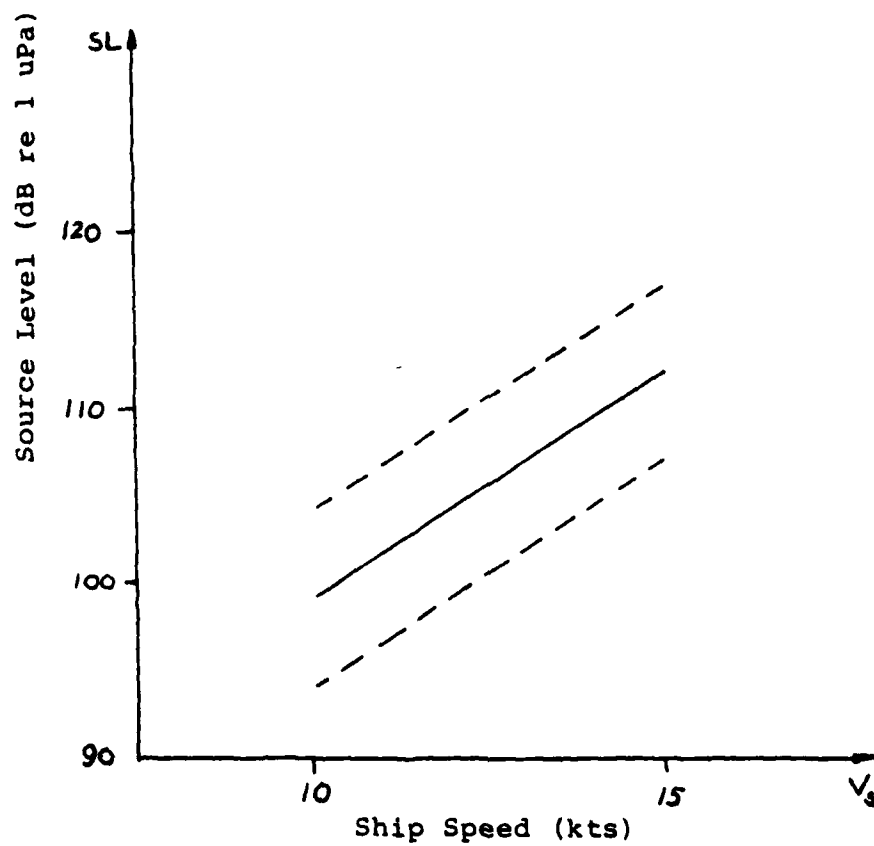


Fig. 15. Average Radiated Spectrum Level for Surface Ship as a Function of Speed in kts.

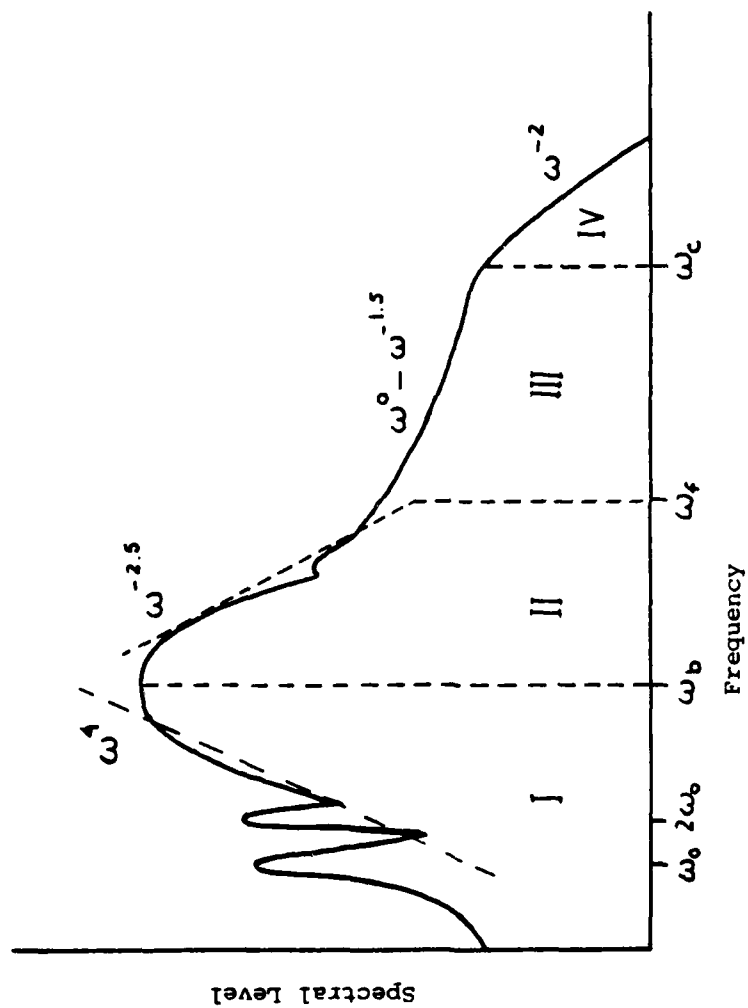


Fig. 16. General Noise Spectrum for a Cavitating Propeller.

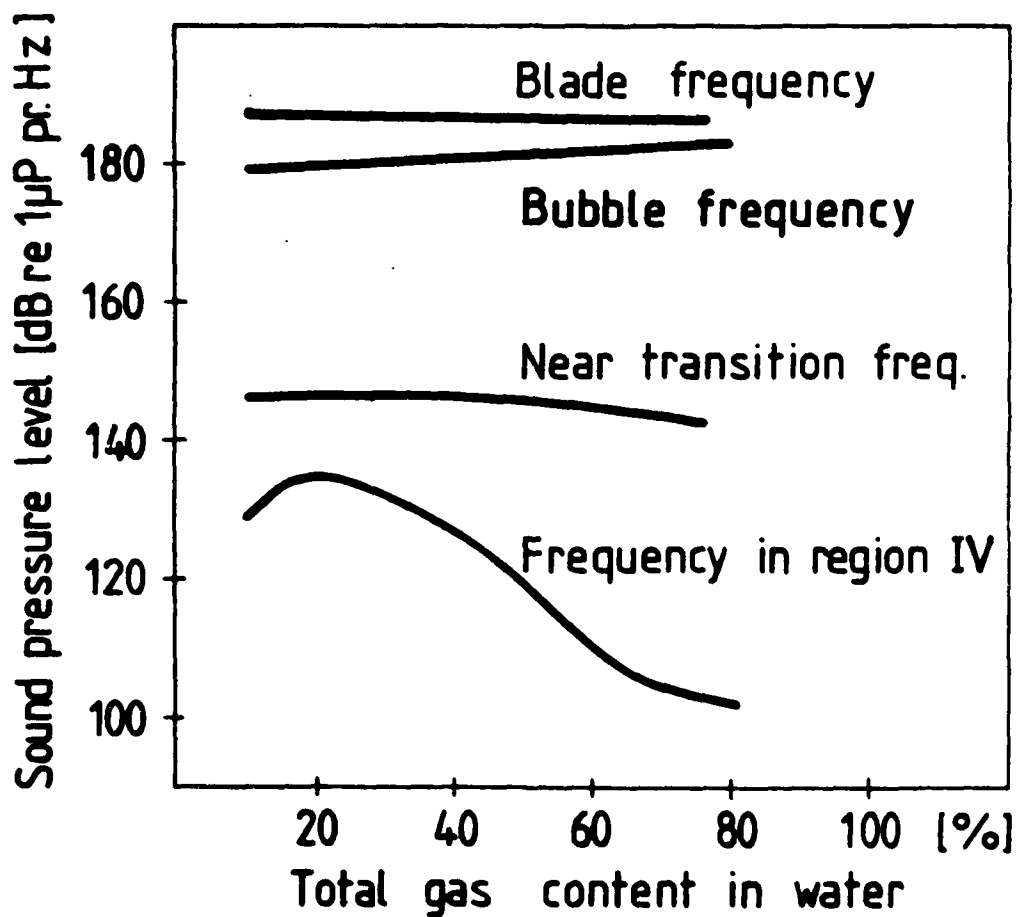


Fig. 17. Spectrum Level as a Function of Total Gas Content

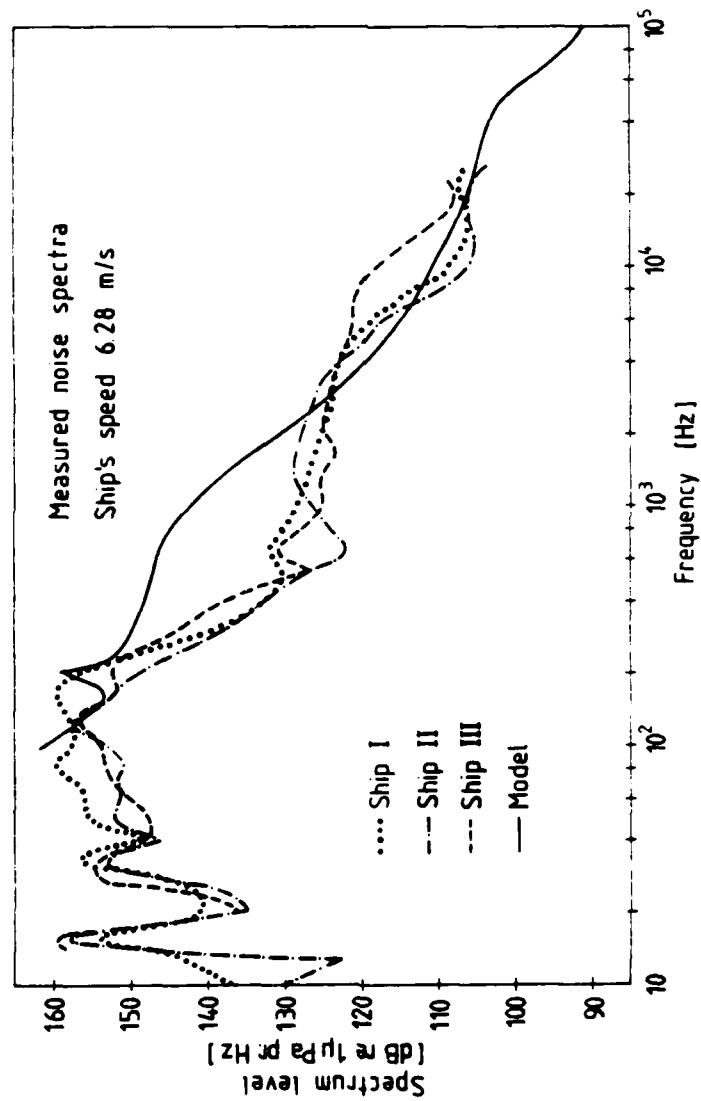


Fig. 18. Measured Model and Full Scale Noise Spectra.

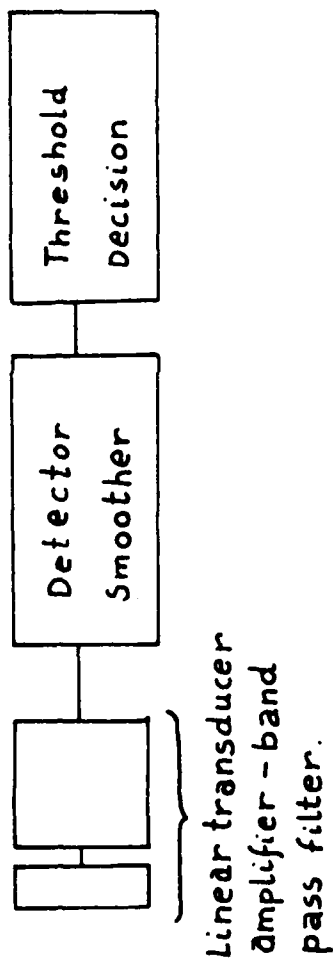


Fig. 19. Square Law Detector Scheme.

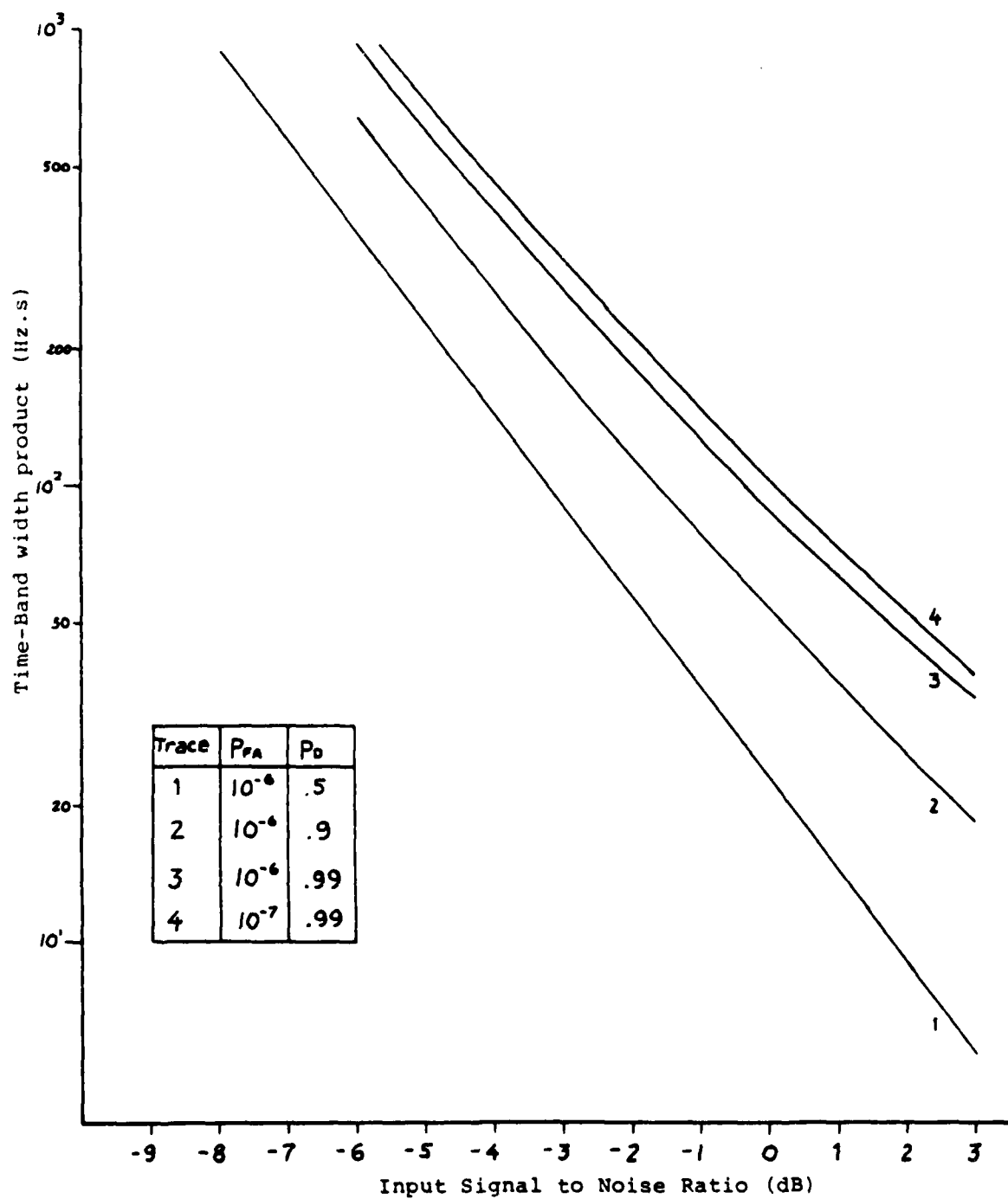


Fig. 20. Required Input S/N Ratio and BT Product for Various Operating Probabilities.

| Trace | Threshold above NL | P_{FA} |
|-------|-----------------------|---------------------|
| 1 | .88 | 10^{-6} |
| 2 | 1.0 | 2×10^{-8} |
| 3 | 1.5 | 1×10^{-10} |
| 4 | 2.0 | 1×10^{-35} |
| 5 | 2.5 | 1×10^{-24} |
| 6 | 3.0 | 1×10^{-28} |

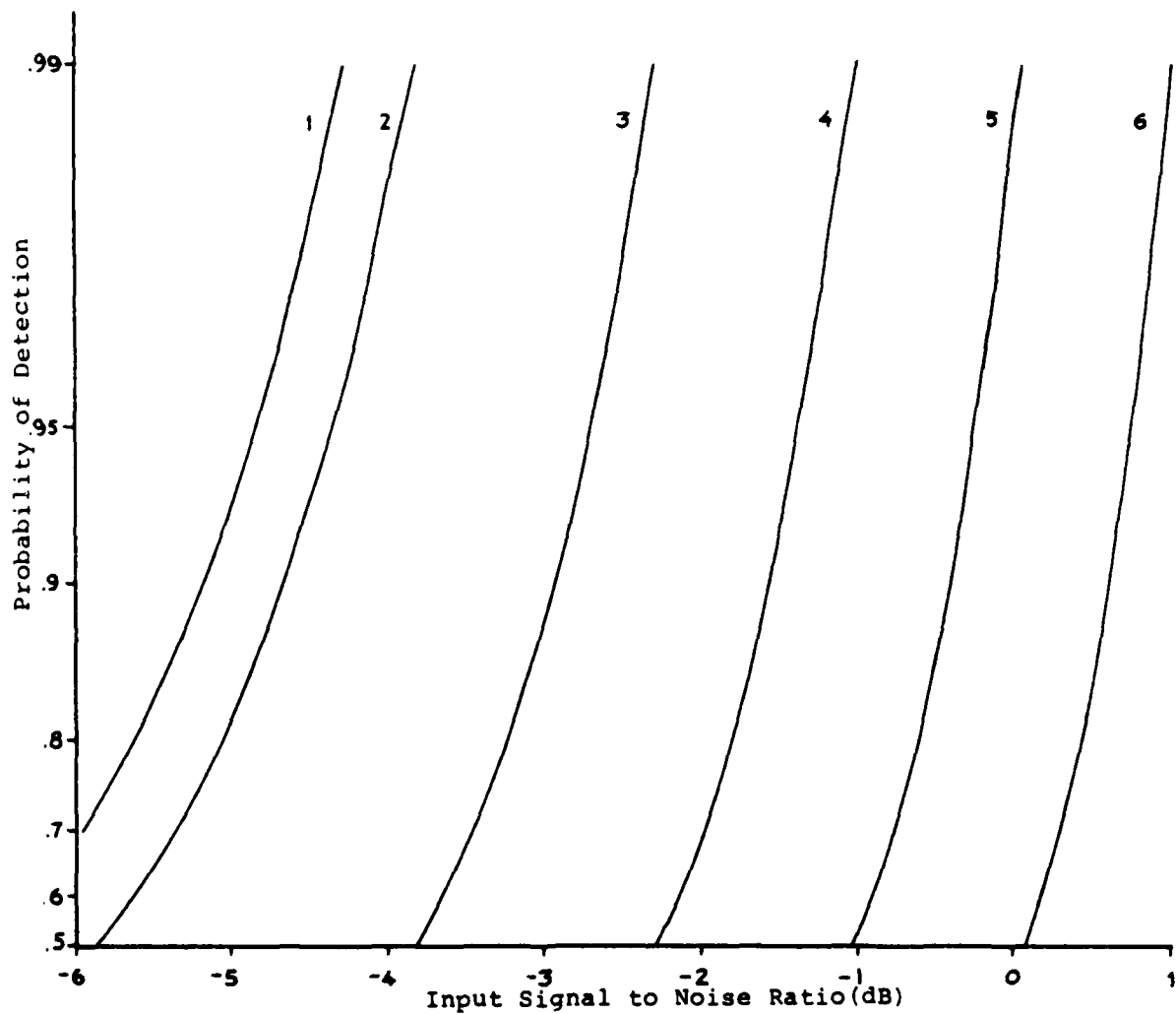


Fig. 21. Probability of Detection Versus Input S/N Ratio for Various Thresholds.

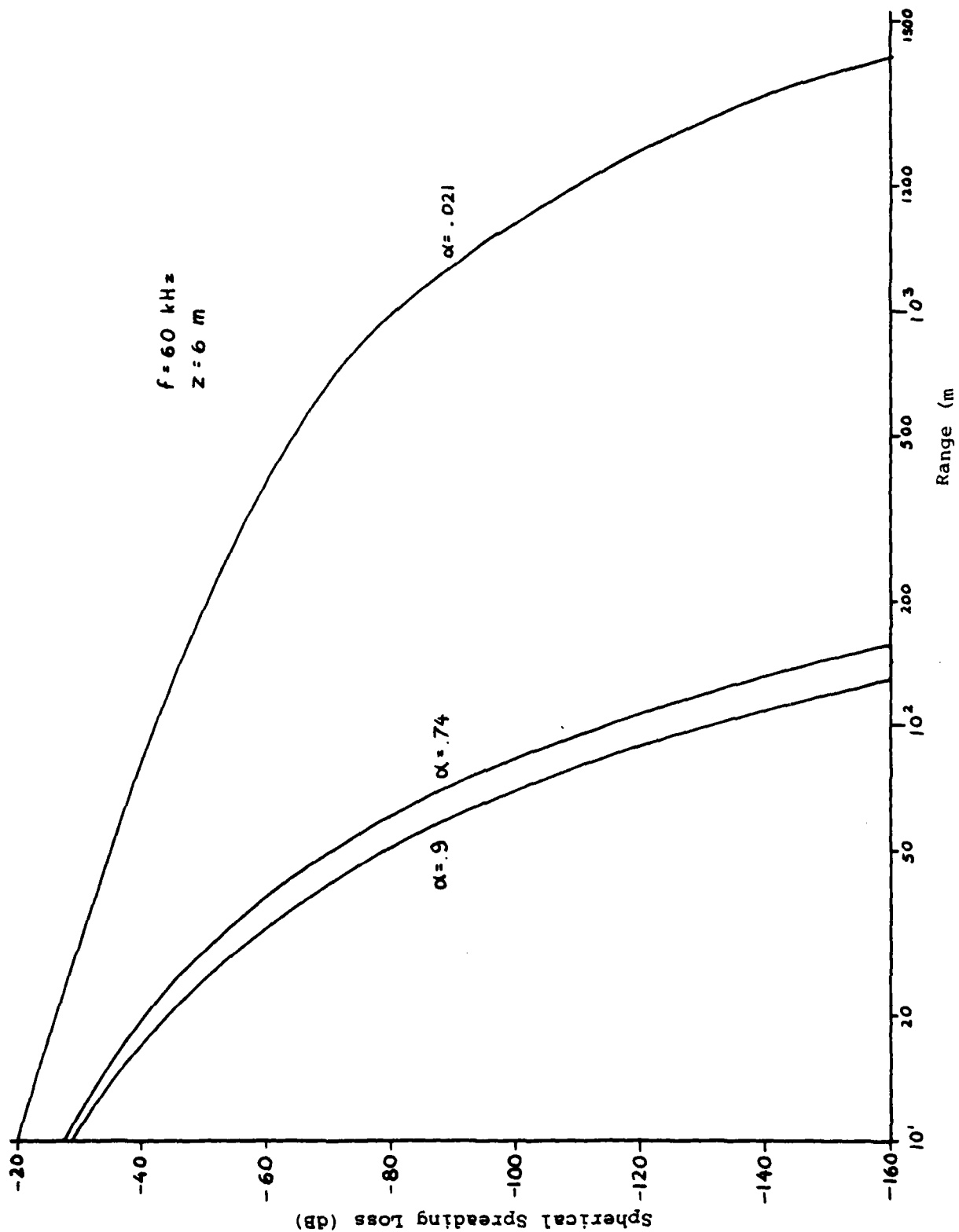


Fig. 22. $-20\log R - \alpha R$ Versus R for Frequency of 60 kHz.

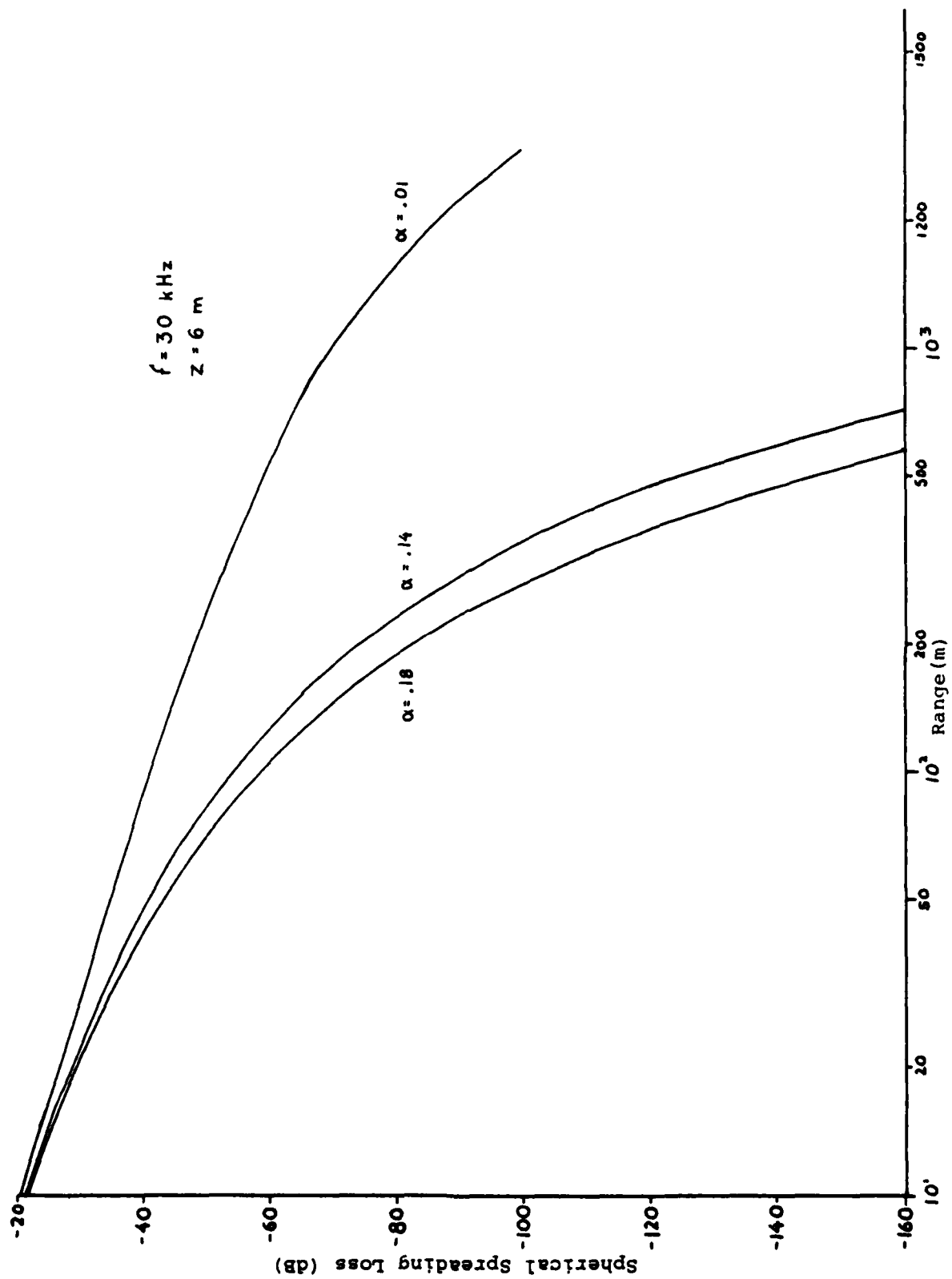


Fig. 23. $-20\log R - \alpha R$ Versus R for a Frequency of 30 kHz.

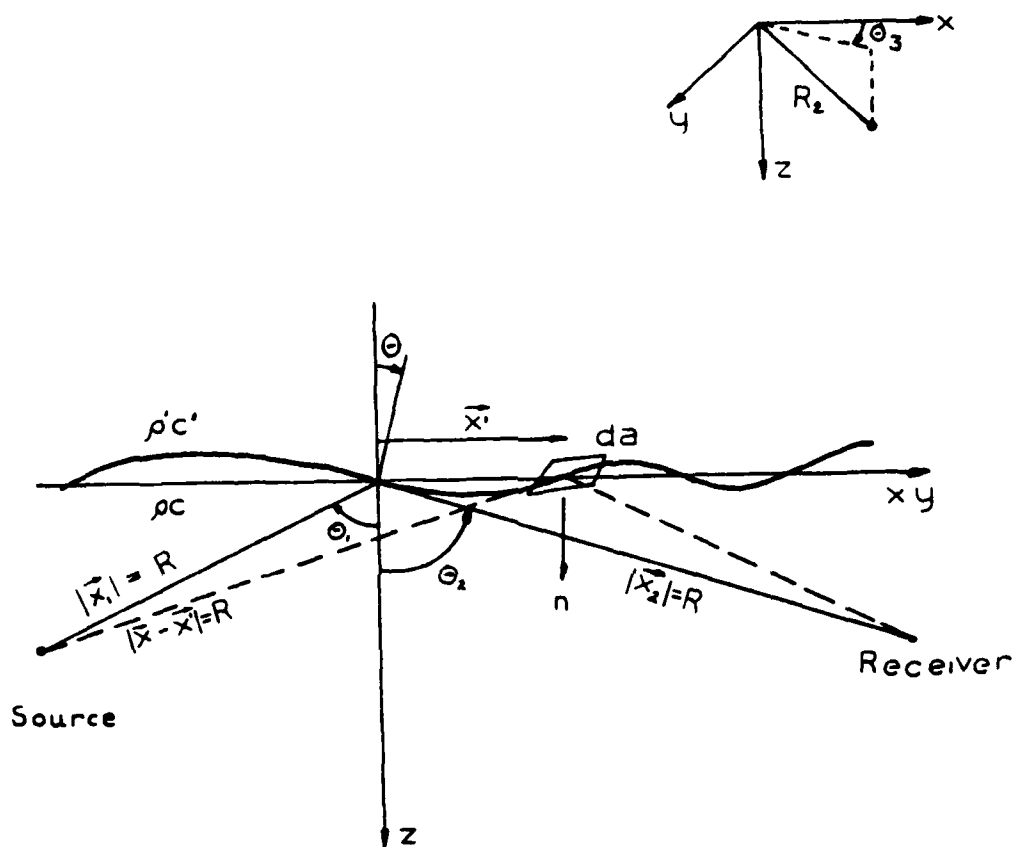


Fig. 24a. Geometry at the Sea Surface Scattering.

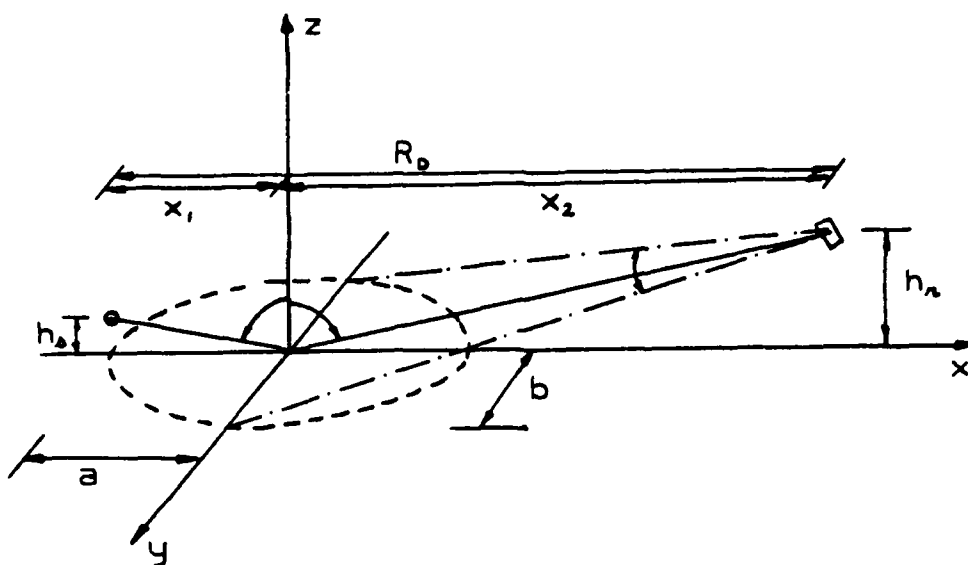


Fig. 24b. Specular Scattering Geometry.

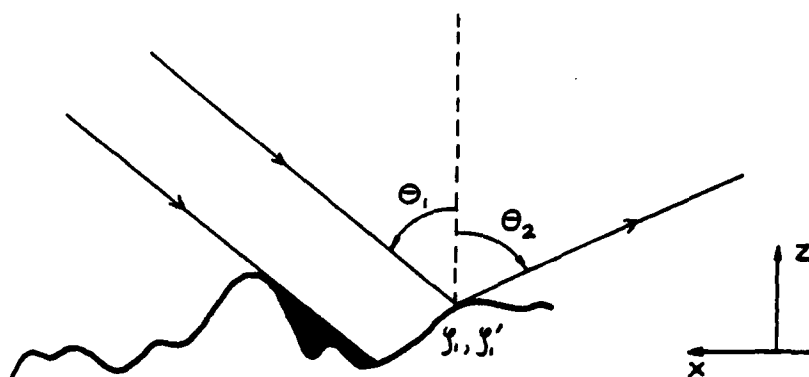


Fig. 25. Rough Surface Shadowing Geometry.

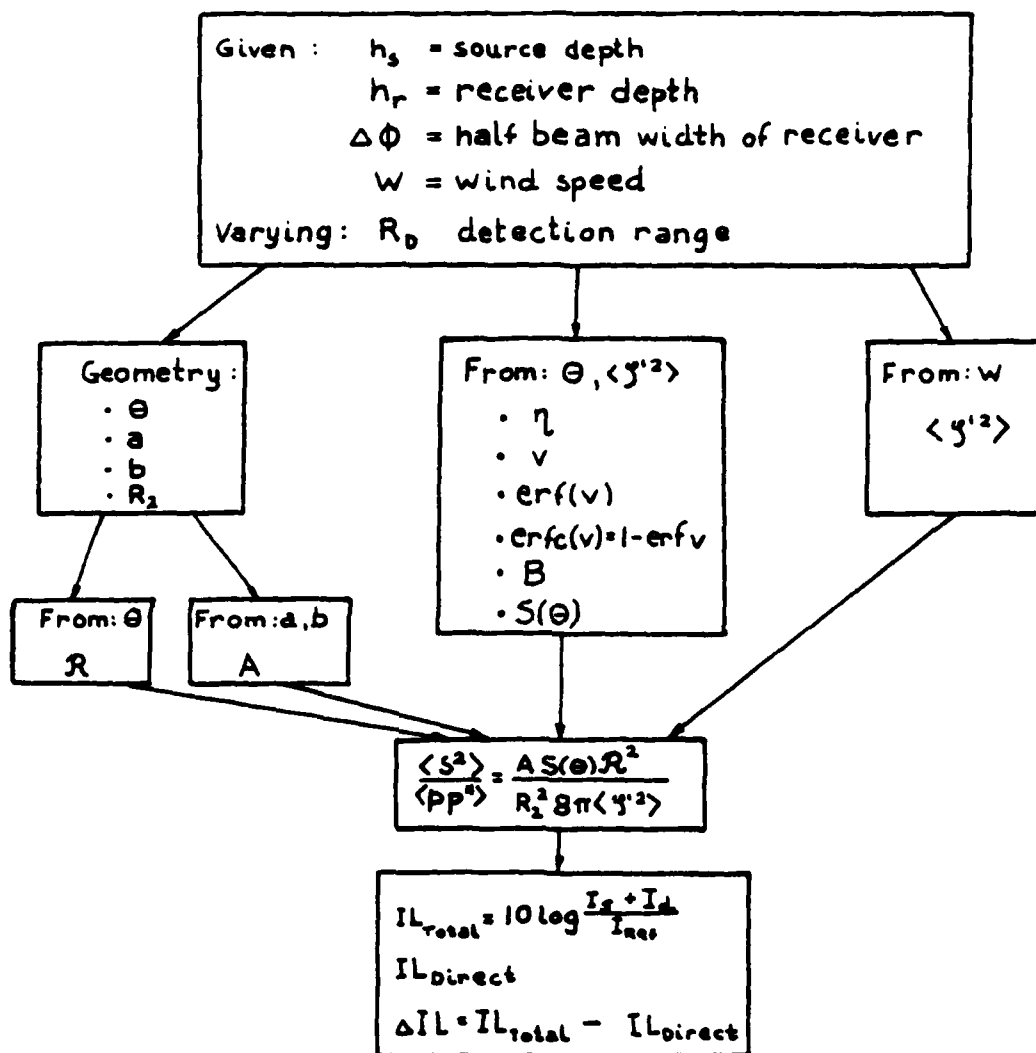


Fig. 26. Calculation Scheme of the Surface Scattering Effect.

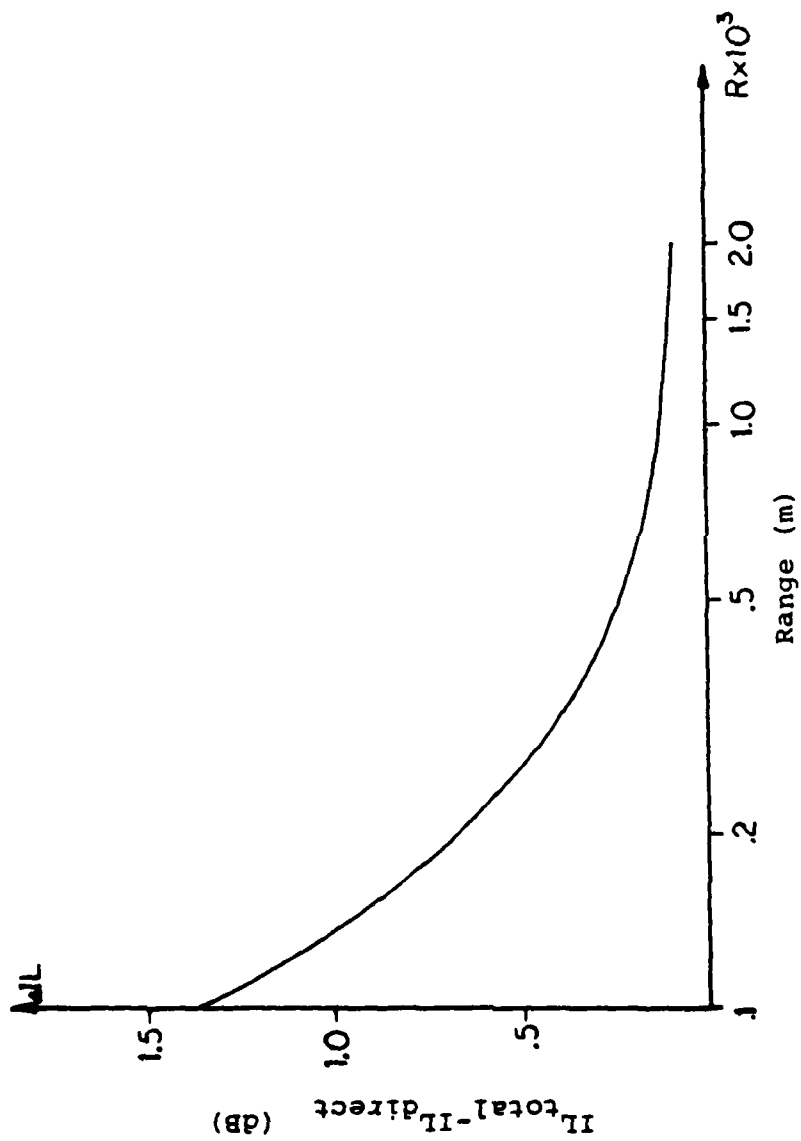


Fig. 27. AIL Versus R.

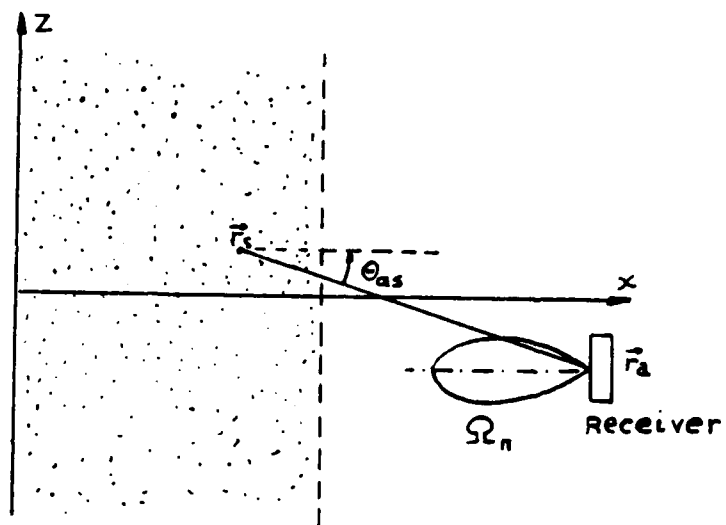


Fig. 28. Geometry of the Subsurface Propagation Model.

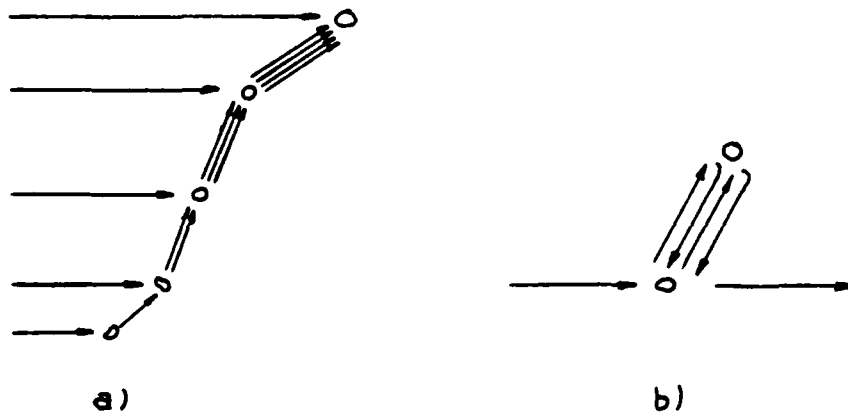


Fig. 29. a) Chains of Successive Scattering.
 b) Scattering Pattern Going Through the Same Scatterer More than Once.

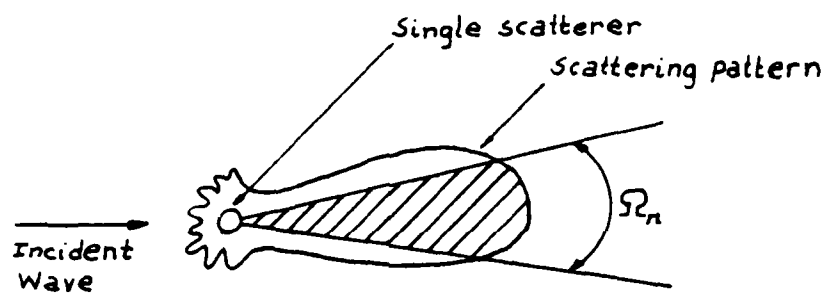


Fig. 30. Scattering Pattern.

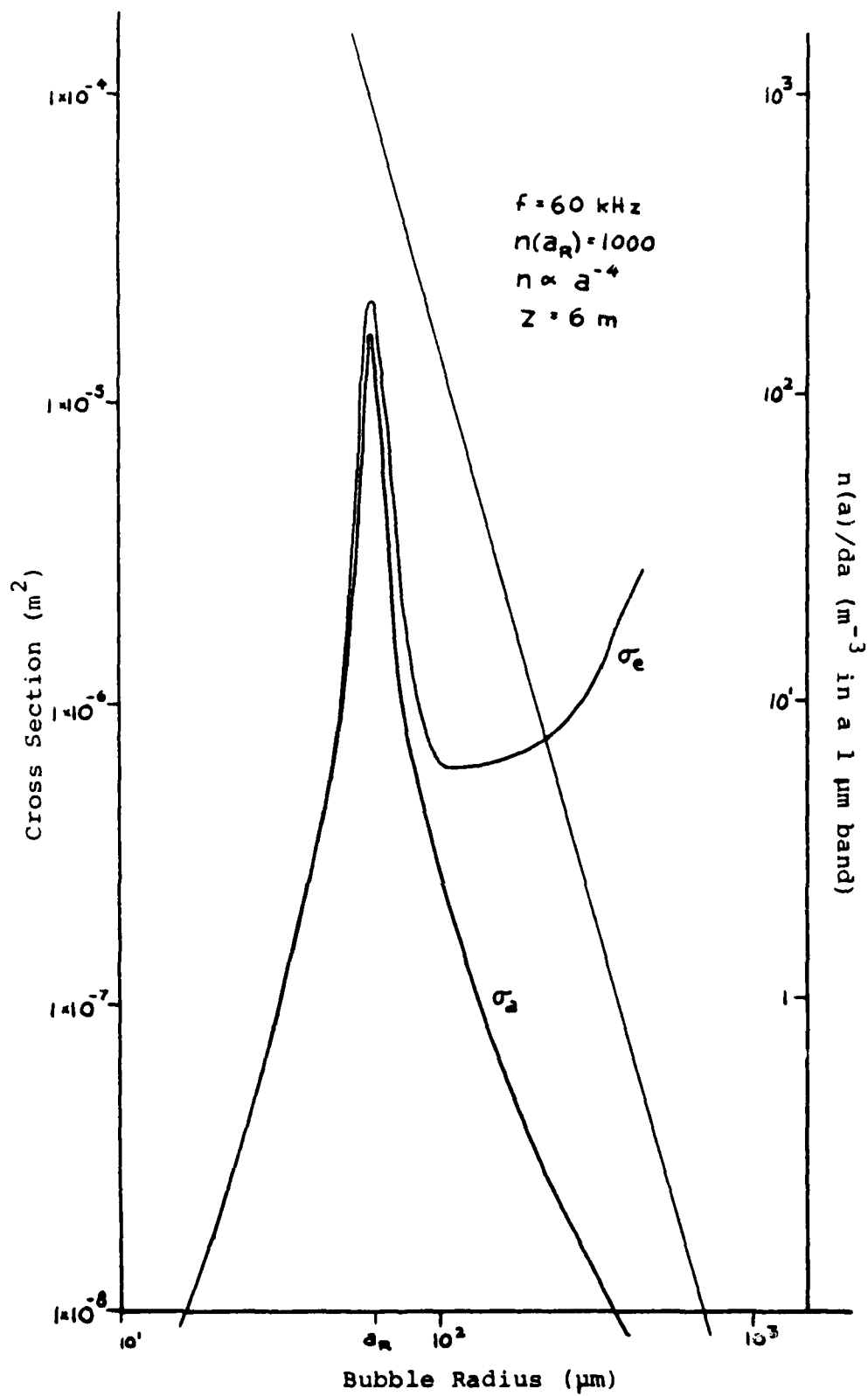


Fig. 31. σ_e and σ_a for 60 kHz.

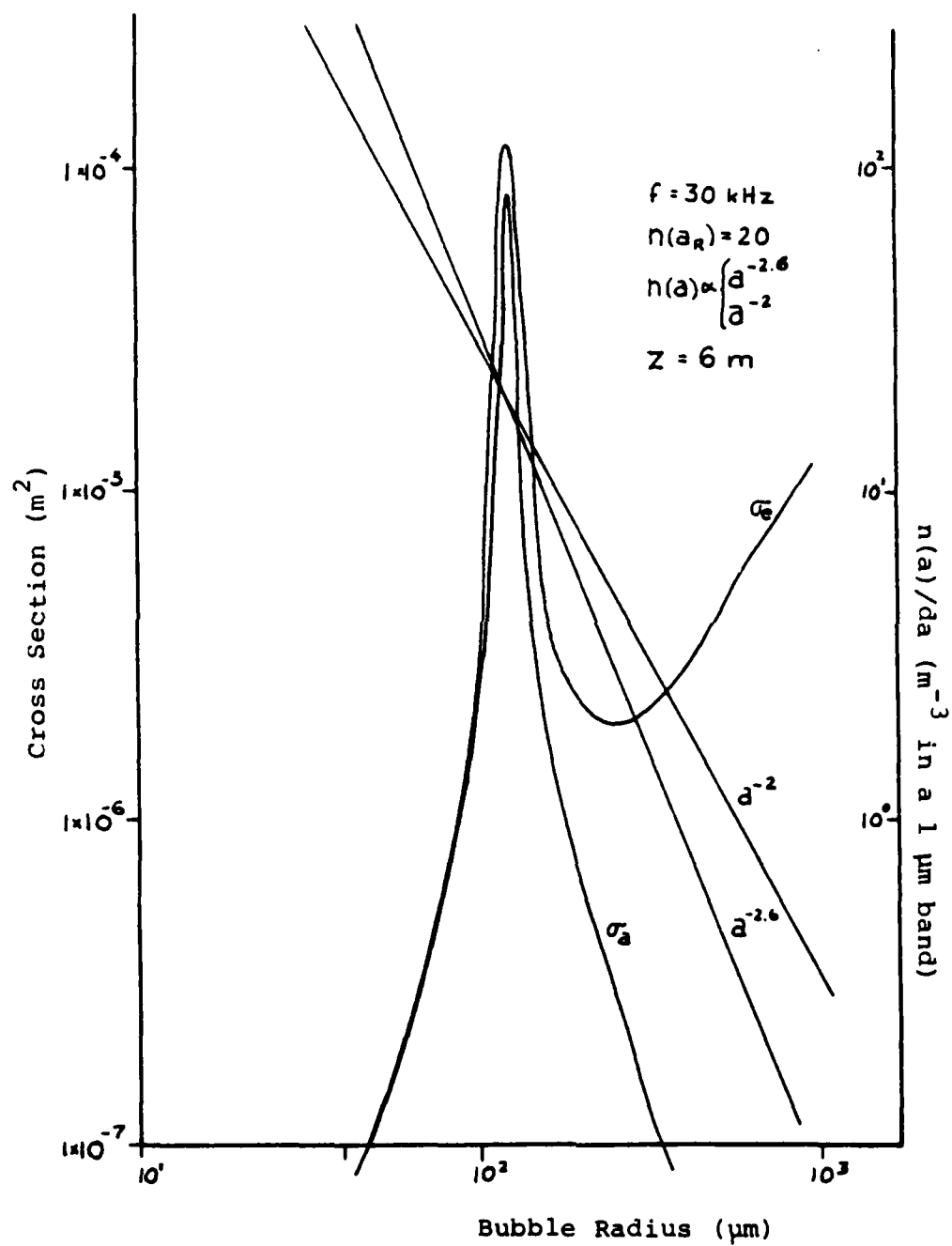


Fig. 32. σ_e and σ_a for 30 kHz.

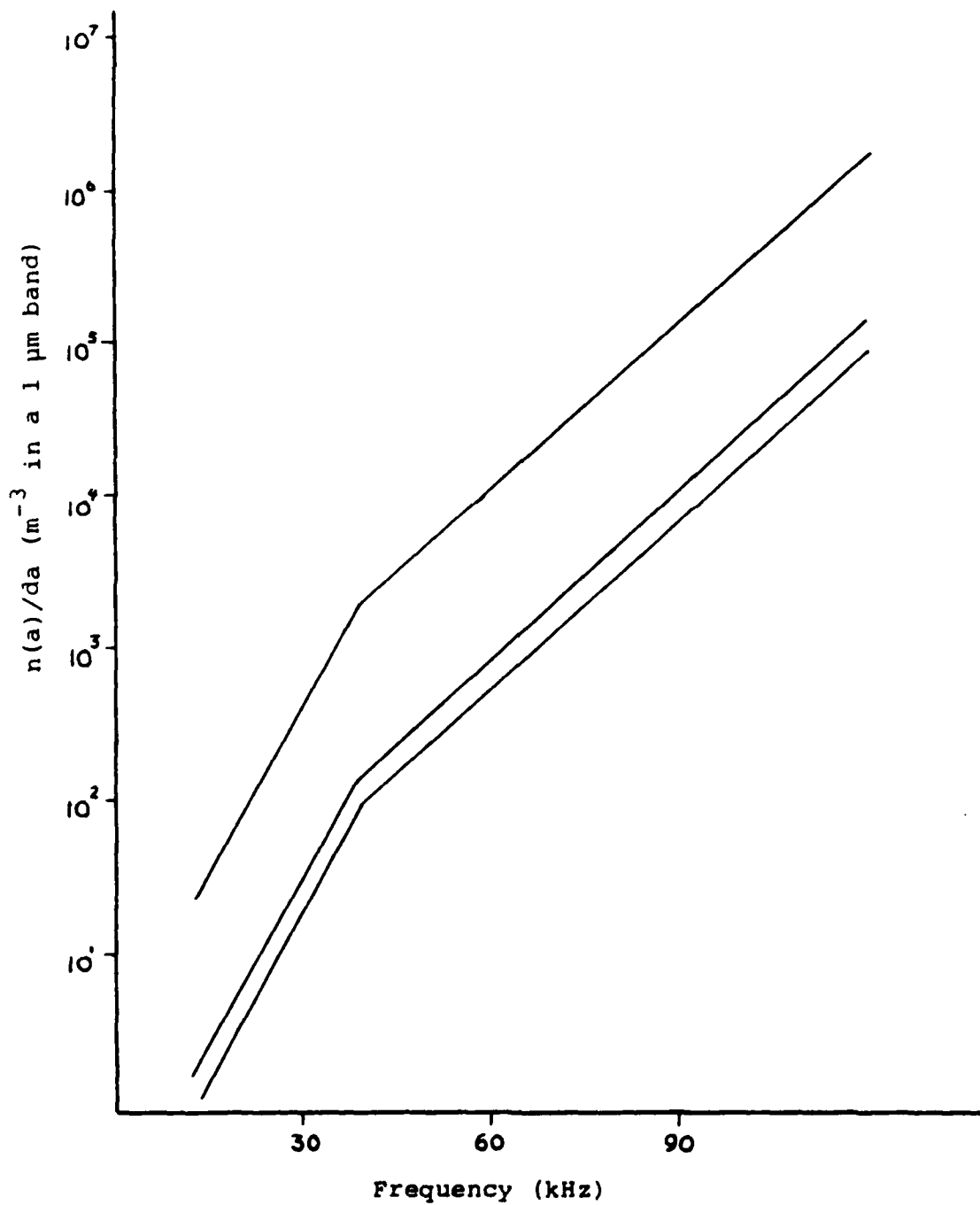


Fig. 33. Interpolated Bubble Data.

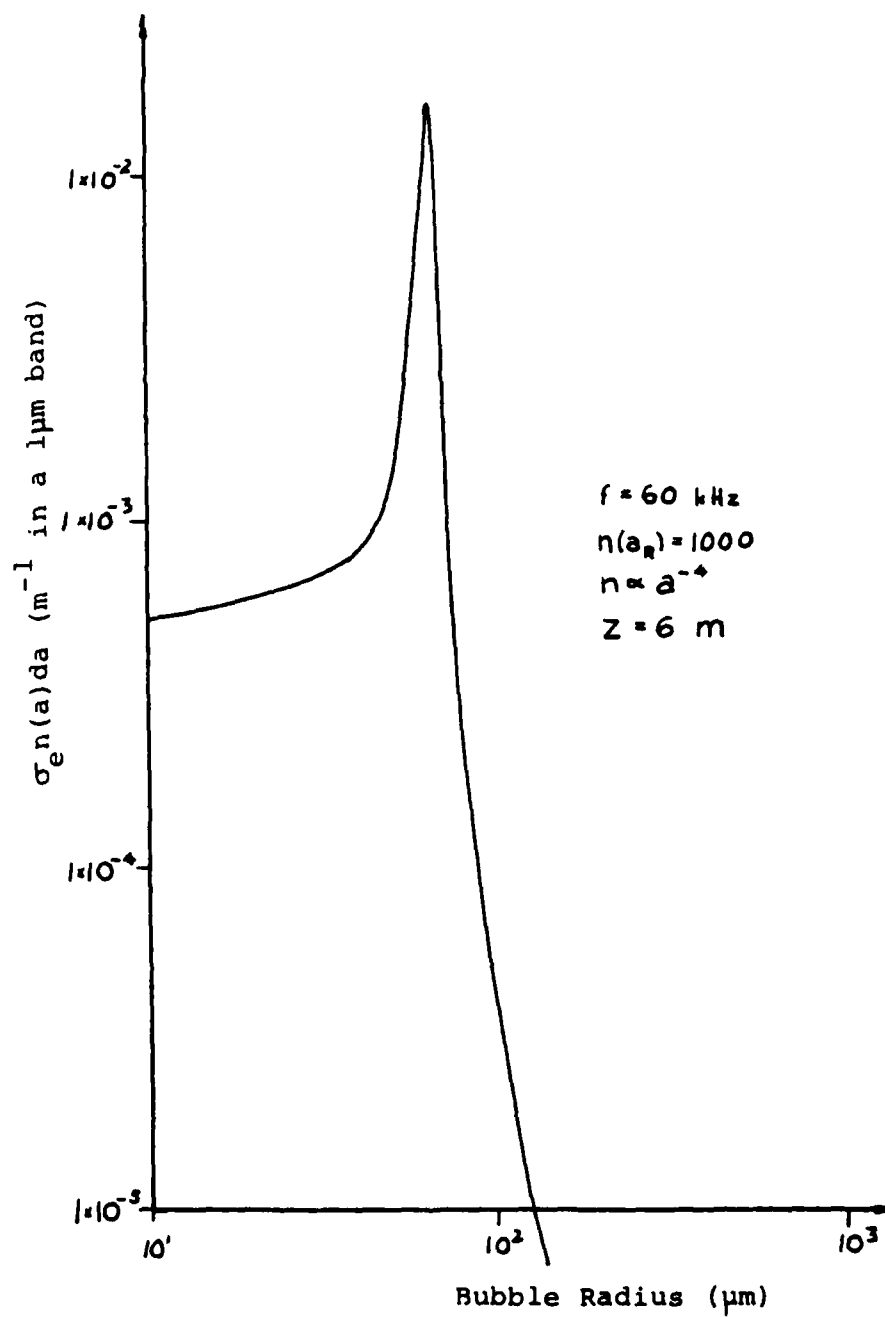


Fig. 34. $\sigma_e(a)n(a)da$ for 60 kHz.

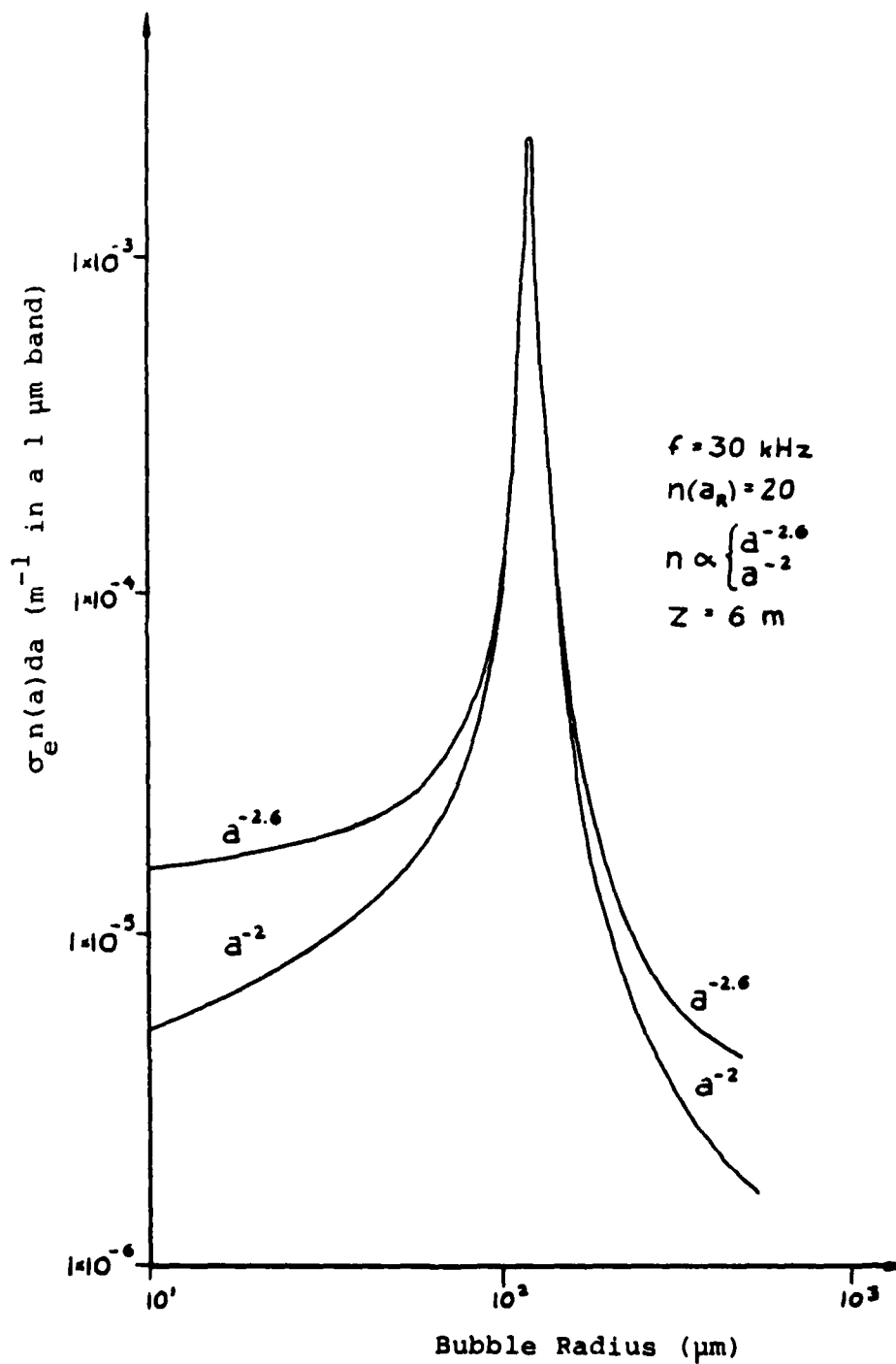


Fig. 35. $\sigma_e(a)n(a)da$ for 30 kHz.

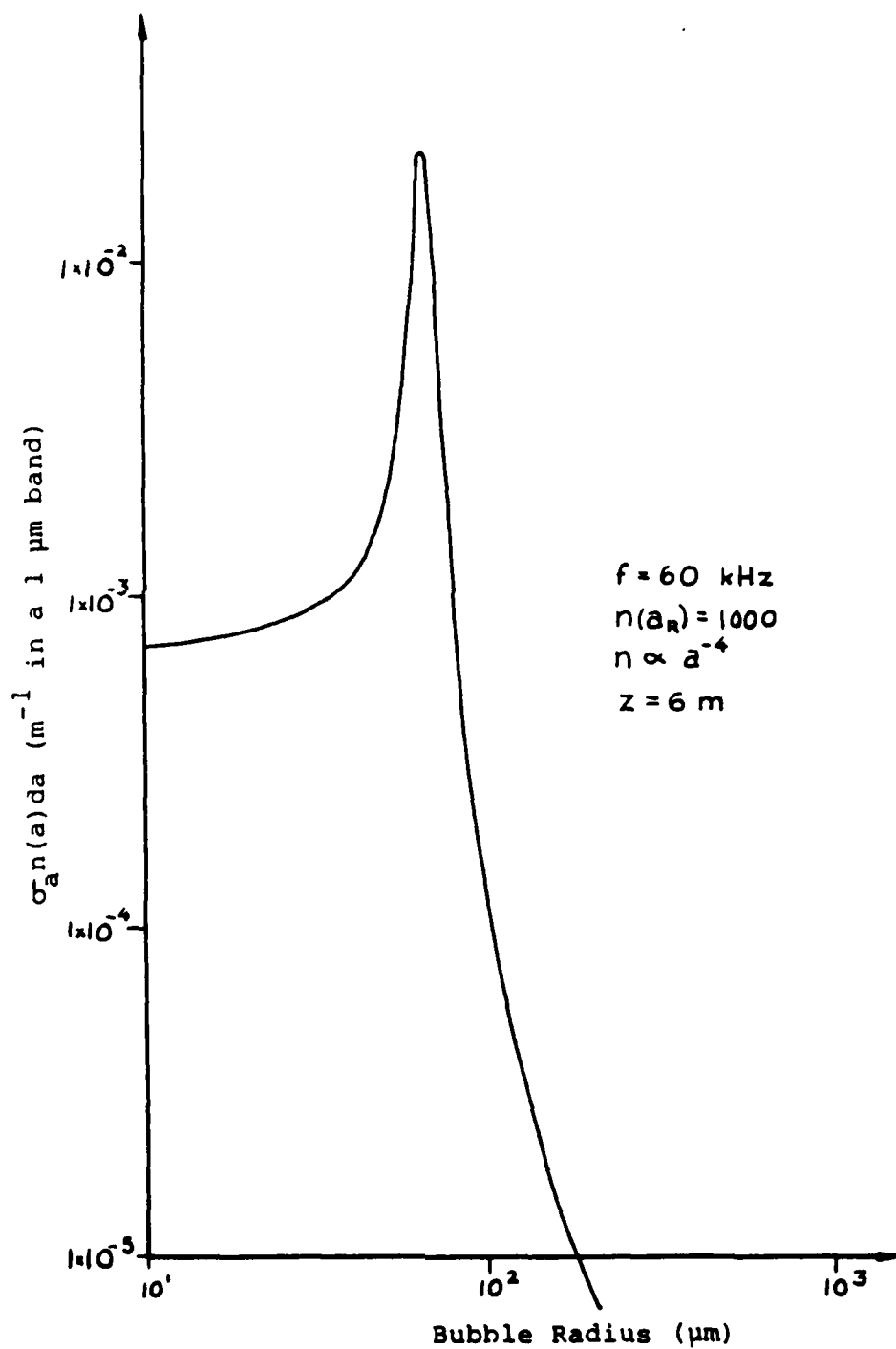


Fig. 36. $\sigma_a(a)n(a)da$ for 60 kHz.

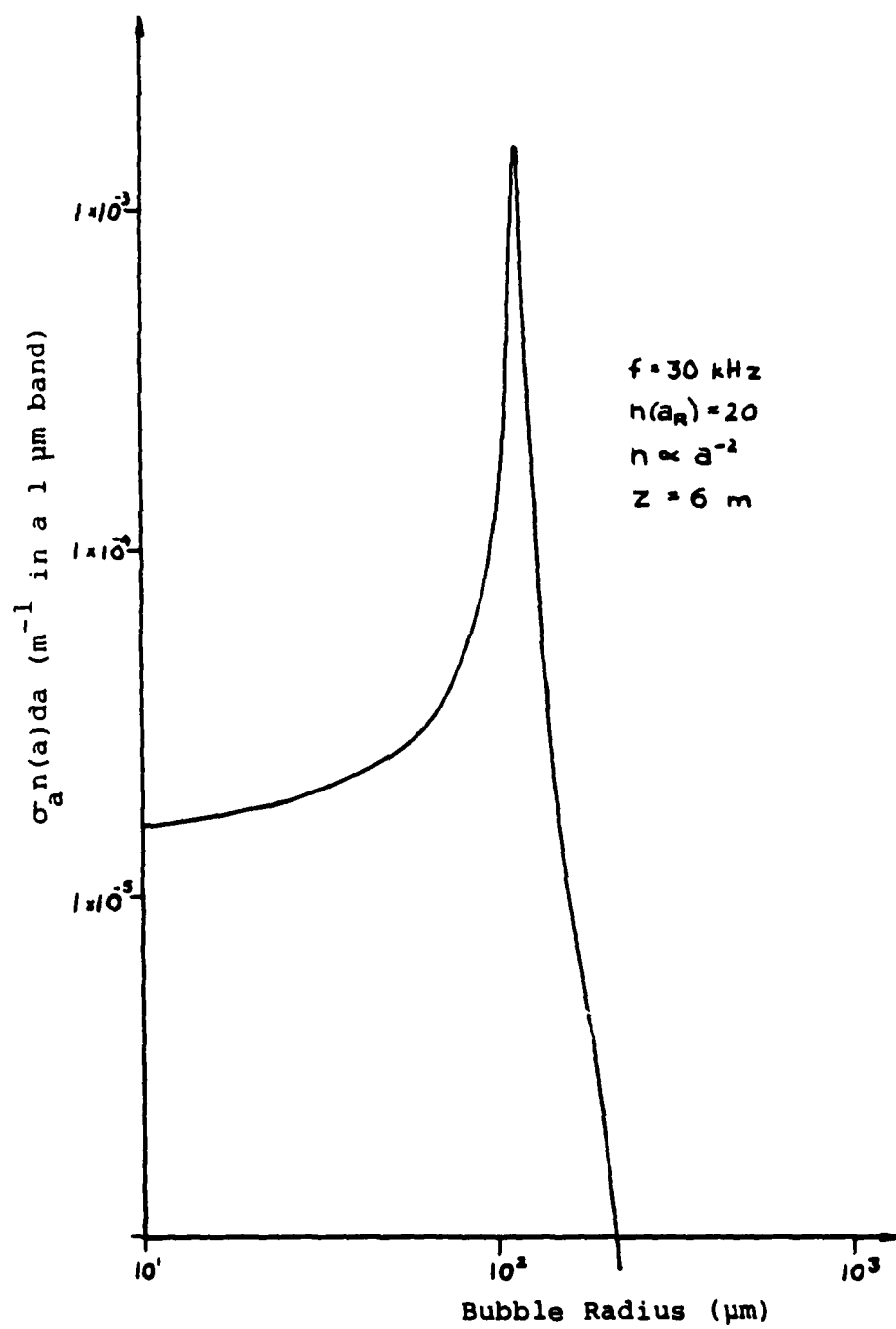


Fig. 37. $\sigma_a n(a) da$ for 30 kHz.

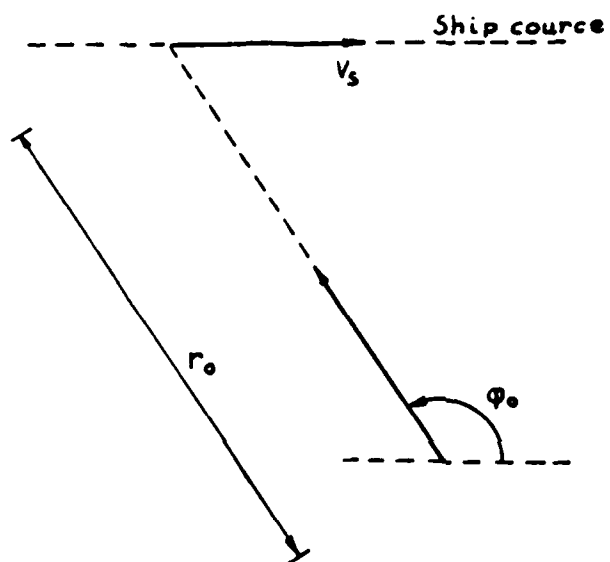


Fig. 38. Pursuit Homing Geometry.

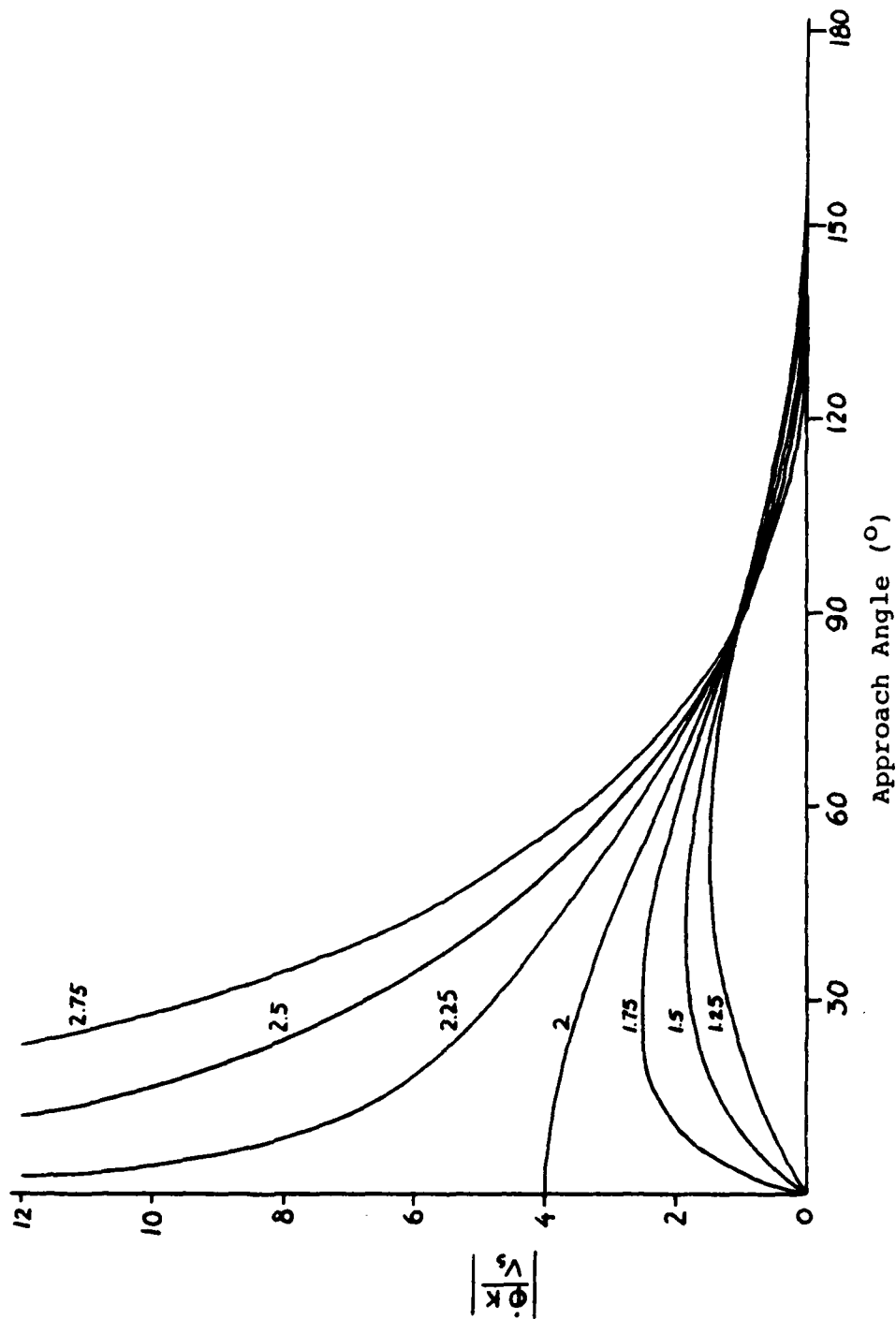


Fig. 39. $\left| \frac{\dot{\phi} K}{V_s} \right|$ as a Function of ϕ With Parameter p .

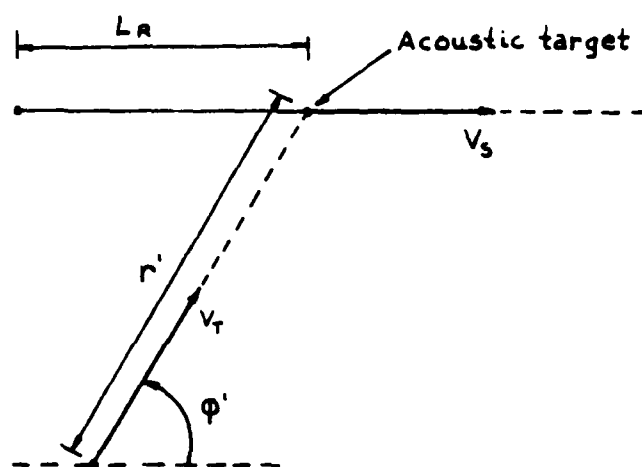


Fig. 40. Hit Criterion Geometry.

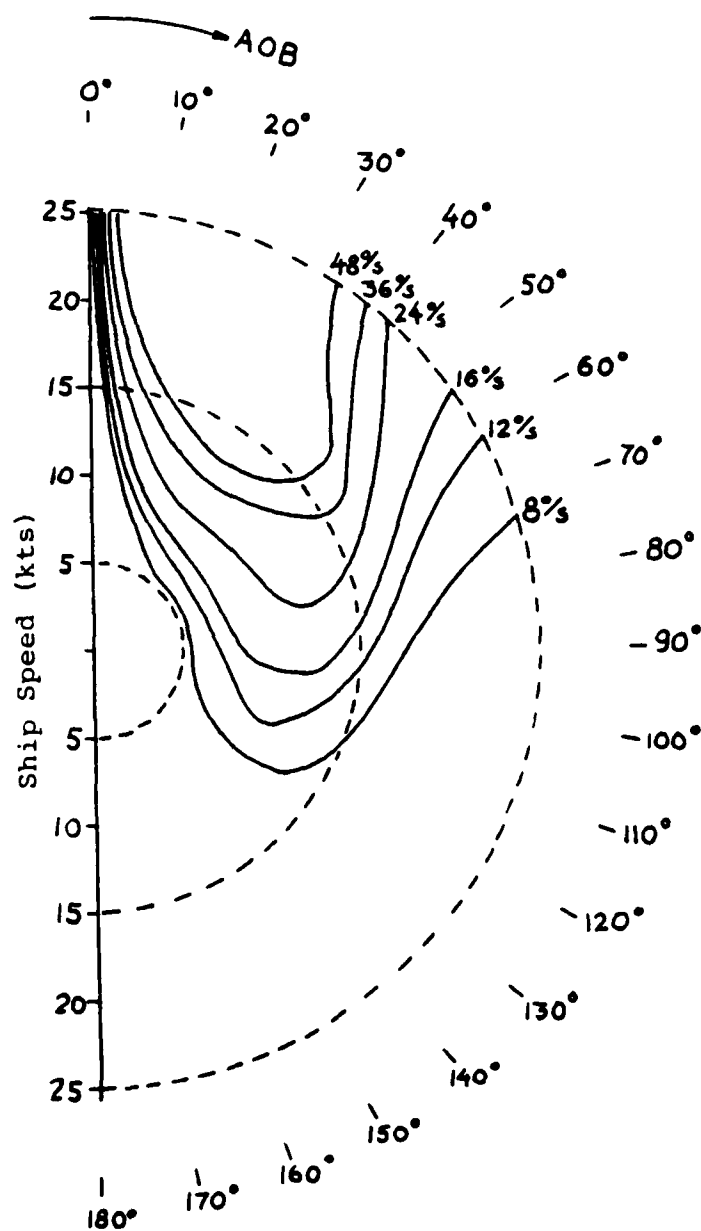


Fig. 41. AOB-limitation Versus Ship Speed with Parameter Maximum Turn Rate.

LIST OF REFERENCES

1. IKU (Continental Shelf Institute, Norway), Bølgedata fra Kontinentalsokkelen (translated, Wave Data from the Continental Shelf), IK U B 772/77/TA/mg, October 1977.
2. Lövik, A., Akustisk Måling av Vind og Bølgeinduserte Gassbobler i Havet (translated, Acoustic Measurements of Wind and Wave Induced Air Bubbles in the Ocean), NTH ELAB Report STF 44A7914, pp. 15-16, May 1979.
3. Medwin, H., In Situ Acoustic Measurements of Bubble Populations in Coastal Waters, J. Geoph. Res., V. 75, pp. 599-611, 1971.
4. Wenz, G. M., Acoustic Ambient Noise in the Ocean Spectra and Sources, J.A.S.A., V. 34, pp. 1936-1956, 1962.
5. Norwegian Defence Research Establishment, Division for Underwater Warfare, Typical Sound Velocity Curves in Norwegian Coastal Waters.
6. U.S. Navy, N.O. Publication 700, 1969.
7. Urick, R. J., Principles of Underwater Sound, McGraw-Hill, 1975.
8. Thorp, W. H., Deep Ocean Sound Attenuation in the Sub- and Low-Kilocycle-per-Second Region, J.A.S.A., V. 38, pp. 648-654, 1965.
9. Ross, D., Mechanics of Underwater Sound, Pergamon Press, 1976.
10. Morse, P.M. and Ingard, K. V., Theoretical Acoustics, McGraw-Hill, 1968.
11. Lövik, A., A Theoretical and Experimental Investigation on Propeller Cavitation Noise, NTH ELAB Report STF 44A80121, February 1980.
12. Lövik, A., Acoustic Detection of Gas Bubbles in Water, NTH ELAB Report STF 44A80122, pp. 25-38, February 1980.
13. Cox, C. S., and Munk, W. H., Measurements of the Roughness of the Sea Surface from Photographs of the Sun's Glitter, J. Optic, Soc. Am., V. 44, pp. 838-850, 1954.
Cox, C. S., and Munk, W. H., Statistics of the Sea Surface Derived from the Sun Glitter, J. Marine Res., V. 13, pp. 198-227, 1954.

14. Pierson, W. M., and Moskowitz, L., A Proposed Spectral Form for Fully Developed Wind Seas Based on Similarity Theory of S. A. Kitaigorodskic, J. Geoph. Res., V. 69, pp. 518.-5190, 1964.
15. Tolstoy, I. and Clay, C., Ocean Acoustics, McGraw-Hill, 1966.
16. Fortuin, L., The Wave Equation in a Medium with a Time-dependent Boundary, J.A.S.A., V. 53, pp. 302-305, 1972.
17. Beckmann, P., Shadowing of Randomly Rough Surfaces, Trans IEEE, Antenna Propagation, V. 13, pp. 384-388, 1965.
18. Wagner, R., Shadowing of Randomly Rough Surfaces, J.A.S.A., V. 41, pp. 138-147, 1967.
19. Kinsler, L. E. and Frey, A. R., Fundamental of Acoustics, Second Edition, Wiley, 1962.
20. Ishimaru, A., Wave Propagation and Scattering in Random Media, V. 2, Academic Press, 1978.
21. Clay, C. and Medwin, H., Acoustical Oceanography, Wiley, 1977.
22. Medwin, H., The Rough Surface and Bubbles Effect on the Sound Propagation in a Surface Duct, NPS-61Md71101A, October 1971.
23. Van Nostrand, D., Principles of Guided Missile Design, McGraw-Hill, 1955.
24. Texas Instruments Inc., TI Programmable 58/59 Math/Utilities, 1978.
25. Texas Instruments Inc., TI Programmable 58/59 Master Library, 1977.

INITIAL DISTRIBUTION LIST

| | No. Copies |
|---|------------|
| 1. Defense Technical Information Center Cameron Station Alexandria, Virginia 22314 | 2 |
| 2. Library, Code 0142 Naval Postgraduate School Monterey, California 93940 | 2 |
| 3. Department Chairman, Code 61 Department of Physics and Chemistry Naval Postgraduate School Monterey, California 93940 | 1 |
| 4. NAVMATCOM NOR, Bureau of Weapons N-5078 Haakonsvern Norway | 3 |
| 5. KNM "TORDENSKJOLD," Torpedo-/mine-skolen N-5078 Haakonsver Norway | 2 |
| 6. Norwegian Defense Research Establishment Devison for Electronic P.O. Box 25, 2007 Kjeller Norway | 1 |
| 7. Norwegian Defense Establishment Devison for Underwater Warfare P.O. Box 115, N-3191 Horten Norway | 1 |
| 8. Professor K. E. Woehler, Code 61Wh Department of Physics and Chemistry Naval Postgraduate School Monterey, California 93940 | 1 |
| 9. Professor H. Medwin, Code 61Md Department of Physics and Chemistry Naval Postgraduate School Monterey, California 93940 | 1 |
| 10. CDR Y. D. Tronstad, RNoN Naustvg. 23, N-5088 Mjølkeråen Norway | 3 |

DATE
FILME